

**3D PRINTED FLEXIBLE MATERIALS FOR ELECTROACTIVE  
POLYMER STRUCTURES, SOFT ACTUATORS, AND FLEXIBLE  
SENSORS**

by

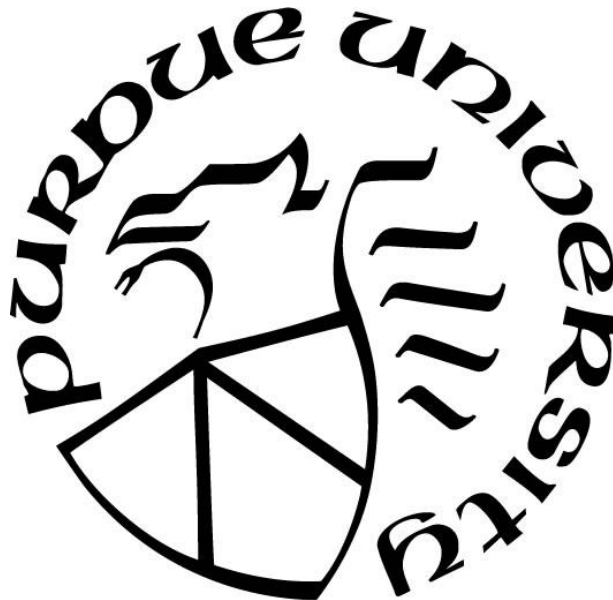
**David Felipe González Rodríguez**

**A Thesis**

*Submitted to the Faculty of Purdue University*

*In Partial Fulfillment of the Requirements for the degree of*

**Doctor of Philosophy**



Purdue Polytechnic Institute

West Lafayette, Indiana

August 2020

**THE PURDUE UNIVERSITY GRADUATE SCHOOL  
STATEMENT OF COMMITTEE APPROVAL**

**Dr. Brittany Newell, Co-Chair**

School of Engineering Technology

**Dr. Jose Garcia, Co-Chair**

School of Engineering Technology

**Dr. Robert Nawrocki, Committee Member**

School of Engineering Technology

**Dr. Benjamin Ducharne, Committee Member**

Institut National des Sciences Appliquées de Lyon

**Approved by:**

Dr. Kathyne Newton

# TABLE OF CONTENTS

|  |    |
|--|----|
| TABLE OF CONTENTS.....                               | 3  |
| LIST OF TABLES.....                                  | 5  |
| LIST OF FIGURES .....                                | 6  |
| GLOSSARY .....                                       | 9  |
| ABSTRACT.....  | 10 |
| CHAPTER 1. INTRODUCTION .....                        | 12 |
| 1.1. Statement of the problem.....                   | 12 |
| 1.2. Scope .....                                     | 13 |
| 1.3. Significance .....                              | 13 |
| 1.4. Research question.....                          | 14 |
| 1.5. Assumptions .....                               | 14 |
| 1.6. Limitations.....                                | 14 |
| 1.7. Delimitations .....                             | 15 |
| CHAPTER 2. REVIEW OF LITERATURE .....                | 16 |
| 2.1. Electroactive polymer structures .....          | 16 |
| 2.2. Soft actuators .....                            | 20 |
| 2.3. Flexible sensors .....                          | 24 |
| CHAPTER 3. METHODOLOGY.....                          | 28 |
| 3.1 Introduction.....                                | 28 |
| 3.2 Computational simulation.....                    | 28 |
| 3.3 Elastomer material .....                         | 29 |
| 3.4 Manufacturing process.....                       | 29 |
| 3.5 Material characterization .....                  | 30 |
| 3.5.1 Experimental instrumentation.....              | 31 |
| 3.6 Dielectric electroactive polymer structure ..... | 31 |
| 3.6.1 Experimental instrumentation.....              | 32 |
| 3.7 Soft actuator .....                              | 33 |
| 3.7.1 Experimental instrumentation.....              | 34 |
| 3.8 Flexible sensors.....                            | 34 |

|            |                                       |    |
|------------|---------------------------------------|----|
| 3.8.1      | Capacitance sensor.....               | 35 |
| 3.8.2      | Resistance sensor.....                | 37 |
| CHAPTER 4. | RESULTS .....                         | 40 |
| 4.1        | Electroactive polymer structures..... | 40 |
| 4.1.1      | Permittivity evaluation.....          | 40 |
| 4.1.2      | Applied Pre-strain.....               | 42 |
| 4.1.3      | Tensile properties.....               | 43 |
| 4.1.4      | Pre-strain treatment.....             | 47 |
| 4.1.5      | Surface metrology.....                | 49 |
| 4.1.5.1    | Concentric circles path .....         | 51 |
| 4.1.5.2    | Line path.....                        | 52 |
| 4.1.6      | Actuation.....                        | 53 |
| 4.2        | Soft actuators .....                  | 56 |
| 4.2.1      | Material simulation.....              | 56 |
| 4.2.2      | Computational simulation.....         | 59 |
| 4.2.3      | Experimental test .....               | 65 |
| 4.2.4      | Applications.....                     | 69 |
| 4.2.4.1    | Open dual bellow actuator .....       | 69 |
| 4.2.4.2    | Closed dual bellow actuator .....     | 72 |
| 4.3        | Flexible sensors.....                 | 74 |
| 4.3.1      | Capacitance sensor.....               | 75 |
| 4.3.2      | Resistance sensor.....                | 81 |
| 4.3.3      | 3D printed sensors .....              | 85 |
| CHAPTER 5. | CONCLUSIONS.....                      | 87 |
| 5.1        | Electroactive polymer structures..... | 87 |
| 5.2        | Soft actuators .....                  | 88 |
| 5.3        | Flexible sensors.....                 | 88 |
| 5.4        | Future work.....                      | 89 |
| REFERENCES | .....                                 | 90 |

## LIST OF TABLES

|   |    |
|---|----|
| Table 1. Tensile test – One-layer samples .....               | 44 |
| Table 2. Tensile test – Two-layer samples.....                | 45 |
| Table 3. Tensile test – Three-layer samples.....              | 45 |
| Table 4. Tensile test – Four-layer samples .....              | 45 |
| Table 5. Tensile test – Five-layer samples.....               | 46 |
| Table 6. Key data of soft actuators displacement results..... | 68 |

## LIST OF FIGURES

|   |    |
|---|----|
| Figure 1. Structure and working principle of a soft DEAP.....                                 | 18 |
| Figure 2. Printing head for flexible materials. ....  | 30 |
| Figure 3. Manufactured dielectric electroactive polymer structure .....                       | 32 |
| Figure 4. Bellow pneumatic actuator CAD model.....  | 33 |
| Figure 5. Actuator layer composition .....  | 34 |
| Figure 6. Capacitor diagram .....   | 35 |
| Figure 7. Capacitance sensor CAD model.....   | 37 |
| Figure 8. Current flowing through the cross-sectional area of a wire .....                    | 38 |
| Figure 9. Resistance sensor CAD model .....   | 39 |
| Figure 10. Dielectric constant of printed TPU.....  | 41 |
| Figure 11. 3D Printed TPU membrane. ....  | 42 |
| Figure 12. Applied pre-strain test .....  | 43 |
| Figure 13. Printing path angles .....   | 44 |
| Figure 14. Young’s modulus of printed TPU. ....   | 47 |
| Figure 15. The pre-strain effect on electric field resistance.....                            | 48 |
| Figure 16. The pre-strain effect on the actuation.....  | 49 |
| Figure 17. Printed TPU membranes.....   | 50 |
| Figure 18. 2D Surface image – Concentric circles path sample.....                             | 51 |
| Figure 19. 3D Contour image - Concentric circles path sample.....                             | 51 |
| Figure 20. Roughness measurement - Concentric circles path sample.....                        | 51 |
| Figure 21. 2D surface image –Line path sample. ....   | 52 |
| Figure 22. 3D Contour image – Line path sample.....   | 52 |
| Figure 23. Roughness measurement - Line path sample. ....                                     | 52 |
| Figure 24. Actuation of DEAP structures .....   | 54 |
| Figure 25. Actuation of DEAP structure at 4.67 kV - Concentric circles path.....              | 55 |
| Figure 26. Actuation of DEAP structure at 5.73 kV (Parallel direction) - Line path. ....      | 55 |
| Figure 27. Actuation of DEAP structure at 5.02 kV (Perpendicular direction) - Line path. .... | 55 |

|  |    |
|--|----|
| Figure 28. 3D printed bellow pneumatic actuator. ....  | 56 |
| Figure 29. Uniaxial data fitting Mooney Rivlin – 2 parameter hyperplastic model. ....                          | 59 |
| Figure 30. Computational mesh of the bellow actuator. ....   | 62 |
| Figure 31. Fixed boundary constrains on the bellow actuator. ....  | 63 |
| Figure 32. Boundary load on the bellow actuator. ....  | 63 |
| Figure 33. Finite element analysis - bending behavior under a pressure of 25 psi. Von Mises Stress [MPa]. .... | 63 |
| Figure 34. Finite element analysis – Total displacement [mm] under a pressure of 25 psi. ....                  | 64 |
| Figure 35. Experimental test setup for the pneumatic bellow actuator. ....                                     | 65 |
| Figure 36. Displacement analysis (0 psi). ....   | 66 |
| Figure 37. Displacement analysis (5 psi). ....   | 66 |
| Figure 38. Displacement analysis (10 psi). ....  | 67 |
| Figure 39. Displacement analysis (15 psi). ....  | 67 |
| Figure 40. Displacement analysis (20 psi). ....  | 67 |
| Figure 41. Displacement analysis (25 psi). ....  | 68 |
| Figure 42. Open dual bellow pneumatic actuator CAD model. ....   | 70 |
| Figure 43. 3D printed open dual bellow pneumatic actuator. ....  | 70 |
| Figure 44. FEA - Bending-close behavior under a pressure of 24 psi. Von Mises Stress [MPa].                    | 71 |
| Figure 45. Bending-close behavior under a pressure of 24 psi. ....   | 71 |
| Figure 46. Grip functionality under a pressure of 24 psi. ....   | 71 |
| Figure 47. Close dual bellow pneumatic actuator CAD model. ....  | 72 |
| Figure 48. 3D printed close dual bellow pneumatic actuator. ....   | 73 |
| Figure 49. FEA - Bending-open behavior under a pressure of 25 psi. Von Mises Stress [MPa].                     | 73 |
| Figure 50. Bending-open behavior under a pressure of 25 psi. ....  | 74 |
| Figure 51. Grip functionality under a pressure of 25 psi. ....   | 74 |
| Figure 52. Fixed boundary conditions on the capacitance sensor. ....   | 77 |
| Figure 53. Boundary load on the capacitance sensor. ....   | 77 |
| Figure 54. Computational mesh of the capacitance sensor. ....  | 78 |
| Figure 55. Total displacement under 30 kPa – Capacitance sensor. ....  | 78 |
| Figure 56. Total displacement under 30 kPa in the Y, Z plane – Capacitance sensor. ....                        | 79 |

|  |    |
|--|----|
| Figure 57. Von Mises Stress [MPa] – Capacitance sensor. ....             | 80 |
| Figure 58. Capacitance [pF] vs Pressure [kPa] – Capacitance sensor. .... | 81 |
| Figure 59. Fixed boundary conditions on the resistance sensor. ....      | 82 |
| Figure 60. Boundary load on the resistance sensor.....                   | 82 |
| Figure 61. Computational mesh of the resistance sensor.....              | 83 |
| Figure 62. Total displacement under 30 kPa – Resistance sensor. ....     | 83 |
| Figure 63. Von Mises Stress [MPa] – Resistance sensor.....               | 84 |
| Figure 64. Capacitance [pF] vs Pressure [kPa] – Resistance sensor.....   | 85 |
| Figure 65. 3D printed capacitance sensor. ....                           | 86 |
| Figure 66. 3D printed resistance sensor. ....                            | 86 |

## GLOSSARY

- Electroactive polymers: “are polymers that undergo shape and/or dimensional change in response to an applied electrical field” (Wang et al., 2016).
- Soft actuator: “is a component or device that is responsible for moving and controlling the movement of a mechanism or system” (Chida et al., 2011).
- Flexible sensor: “structure that is capable of measuring the amount of deflection or bending” (Zhao et al., 2018)
- 3D printing: “is an additive manufacturing process that builds a three-dimensional object from a computer-aided design (CAD) model, typically by laying down many thin layers of a material in succession” (Schaffner et al., 2018).
- Dielectric material: “An electrical insulator that can be polarized by an applied electric field due to the shift of the average equilibrium positions of ions in the material. These materials are used for storing electric charge between the plates of capacitors” (Escudier & Atkins, 2019)

## ABSTRACT

Soft actuators and sensors are currently used in many industrial applications due to their capability to produce an accurate response. Researchers have studied dielectric electroactive polymers (DEAPs) because these types of structures can be utilized as actuators and as sensors being able to convert electrical energy into mechanical and vice versa. However, production of this kind of structures is complex and in general involve several steps that are time consuming. Customization of these types of structures will be ideal to enhance the performance of the devices based on the specific application. 3D printing technologies have emerged as innovative manufacturing processes that could improve fabrication speed, accuracy, and consistency with low cost. This additive manufacturing technique allows for the possibility of increased device complexity with high versatility.

This research studied the potential of 3D printing technologies to produce DEAPs, soft actuators, and flexible sensors. The study presents novel designs of these composite flexible structures, utilizing the most flexible conductive and nonconductive materials available for fused deposition modeling, achieving versatility and high performance in the produced devices. Produced DEAP actuators showed an actuation and electric resistivity higher than other electroactive structures like shape memory alloys and ferroelectric polymers. In addition, this research describes the electromechanical characterization of a flexible thermoplastic polyurethane, (TPU), produced by additive manufacturing, including measurement of the dielectric constant, percentage radial elongation, tensile properties, pre-strain effects on actuation, surface topography, and measured actuation under high voltage. DEAP actuators were produced with two different printing paths, concentric circles and lines, showed an area expansion of 4.73% and 5.71% respectively. These structures showed high resistance to electric fields having a voltage breakdown of 4.67 kV and 5.73 kV respectively. Those results are similar to the resistant of the most used dielectric material “VHB 4910”.

The produced soft pneumatic actuators were successfully 3D printed in one continuous process without support material. The structures were totally sealed without the use of any sealing material or post process. Computational simulations were made to predict the response of the designed structures under different conditions. These results were compared with experimental results finding that the theoretical model is able to predict the response of the printed actuators

with an error of less than 7%. This error is satisfactorily small for modeling 3D printed structures and can be further minimized by characterization of the elastomeric material. Besides that, two different grippers were designed based on the opening and closing movements of single bellows actuators. The functionality of both designs was simulated and tested, finding that both designs are capable lifting a heavier rigid structure.

Finally, this study presents a computational simulation of a 3D printed flexible sensor, capable of producing an output signal based on the deformation caused by external forces. Two different sensors were designed and tested, working based on a capacitance and resistance change produced by structural deformation. Computational analysis indicate the capacitance sensor should undergo change of capacitance from 3 to 8.5 pF when is exposed to 30 kPa; and the resistance sensor should experience an increase from 101.8 to 103 k $\Omega$  when is exposed to 30 kPa.

# CHAPTER 1. INTRODUCTION

## 1.1. Statement of the problem

Different types of actuators and sensors currently used in industrial applications are made using complex manufacturing processes. For example, some electroactive structures and soft actuators use elastomer films that can be made by casting, dipping, spin coating, or spraying, but these types of manufacturing processes can be time-consuming and the fabrication processes are difficult, expensive, labor-intensive and wasteful. In general, these types of devices are mass-produced to reduce their cost, but this creates difficulties in application due to the design constraints and the difficulty to modify the device for small quantities. Often, a specially designed sensor or actuator would be optimal in a given setting. However, sensor and actuator customization is rare and expensive. For example, commercial pneumatic grippers can be used with different types of jaws, but each jaw has its own limitations in motion, speed, force, etc. Generally, applications that utilize pneumatic grippers requires adaptability from the actuators to pick up and lift objects with complex shapes. In those cases, it is necessary to produce a new type of grip based on the preset restrictions in the application.

3D printing has emerged as an alternative to traditional manufacturing technologies, allowing flexibility in designs and low cost materials. This manufacturing process seeks to improve the fabrication speed and versatility of current devices. The versatility of this technology can be translated into a reduction in weight, volume, manufacturing time, customization, and cost. 3D printing allows designers to build an entire system consisting of the structure, the mechanism, the transmission, as well as the actuator without the need for additional assembly processes. In addition, this type of technology allows designers to include sensing devices during the manufacturing process, through printing or embedding sensors within the 3D printing process.

This manufacturing process have some disadvantages, just like any other manufacturing process. For example, 3D printers use 100 times more power than conventional methods and produce potentially toxic emission when are used in enclosed spaces. 3D printed objects have limitations in surface quality and could have some imperfections like airgaps or fractures due to the polymerization process of the material (Paoletti & Ceccon, 2018).

## **1.2. Scope**

The scope of this work is the manufacturing and testing of flexible materials to produce dielectric electroactive polymers, soft actuators, and flexible sensors based on additive manufacturing technologies. This research is limited to 3D printing deposition techniques. In addition, computational simulations coupling the mechanical and electrical properties of the materials to predict the actuation response were made. Computational simulations are based on experimental characterization of the 3D printed flexible and conductive material, and experimental testing is based on international standards or defined experimental methodologies, analyzing the electromechanical properties of 3D printed flexible materials and its performance as an actuator or sensor.

## **1.3. Significance**

The purpose of this thesis is to identify, analyze, and select best practices and techniques for manufacturing 3D printed flexible materials for electroactive polymer structures, soft actuators, and flexible sensors. These structures have been studied in past studies by different researchers, but this study is the first to analyze the behavior of the most flexible material that can be used in FDM to produce actuators and sensors.

3D printing of flexible materials is still a new area to explore, where 3D printed flexible structures are still in a stage of discovery and characterization. This project provides a methodology to characterize the mechanical and electrical properties of 3D printed flexible materials. The results from this research provide experimental results that can be utilized by other researchers to compare the performance of new materials or develop new designs of functional structures based on the characterized material. In addition, the study present computational simulation of the 3D printed material based on the experimental results, allowing to develop computational models to predict the behavior of manufactured structures.

This study presents different methodologies to produce 3D printed functional structures, analyzing the challenges encountered in 3D printing of flexible and conductive materials. The current study also aims to motivate researchers to design and test different 3D printed structures, as well as improve or optimize the current manufacturing processes for these structures.

#### **1.4. Research question**

Based on the problem statement, the scope and the significance, the next research question and sub-questions are made for this work:

- How can 3D printing technologies be applied to manufacture electroactive structures, soft actuators, and flexible sensors using additive deposition methods?
  - How can the mechanical and electrical properties of flexible 3D printed materials be characterized?
  - How can the mechanical and electrical response of the 3D printed devices be predicted?
  - How can the response and functionality of the 3D printed devices be characterized?

#### **1.5. Assumptions**

- All 3D printed samples are fully fused with no air gaps in the structure.
- Room conditions including temperature and humidity did not affect the printing processes.
- External mechanical vibrations, electric/magnetic radiation did not affect the printing processes.
- The level of cleanliness (particles per cubic foot) in the laboratory did not affect the printing processes.
- All 3D printing machines are in good mechanical condition.
- Material properties are maintained for all samples printed even for samples printed from different batches of the same type of filament.

#### **1.6. Limitations**

- The manufacturing process was limited to the 3D printers available on the Purdue campus and in particular the Adaptive Additive Technologies Laboratory.
- Mechanical and electrical tests were limited to the available laboratory equipment on the Purdue campus.

- Software to produce G-code (is the common name for the most widely used computer numerical control programming language) was limited to open source software.
- The resolution of the manufacturing process was limited by the 3D printer specifications.

### **1.7. Delimitations**

- Electroactive structures, soft actuators, and flexible sensors could have multiple shapes, forms, and configurations. In this project, just a few types of designs were printed and analyzed based on a preliminary design analysis. Selected materials and 3D printing techniques will be considered to define the main designs and the variations that will be studied.
- Possible applications of the printed structures are discussed but not manufactured to the corresponding characterization and testing requirements.

## CHAPTER 2. REVIEW OF LITERATURE

### 2.1. Electroactive polymer structures

Currently, many industrial applications use different types of actuators such as piezoelectric, electric motors, combustion engines, shape memory alloys, etc. In the most general and simplistic sense a good actuator only needs to exhibit high power per unit of volume or power per unit of mass (Madden, 2008). Piezoelectric, electric motor and combustion engines offer the highest power per unit of mass (specific power) of more than 500 W/kg (Hollerbach et al., 1992). However, when the required motion becomes more complex, the implementation of combustion engines and electric motors becomes problematic, requiring transmission systems and nullifying the benefits of high-power density.

Piezoelectric actuators present a challenge to couple the mechanical work out of the structure when large displacements are needed compare to the size of the actuator. Systems to amplify the displacements of this type of actuators are complex and in some cases are not enough to accomplish the requirements (Sommer-Larsen et al., 2001). Shape memory alloys utilize temperature to achieve the phase transformation of the material which also implies the requirement of cooling systems to produce actuation in a short time. The rate of actuation of this kind of actuators can be very low and its position control is difficult because of their hysteresis and stress dependent response (Pelrine et al., 2001). Electroactive polymer actuator performance is not sufficient at present to replace engines or electric motors. Although specific power is increasing with research advances (~450 W/kg) practical issues are still challenging to solve, like high voltage and pre-strain requirements (King et al., 2004). Nevertheless, this type of actuators offer large strains and stroke where complex, nonperiodic motions are required (Hunter & Lafontaine, 1992). Electroactive polymer actuators are the closest of any artificial system to reproduce muscles behavior.

For as far back as three decades, the mechanical and electrical properties of polymeric materials have been studied and characterized when the material is exposed to optical, electric, pressure, magnetic, or chemical fields. Research results has shown that the mechanical or electrical properties of some polymeric materials change when exposed to an external stimulus. For example, some of these polymers are described as “functional polymers” for their ability to change their

properties based on an external field (Lendlein et al., 2018). Electroactive polymers (EAP) are one subclass of this kind of materials. This type of materials are capable of change its geometrical dimensions when an electric field is induced, converting the electrical potential into mechanical strain. Electroactive polymers have been used to produce energy harvesting devices and sensors (Pralhad et al., 2005). Commonly, these EAP are grouped in two different sub-classes: electric and ionic (Mangla et al., 2014).

- Electric EAP's are materials in which activation is caused by electrostatic forces between two electrodes, which squeeze the polymer. These kinds of materials are able to deform and act essentially as capacitors. Electric EAP's change their capacitance when voltage is applied, making the polymer contract in thickness and extend in area because of the electric field. This sort of electroactive polymer is known as "Dry" and requires high voltages to be actuated (1 – 10 kV). However, they utilize low electrical power consumption (Bar-Cohen et al., 2017).
- Ionic EAP's are materials in which activation is caused by the displacement of ions inside the polymers. These sorts of materials are known as "Wet" and require low voltages to be actuated (1 – 5 Vdc), however higher electrical power consumption. Frequently, these ionic materials need to keep up their moisture content to perform accurately in confined applications (Bar-Cohen et al., 2017).

Each type of electroactive polymer has its advantages and disadvantages depending on the application conditions. The electric sort of EAP materials appear to be more advantageous for applications that are exposed to high mechanical strains, because of their high mechanical energy density and quick response. Otherwise, ionic materials appear to be more advantageous for microfluidics applications because of the aqueous environment and the capacity to produce high deformation at low applied voltages (Miriyeve et al., 2017).

Low elastic stiffness polymers with high dielectric breakdown strength subjected to an electrostatic field generate a large strain and act as EAP materials. These materials are known as dielectric elastomer EAPs. The structure of a soft dielectric EAP consist of a thin dielectric film, which is coated on the two sides with a conductive material. While applying a DC high voltage,  $U$  (in the range of thousands of volts), the electrodes compress the elastomeric dielectric in the thickness direction, producing a mechanical pressure. For volume to be conserved, the incompressible elastomer membrane expands in the planar directions to compensate the reduction

in thickness. The stress induced by electrostatic forces is known as "Maxwell stress" (Mohd et al., 2017).

Dielectric electroactive polymer structures are equivalent to a parallel plate capacitor as shown in figure 1. Equation 2.1 described a mathematical expression that models the working principle of this kind of structure. Based on this model, the most relevant properties of a dielectric material are the relative permittivity and thickness. The equivalent pressure applied to the dielectric material, when an electric field is induced, is directly proportional to the relative permittivity, and inversely proportional to the thickness.

$$P_{equivalent} = \epsilon_0 * \epsilon_r * \left(\frac{U}{d}\right)^2 \quad (2.1)$$

$P_{equivalent}$  = equivalent pressure

$U$  = voltage

$d$  = Thickness of the dielectric films

$\epsilon_0$  = Free space permittivity ( $8.85 \times 10^{-12}$  F/m)

$\epsilon_r$  = Relative permittivity of the dielectric material

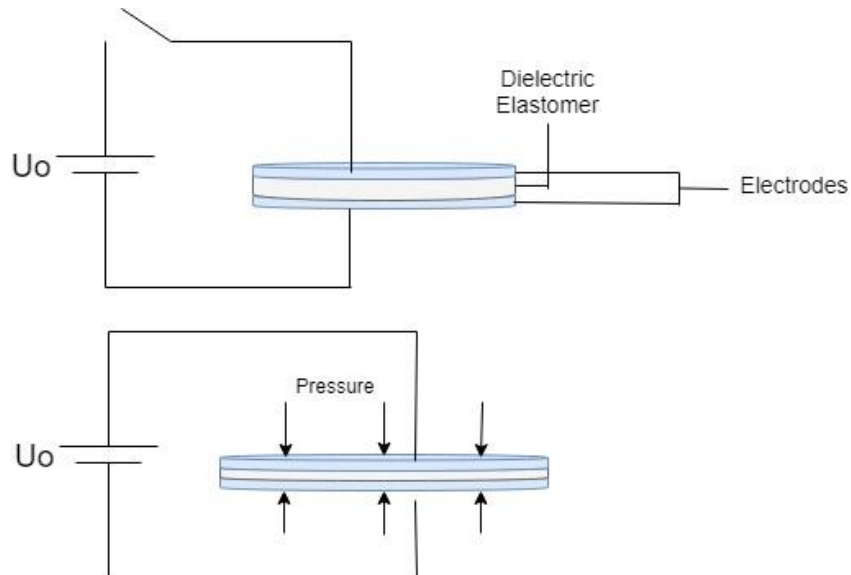


Figure 1. Structure and working principle of a soft DEAP. (Gonzalez et al, 2019)

DEAP structures presents two states. The structure will remain in a non-polarized state as long as it is not exposed to an electric field. When the structure is exposed to an electric field, it changes to a polarized state where the elastomeric material is compressed reducing its thickness and compensate with an expansion in the plane directions. This type of structures can be actuated in two unique direction in which the motion of the structure can be utilized: the thickness direction utilizing the structure as a contractile actuator, or the planar direction utilizing the structure as an extending actuator.

Pre-strain treatments are commonly used in dielectric materials when are used in electroactive actuators. This treatment improves the overall performance of the structure and enhance the dielectric breakdown of the elastomer material (Ha et al., 2006). In addition, this process is used to increase the response speed, induce preferential expansion when the elastomer is asymmetrically stretched, and reduce the thickness of the dielectric film (Mok Ha et al., 2008). Generally, two different pre-strain treatments are used in dielectric materials of electroactive polymers: mechanically, and chemical. Mechanical treatment provides significant challenge during the manufacturing process, since this mechanical pre-strain must be maintained during the subsequent processes and during application (Newell et al., 2018). Chemical treatment involves several steps and requires impregnating the dielectric material with polymerizable and crosslinkable liquid additives to pre-strain and cure the elastomeric polymer (Ha et al., 2006).

A variety of actuator configurations have been developed to exploit the capabilities of dielectric elastomers while addressing their unique challenges. These configurations range from simple bending beam, diaphragm or stacked structures (Kornbluh, 2008). Rosenthal & Pei studied the motion and production of multiple-degrees-of-freedom (multi-DOF) spring roll actuators. These actuators have been developed by patterning electrodes on dielectric films having radial alignment on multiple on multiple spans that are wrapped around a compression spring. They present different application of roll actuators, like walking robot and serpentine-like motion robot, and demonstrated its potential to be used un aquatic robotic systems (Aaron Rosenthal & Pei, 2008).

To increase the absolute deflection of dielectric elastomer actuators at limited driving voltage, thin dielectric films and elastic electrodes are stacked on top of each other using a multilayer fabrication technology (Schlaak et al., 2008). Kovacs et al.'s presented a novel approach for active structures driven by soft dielectric electroactive polymers. The proposed active structure

is composed by thin dielectric films, pre-strained using chemical treatments, and conductive electrodes stacked on top of each other. The dielectric films are arranged in a pile-up configuration between the electrodes. The actuator works based on the contraction effect of the dielectric films when an electrostatic field is applied. Manufactured actuators showed significant actuation performance being capable of lift 15 kg with a contractive deformation of 18%, when were exposed to 4.5 kV (Kovacs et al., 2009). Carpi & De Rossi present two different types of contractile multi-layer linear actuators utilizing helical and folded configurations. Prototype samples were fabricated with silicone elastomer finding that the maximum contraction for the helical actuators was 5% for a field of 14 V/ $\mu\text{m}$ , and for the folded actuator was 10% for a field 10 V/ $\mu\text{m}$  (Carpi & De Rossi, 2008).

One of the most recent studies of this type of structures was presented by Zhu et al.'s. They proposed a semi-rigid ring-shaped electrode layout for an out-of-plane buckling actuator using a dielectric electroactive polymer (DEAP) membrane. The electrodes were patterned around the flexible membrane as a ring, rather than usual compliant electrodes which cover the whole membrane. The membranes showed a linear increase of the deflection as a function of the electric field strength for fields larger than a threshold field in the order of 70 V/ $\mu\text{m}$  (Zhu et al., 2019). Currently, researchers are trying to implement innovative manufacturing process to improve the fabrication of this type of actuators, utilizing novel configurations and designs, and are also studying the behavior of this actuators by finite element analysis (FEA).

## **2.2. Soft actuators**

During the past few decades, robots have been increasingly used in modern industrial applications. The automotive industry has been modernized constantly by the use of robots, specially in the assembly area (Shepherd et al., 2011). Notwithstanding, in the most recent decade, research and industry have begun to investigate and create robots for new application areas. Robots have characteristics that can be severe limitations in certain circumstances. The most important limitation is that robots are classified as “non-collaborative”, which means that they are not able to work safely in close contact with humans or other fragile objects (Whitesides, 2018). Generally, robots are heavy and hard and are designed to move rapidly, to apply large forces, and to handle dangerous tools. Robots are built largely of noncompliant materials. As a result, they must be positioned accurately to perform their tasks, and they are generally not able to adapt

autonomously to different shapes and tasks (Hashemi et al., 2020). In the past two decades, researchers have tried to optimize the functionality of these structures improving the adaptability, cost, weight, and thermodynamic efficiency of robots (Laschi et al., 2017).

Currently, robots are utilized in predominantly human domains and are gaining acceptance for use in close proximity interactions with humans to either assist human operators or work cooperatively with them. This conceptual change in the utilization of a robot has brought about advancements in materials and manufacturing processes, attempting to get closer to biologically inspired structures and creating a new subfield in robotics called “soft robotics”. The soft robotics field has increased in the past few years, providing new kinds of structures that can produce intricate controlled movements to accomplish specific tasks. These kinds of structures are more suited to direct human interaction due to the use of soft materials. Soft actuators are flexible, adaptable, and versatile structures that are generally made of flexible elastomeric materials (Davis, 2018). This type of actuators offers to the user simpler operation, lower cost, and greater durability. Soft actuators are often fabricated from a single piece of flexible elastomer and have no frictional surfaces at joints or bearings, reducing its maintenance (Liu et al., 2020).

One of the most common actuator design that researchers have attempted to study and replicate, through the use of soft actuators, is human-like organic muscles. The drive to produce an organic-like actuator originates from the capacity of the human muscle to perform accurate positional movements and support external loads through compression and expansion of highly flexible structures (Miriyeve et al., 2017). Soft robotic systems seek to solve the need for robots that can safely work and interact with humans. This type of device deforms continuously along its structure using flexible materials enabling the system to change shape safely when interacting with humans or obstacles. Currently, researchers of different fields are working in the development of new materials and advanced manufacturing techniques to improve soft actuator performance, and manufacturability. Soft robotics have developed new types of robotic technologies like robotic grippers, surgical systems, and assistive and rehabilitation exoskeletons (Krause et al., 2018).

The capability of soft robots strongly depends on the performance of their actuators. Soft actuators have been studied and produced in the past two decades, and it has been found that this type of actuators have several advantages over traditional actuators. Usually, traditional actuators are limited to a specific range of motion, reducing their degrees of freedom. Conversely, soft actuators can provide large range of motion with multiple degrees of freedom based on design

characteristics such as: geometry, material, and their control system (Krause et al., 2018). Commonly, soft actuators can be actuated in two ways: using smart materials or a working fluid that can be compressible or incompressible.

Smart materials are still an exploratory field. This type of actuation has some disadvantages like limitations in the output force, low efficiency, low stability, short lifetime, and high cost. Soft pneumatic actuators are widely used in robotics and automation because they can provide a large range of movements and high-power densities. In addition, pneumatic actuation that uses air as the working fluid is preferred over hydraulic or other fluids in gaseous form because they are simpler, low-cost, biocompatible, environmentally friendly and safe. However, there are performance limitations due to the compressibility of air. It is more difficult to apply accurate finite control using air in pneumatic circuits (Hu et al., 2018). Soft pneumatic actuators operate by applying positive or negative controlled input pressure to a sealed channel inside a flexible structure. These types of actuator can bend, twist, extend, or contract depending on the geometry, material, and boundary conditions. Current soft pneumatic actuators reported in the literature can be classified in three major groups, according to their degrees of freedom: a) one dimensional: extension and expansion; b) two dimensional: bending motions; c) three dimensional: rotating motions and complex movements (Hu et al., 2018).

Human and animal muscles have the ability to support large external loads while performing accurate positional movements, through expansion and contraction of muscle tissues. For this reason, human-like organic muscles are one of the most common actuator designs that researchers have tried to study and copy (Miriyeve et al., 2017). Numerous types of soft pneumatic actuators exist in research and application. The first pneumatic actuator was patented by Alexandre Morin in 1953 (Morin, 1953). The actuator has an elastic diaphragm adapted to be subjected to the pressure of any fluid and adjusted to transmit any change in the pressure of the fluid. The McKibben artificial muscle actuator is the most frequently used and researched actuator with one dimensional movement in robotics applications. This actuator has a simple structure consisting of an internal elastic tube surrounded by a braided sleeve. The tube ensures the internal pressurization of the fluid during the deformation that occurs when the actuator is supplied with compressed air, while the braid controls the expansion of the tube and enables the radius to increase and produce an axial contraction (Belforte et al., 2014).

In the last few decades, researchers have worked to characterize this type of actuator and improve its performance. In 1986, Takeo Takagi proposed an actuator provided with a protective layer between the tubular body and the braided structure to prevent damage to the tube (Belforte et al., 2014). In 1988, Mirko Kukulj patented an actuator capable of reducing the friction forces between the fibers of the sleeve (Kukulj, 1988). In 2005, Donald et al.'s patented an actuator whose sheath of braided fibers was designed to be impregnated with liquid lubricants to reduce the friction and abrasion between the elastic tube and the sheath.

Dr. George Whitesides and his research group designed and studied different types of pneumatic actuators using biomimetic principles. In his research, he has developed partially or entirely soft robots fabricated with elastomeric polymers that do not use a rigid skeleton to provide mechanical strength. His designs use networks of channels in elastomers that inflate like a balloon for actuation. Using a series of parallel chambers embedded in elastomers as a repeating component and then stacking or connecting these components enabled his team to manufacture structures that produce complex motions. These manufactured actuators were able to perform an actuation strain of 20% at 500 g loading. For comparison, the corresponding value of a human skeletal muscle is approximately 40% (Yang et al., 2016). In 2011, he presented a manuscript that described a quadrupedal soft robot that used five actuators and a simple pneumatic valving system that operated at low pressures (<10 psi). The robot was manufactured using soft lithography, using a 3D printer to fabricate molds from which the quadruplet was replicated (Sphepherd et al., 2011). Additionally, in 2014 he presented a pneumatic mobile soft robot using composites of silicone elastomer, polyaramid fabric, and hollow glass microspheres. The robot was manufactured using mold casting. The robot has autonomous operation being able to produce elevated pressures up to 138 kPa to actuate its legs and hold payloads of up to 8 kg (Tolley et al., 2014).

Soft actuators are commonly fabricated through mold casting of elastomeric materials, typically silicone rubber. This manufacturing process generally involves manual processing after the material is cured, increasing cost, time, and labor. Molding processes restrict design complexity and hinder design changes. In a recent study, Benjamin Keong presented five different types of pneumatic actuators fabricated using fused deposition modeling (FDM) technology (Keong et al., 2018). FDM is a more cost-effective, automated, and simple method of soft actuator fabrication. In addition, the application of 3D printing techniques allows for more complex designs of

pneumatic actuators with improved performance through higher output force and achievement of more complex movements.

Recent advances in 3D printing technology have improved the manufacturing process in terms of resolution, speed, cost, and materials. This has enabled the rapid fabrication of highly customizable soft flexible actuators. 3D printing has become an important technology for advancing the emerging field of soft robotics. The research community has used 3D printing technology to fabricate new custom designs for soft actuators and sensors, even incorporating smart materials such as dielectric electroactive polymers (Dong et al., 2018). 3D printing has been commercially available for almost two decades with continuous improvement in printing techniques (e.g., improved resolution, speed, automatization, and new innovative materials). Currently, 3D printing advances enable rapid prototyping of elastomer structures that are not printable through existing soft lithography techniques (e.g., non-planar cross section) (Hwang et al., 2015). In addition, 3D printing techniques allow for the design of improved internal features of the manufactured devices and have more control of the mechanical properties of the structure and its performance.

3D printing of flexible materials is still a new area of research. Nowadays, only one type of elastomeric material can be printed with a limited range of degree of elasticity, that depends on the chemical formulation used by the manufacturer (Verl et al., 2015). Flexible materials available for 3D printing materials have several limitations when implemented in 3D printing processes. In the case of FDM technique, elastomer materials are difficult to print, have poor bridging characteristics, low printing speed, and may not work well on Bowden extruders (a type of filament feeding mechanics used in many FDM 3D printers) (Soreni-Harari et al., 2020). There is a necessity to explore and develop solution to improve the printing process of elastomeric materials. This research describes the best practices for 3D printing of flexible materials, analyzing the extruder mechanism, feed rates, and optimization of travel movements.

### **2.3. Flexible sensors**

Sensors are employed to monitor and detect the changes to external fields or conditions in the surrounding environment. They are used to collect data that is difficult to obtain from inaccessible or partially accessible locations. Some sensing devices can store and analyze the collected data (Nag et al., 2019). The classification of sensors can be done in two categories

depending on the type of materials used to fabricate them, flexible and non-flexible. Flexible devices are fabricated from malleable materials and have a wide range of deformation without permanently changing its properties. Non-flexible sensors were developed earlier among which the ones developed with silicon substrates are the most popular (Amjadi et al., 2015).

The most common sensors used in industry applications are non-flexible. While very useful for many applications, there are certain disadvantages associated with these sensors like their brittle nature, stiffness, which deters their usability (Yang et al., 2018). These disadvantages are more prominent, especially when the sensing system is deployed for monitoring physiological parameters of a person or any other uses which involves any strain applied on the sensor (Nag et al., 2019). During the last decade, flexible sensors have been studied and produced with improved mechanical and electrical properties for applications where non-flexible sensors are not ideal. Flexible prototypes have demonstrated great potential to be used in many industrial applications such as environmental, chemical, healthcare, biomedical, and aviation sectors (Liu et al., 2018). This type of structures can be applied to soft and irregularly shaped surfaces such as human skin or textile fabrics (Nag et al., 2019).

Different types of manufacturing techniques can be used to fabricate flexible sensors that differ in resolution, speed, cost, and materials (Nag et al., 2019). Some of the most common manufacturing techniques are: photolithography, screen printing, 3D printing, ink-jet printing, and laser cutting. 3D printing is significantly more versatile and less expensive than conventional lithographic methods improving manufacturing time of proof of concept models and allowing for production of multi-material final products with high complexity. This additive manufacturing method has been used to manufacture electronic devices layer-by-layer, enhancing controllability and tunability over the structure (Li et al., 2018). 3D printers have become a viable cost-effective approach for design and development of flexible sensors with complex geometries (Hamzah et al., 2018). However, there remains a very long road toward the full utilization of 3D printing technology to realize a truly unique 3D printed flexible electronic device due to the limitation of functional 3D printing materials (Yang et al., 2018).

Novel multi-functional materials, also known as “smart materials”, have been preferred and used in research to produce flexible sensors. The coupling between the material and its active elements is like a classical mechanical coupling of two structures down to the level of molecular interactions. Those interactions make the materials and structures with built-in sensing or actuation

functions, dependent on the properties of the active elements (Boller, 2001). The vast majority of the studied flexible sensors used conductive materials. Researchers have created different types of flexible conductive materials, mixing flexible polymer matrixes with active particles of conductive materials such as carbon nanotubes, aluminum, graphene, and graphite. Similarly, researchers have created other conductive materials like gels, inks, and rigid filaments; that are also used in flexible sensor designs with lower thickness values (Boller, 2001).

Leigh et al. developed a formulation of a simple conductive thermoplastic composite called “carbomorph” demonstrating how it can be used in a commercial 3D printer to produce electronic sensors able to sense mechanical flexing based on capacitance changes. This novel material was composed of conductive carbon black (CB) and polycaprolactone (PCL), using a loading of CB in the composite of 15 wt%. They conclude that higher loadings of CB produce a filament with higher diameter and roughness that compromises the quality and resolution of the print. They successfully produced usable 3D printed flexible sensors, capacitance buttons, and capacitance smart vessels (Leigh et al., 2012). Additionally, the research presented by Kwok et al. describes the fabrication of an electrically conductive filament used for the production of 3D printed circuits and sensors. The conductive material was composed of homopolypropylene and CB, using a loading of CB in the composite of 20.4 wt%. The produced material shows stability in the electrical properties under exposure to sunlight over one month and no degradation was observed in terms of electrical resistance (Kwok et al., 2017).

One of the most common flexible sensors that researchers have studied is the stretchable tactile sensors. This type of sensor is a multifunctional device able to convert mechanical strain into electric potential and viceversa (like DEAP structures) and can be applied to produce wearable electronics and energy harvesting. Guo et al. designed and fabricated a stretchable tactile sensor combining nanocomposite conductive inks and silicone ink. They were able to develop sinter-free inks with adjustable viscosities and electrical conductivities. The customized sensor demonstrated capabilities of detecting and differentiating human movements, including pulse monitoring and finger motions. The electrical sensing behavior of the printed tactile sensor was evaluated finding that when the applied pressure increases from 100 to 500 kPa, the resistance of the device decreases from 1.14 K $\Omega$  to 95  $\Omega$  (Guo et al., 2017).

Another type of stretchable sensor was presented by Li et al. In this work, they report the successful fabrication of a stretchable capacitive sensor using a novel 3D printing method for

highly sensitive tactile and electrochemical sensing applications. The sensor utilizes a mixture of carbon nano tubes (CNT) and polydimethylsiloxane (PDMS) as conductive material. They were able to print the flexible sensor using a 3D printer with a liquid deposition mechanism, where conductive and nonconductive material were printed on glass substrate at room temperature. Printed capacitance sensors were able to increase its capacitance value from 4.93 to 20.67 pF when the gap between electrodes decrease from 3 mm to 1 mm. In addition, the developed sensor exhibited a detection limit as low as  $1 \times 10^{-6}$  M for NaCl aqueous solution (Li et al., 2018).

An interesting application for 3D printed sensors is presented by Shih et al. This study presents 3D printed resistive soft sensors, with different geometries, embedded in a soft robot body improving their exteroception and interoception capabilities. They characterized linear, planar, and 3D sensors, manufactured using nonconductive (TangoPlus FLX930) and conductive (TangoBlackPlus FLX980) commercial photopolymers. The conductive resin contains carbon particles which provide a measurable conductivity. 3D printed resistive sensors showed an increase of its resistance value from 0.5 M $\Omega$  to 1.65 M $\Omega$  when the pressure increases from 200 to 600 kPa (Shih et al., 2018).

In the future, devices that use these types of flexible sensors could include real-time functionalities, supplemented with a feedback control loop, for applications in the measurement and control of environmental conditions, biological applications, and the movement and deformation of structures, etc. (Han et al., 2019). Innovation of advanced manufacturing techniques provide new opportunities for fabrication of wearable devices that can be adjusted to the needs of each user, adapting its structure to pre-established topologies and integrating multiple smart materials with coupled functionalities.

## **CHAPTER 3. METHODOLOGY**

### **3.1 Introduction**

The methodology used in this study combines computational simulations and experimental tests, where both results were compared in order to validate a theoretical model. On the other hand, some experimental tests were performed to characterize the dielectric printed material and obtain the corresponding mechanical and electrical properties. These values were used as input parameters in the computational simulations. The project started studying some basic designs, being the simplest and easiest designs to understand and test. This is a progressive cycle in which more complex structures were designed and tested, based on the information gained in terms of the theoretical and experimental characterization.

### **3.2 Computational simulation**

The computational simulations were made using COMSOL Multiphysics® version 5.4 software. This is a general-purpose simulation software for modeling designs, devices, and processes in all fields of engineering. In this process theoretical models were developed to characterize the actuation of electroactive structures, soft actuators, and flexible sensors under different conditions. Two modules were used to create the computational simulations: electromagnetics, and structural mechanics. This software allows to define the multiphysics coupling between modules. In this case, the modules are coupled by electromechanical forces to model electromechanical interaction between deformable solids and electric fields, particularly in this case when the deformation of the structure can significantly affect the electric field distribution. Computational models used experimental data obtained from 3D printed samples during the electromechanical characterization process. Stress and strain data were fit with known hyperplastic models to predict deformation in a constructed Mooney-Rivlin model.

For the electroactive polymer structures, the principal objective is to describe the actuation of the structure coupling the mechanical and electrical properties of the different materials. On the other hand, for the soft actuators the principal objective is to describe the actuation of the structure coupling the mechanical properties of the structure with the properties of the fluid and its interaction. Finally, the objective for the flexible sensors is to describe the sensitivity of the

structures, coupling the mechanical and electrical properties of the different materials, based on the deformation of the hole structure. All components of the simulated structures were modeled using solid tetrahedral elements. This type of element is commonly used in engineering practice because is able to mesh almost any volume regardless of complexity (Payen & Bathe, 2011).

### **3.3 Elastomer material**

Flexible filaments are made of thermoplastic elastomers (TPE) which are a mixture of hard plastic and rubber materials. This type of material is elastic in nature allowing the plastic to be stretched and flexed easily. There are several types of TPE, with thermoplastic polyurethane (TPU) being the most commonly used among 3D printing filaments. TPU is a flexible, abrasion and oil resistant thermoplastic that is used in many manufacturing processes for industrial use. This material is durable and has the ability to withstand ambient temperatures of up to 80 degrees Celsius.

TPU was selected to manufacture all structures designed and studied in this research. The most flexible and elastic TPU material available in the market is called “X60 Ultra Flexible Filament”. This material is made of TPU and has a shore hardness of 60A, being much softer than other flexible materials available on the market. This material can produce highly functional parts for applications that require flexibility and stretchability (Thermoplastic Polyurethanes, 2019).

### **3.4 Manufacturing process**

Fused deposition modeling (FDM) was selected based on the available resources (3D printers and materials), and suitability for DEAP, soft actuator, and flexible sensor production. The working principle of this technology is based on material extrusion through a heated extruder. The printing head follows a specific path dictated by a G-code, building the desired part layer by layer (Schlaak et al., 2008). The heated extruder ejects material in liquid or semi-liquid state, utilizing a feeding mechanism based on the rotation of grooved idler-wheels that compress and pull the filament. The 3D printer “Lulzbot Taz 6” was utilized to produce the structures designed using a specialized extruder head with modifications being capable to print flexible materials. The specialized extruder head was constructed with 3D printed rigid parts, using ABS, and one set of dual extruders for flexible materials called “Flexion Extruder”. Those extruders can print flexible

filament at least twice as fast as the regular extruders (70 mm/s). In addition, the specialized extruder has a self-cleaning drive composed by a brush that constantly clears the drive roller of plastic shavings, keeping the teeth sharp to drive filament consistently. All samples were printed using the same 3D printer, material, and printing settings (layer height: 0.15 mm, infill density: 100%, printing temperature TPU: 205 °C, printing temperature ETPU: 220 °C, build plate temperature: 60 °C, printing speed: 10 mm/s; no support material).

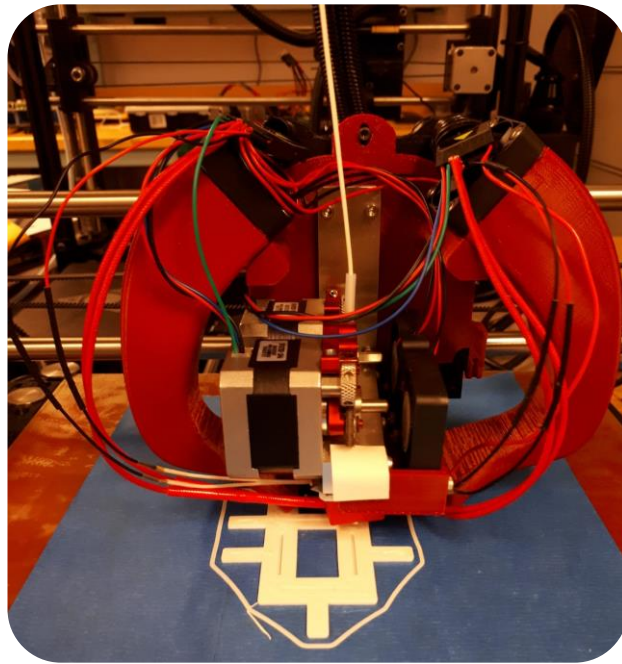


Figure 2. Printing head for flexible materials.

### 3.5 Material characterization

The 3D printing process gives anisotropic properties to the printed structure due to the different printing orientations of the material during the manufacturing process. This manufacturing process print layers of material on top of each other, made of continuous printed lines, causing the structure to possibly have internal voids, imperfections, or discontinuities that directly affect the mechanical response of the printed structure. For this reason, is important to characterize the electrical and mechanical properties of the material after going through the 3D printing process. This study presents the characterization of the TPU material including: tensile

properties, percentage of radial elongation, measurement of the dielectric constant, and surface topography.

### **3.5.1 Experimental instrumentation**

- a. Tensile Test
  - i. MTS Criterion - Model C45.605
- b. Percentage of elongation Test
  - i. Omnidirectional Iris Stretcher
- c. Dielectric constant
  - i. Agilent 4263B LCR Meter
- d. Surface topography
  - i. Bruker Contour Elite K
  - ii. Microscope Nikon Eclipse LV100ND

### **3.6 Dielectric electroactive polymer structure**

The electroactive structures can be used in two different ways: as a sensor and as an actuator. In this study, the electroactive structures were tested and analyzed as an actuator, measuring the expansion of the structure when exposed to high voltage. For the actuation test each structure was connected to a high voltage supply, using conductive material between the electrodes and the voltage output. The structures were exposed to a voltage between 0 and 10 kV, using an increasing step of 10 V. Actuation data was processed using the Tracker 5.1.3 software and analyzed for visible and measurable changes in the physical size of the electrode layer during exposure to high voltage. Tracker is a free video analysis software capable of calculating deformations. This software allows the user to create particle models based on Newton's law. The calibration is based on image distance in pixels between two points, and defined an appropriate coordinate axes to analyze the displacement of certain point (Brown, 2019)

Carbon conductive grease (MG Chemicals® #846) was used to produce the electrodes in the DEAP structures. The electrodes were painted manually because the study is interested in evaluation and characterize the performance of 3d printed dielectric material. This is also the traditional manufacturing method for research in this field. Utilizing a 3D printer to print the electrodes will increase the variables to consider in the performance of the actuators. The

electrodes were painted on both sides of the elastomer material having a diameter of 50 mm. The voltage supply could be connected directly to the electrodes, however that connection would not be the best. Copper tape was used to enhance the connection and conductivity between the electrodes and the high voltage supply. This method is also the traditional baseline test for EAP materials and therefore provided comparability to other works. The elastomeric membranes were stretched to induce the desired pre-strain utilizing the Omnidirectional Iris Stretcher. This machine is an automated uniform stretcher for flexible materials, controlled by the software LabView. The high torque stretcher is capable of pre-straining materials with a minimum diameter of 25.4 mm (1 in) to a maximum diameter of 406.4 mm (16 in). The stretcher calculates the percent strain and has adjustable speed control through a high torque micro-stepper motor and controller (Romo et al., 2018).

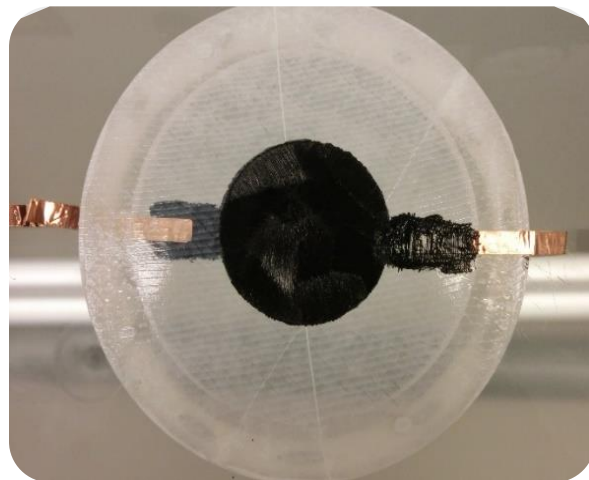


Figure 3. Manufactured dielectric electroactive polymer structure

### **3.6.1 Experimental instrumentation**

1. Manufacturing process
  - i. Lulzbot Taz 6
  - ii. Omnidirectional Iris Stretcher
2. Actuation Test
  - i. TREK 610E High Voltage Supply

### 3.7 Soft actuator

The proposed soft actuator was designed based on Keong et al.'s fold-based pneumatic actuator (Keong et al., 2018). The design consists of a fold-based structure with a sine wave-like shape. The bottom part of the bellow actuator has a wall with a thickness of 1 mm, increasing the resistance to deformation in the negative z-direction (see Figure 4).

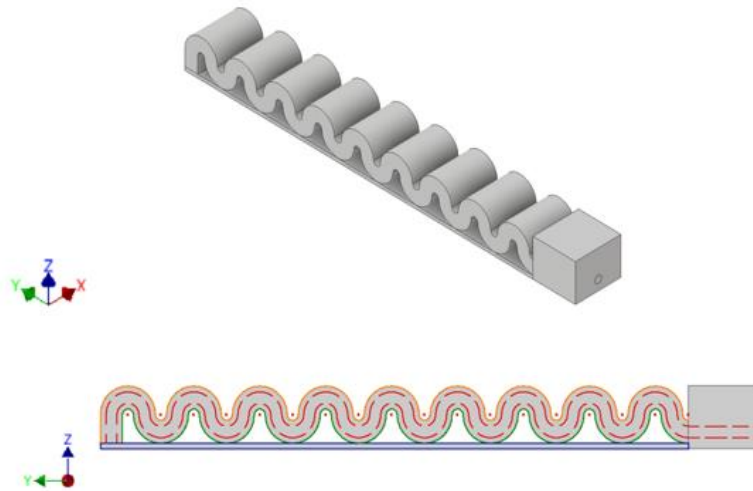


Figure 4. Bellow pneumatic actuator CAD model (Orange line represents the top part of the bellow actuator; Red lines represents the internal channel; Green line represents the bottoms part of the bellow actuator; Blue lines represents the wall in the bottom part of the actuator).

The bellow actuator has an internal channel across the entire length of the actuator. In addition, the internal channel has a circular input port where the line of compressed air is connected providing pressure to the entire internal structure. The input port has a diameter of 2 mm, making the connection to a probe sufficiently tight to have a fully sealed actuator with minimal air leakage.

The entire structure is composed of three regions. The first and third region are a multi-layer zone with a thickness of 2 mm. These layers provide support to restrict actuation in the positive and negative x direction, forcing the actuator to be expanded preferentially in the top layer. The second region is a multi-layer zone with a thickness of 12 mm. This region forms the walls of the actuator and bounds the internal channel. The yellow, blue, and red circles in Figure 5 represent the first, second and third region respectively.

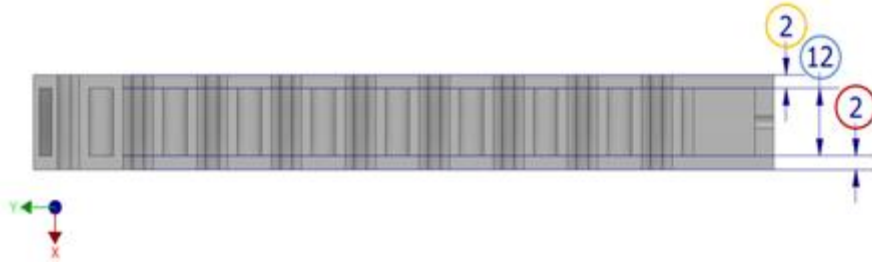


Figure 5. Actuator layer composition (dimensions in mm).

In contrast with previous designs, this actuator has different dimensions in the wall thickness, in the width of each of the three sections that composed the structure, and the profile at the end of the actuator has a different shape. Those changes improve the performance of the actuator resulting in the actuators being able to achieve greater deformation with less pressure. In addition, the end of the actuator will have a higher deformation that improves the grip of the actuator. Actuation data was processed using the Tracker software and analyzed for visible and measurable changes in the physical size of the actuator during the pressurization process with compressed air.

### 3.7.1 Experimental instrumentation

1. Manufacturing process
  - i. Lulzbot Taz 6
2. Actuation Test
  - i. Pressure transmitter (Wika A -10)
  - ii. National Instruments USB data acquisition system (NI DAQ 6212)

### 3.8 Flexible sensors

The sensors designed here are structures composed of two different materials. One of them is a nonconductive hyperelastic material, TPU (X60) and the other one is a conductive linear elastic material (ETPU). The hyperplastic material will function as a membrane that is deformed by external forces. The conductive material is attached to the membrane, being exposed to the deformation of the membrane also propagates deformation to this material. The deformation

caused in the conductive material will affect the electrical properties of the structure. This relationship can be utilized as a deformation sensor.

Al-Rubaiai et al. characterized the mechanical properties of a commercial flexible conductive filament made from a special TPU compound material with a carbon black filler (Al-Rubaiai et al., 2019). The material is called “ETPU”. They conclude that this conductive material behaves as a linear elastic material, with an excellent stretchability over 200%. The manufacturing company “Palmiga Innovation” reports a Young’s modulus of 12 MPa based on the standard ASTM D-638; a resistivity of  $750 \Omega \cdot \text{cm}$ ; Poisson’s ratio of 0.49, and a density of  $1.30 \text{ g/cm}^3$  (PI-ETPU, 2020). This material was selected in this study based on the good mechanical and electrical properties that make this material ideal for conductive 3D printed flexible elements.

### 3.8.1 Capacitance sensor

This type of sensor is a flexible structure that changes its capacitance due to the deformation caused by external forces. The capacitor can be represented by a parallel plate capacitor as shown in Figure 6. The capacitor is composed by two electrodes and one dielectric material between them.

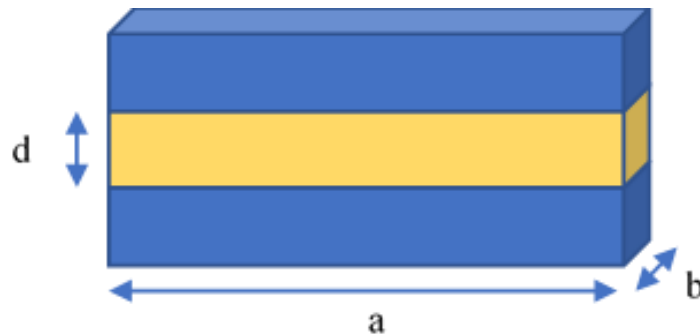


Figure 6. Capacitor diagram. Electrodes are represented in blue; and the dielectric is represented in yellow.

This structure is able to store a charge on its conductive plates which gives its capacitance value. The characteristic capacitance of the structure represents the capacitor’s ability to store an

electrical charge on its plates. The capacitance of the structure can be calculated using the following expression:

$$C = \frac{\epsilon_0 \epsilon_r A}{d} \quad (3.1)$$

where,

$C$  = capacitance value

$A$  = area of the plates in contact with the dielectric material

$\epsilon_0$  = free space permittivity ( $8.85 \times 10^{-12}$  F/m)

$\epsilon_r$  = relative permittivity of the dielectric material

$d$  = distance between the electrodes

Equation 3.1 shows that the capacitance value of the structure is determined from the dimension of the electrodes, the distance between them, and the properties of the dielectric material. In the structure showed in Figure 6 the “A” value is equal to “a x b”.

Based on the above, we designed a sensor maximizing the area of the electrodes and distributing the electrodes over the membrane taking advantage of the produced deformation to reduce the distance between the electrodes. The reduction in the distance between the electrodes increases the capacitance value of the structure. Figure 7 shows the CAD model of the capacitance sensor designed.

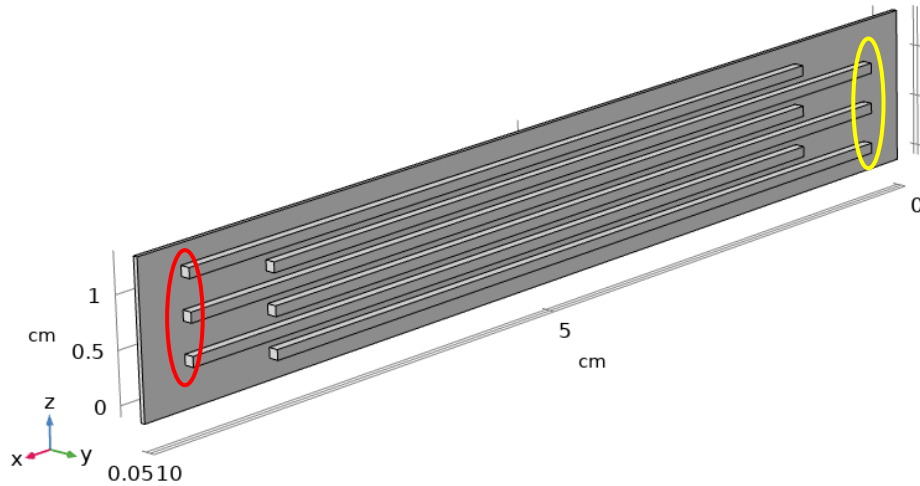


Figure 7. Capacitance sensor CAD model.

The electrodes have an offset of 1 cm between them, in the x axis, to identify the electrodes that are connected between them. In Figure 7, the red ellipse represents the connections of electrode one; and the yellow ellipse represents the connections of electrode two. The electrodes have a distance between them of 1 mm, which mean that air will function as dielectric material. The membrane has a cross-sectional area of 0.45 mm x 15 mm, with a total length of 10 cm. Each line of conductive material that compose the electrodes has a cross-sectional area of 1 mm x 1 mm. The length of each line of conductive material is 8 mm. In this design the dielectric material between each line of the electrodes is air.

### 3.8.2 Resistance sensor

This type of sensor is a flexible structure that changes its resistance due to the deformation caused by external forces. The electrical resistance of an object is a measure of the difficulty of flow of an electric current. Figure 8 shows a diagram of a wire in which current is applied on the cross-sectional area.

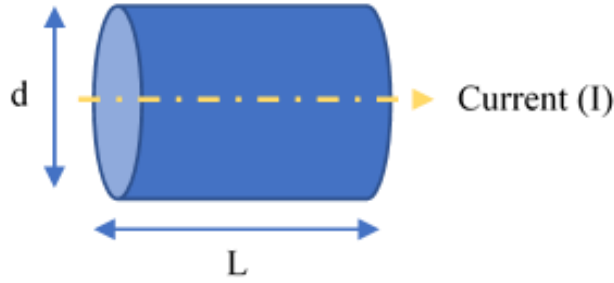


Figure 8. Current flowing through the cross-sectional area of a wire.

The resistance in a wire can be calculated by the following expression:

$$R = \frac{\rho L}{A_I} \quad (3.2)$$

where,

$R$  = resistance

$\rho$  = resistivity of the material

$L$  = length of the wire

$A_I$  = area where the current is applied

Based on the above, the sensor was designed with one continuous conductive element attached to a flexible membrane, creating an electromechanical interaction between the deformable membrane and the electric field of the conductive element. The deformation in the conductive element increases the length of the resistor and decreases the diameter causing the resistance value of the structure to increase. Figure 9 shows the CAD model of the resistance sensor designed.

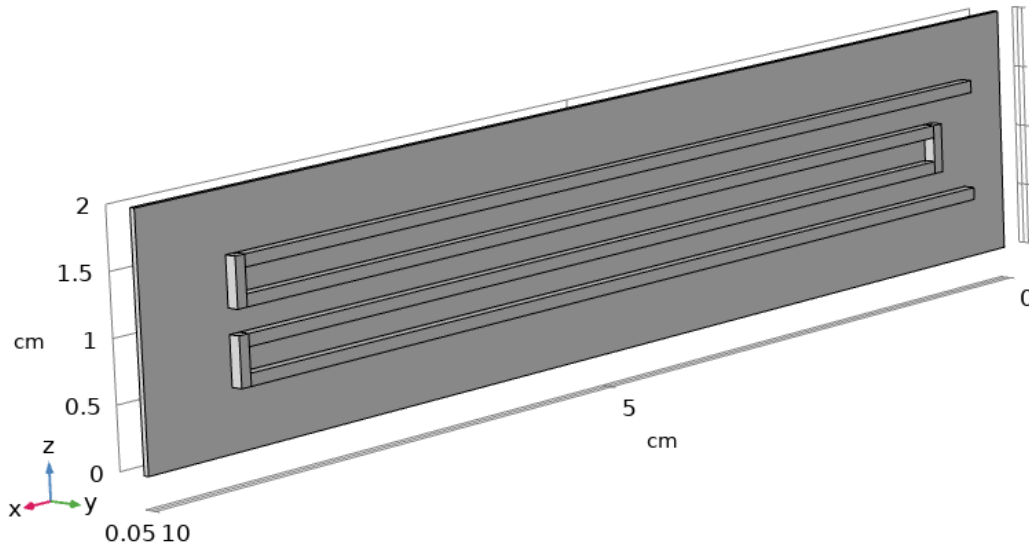


Figure 9. Resistance sensor CAD model.

The conductive element has a cross-sectional area of 1 mm x 1 mm and a total length of 34.2 cm. The membrane has a cross-sectional area of 0.45 mm x 20 mm, with a total length of 10 cm.

## CHAPTER 4. RESULTS

### 4.1 Electroactive polymer structures

This study presents a production method for dielectric electroactive polymer structures using additive manufacturing. In addition, a methodology to characterize the mechanical and electrical properties of 3D printed flexible materials is presented. The electromechanical characterization consists of measurement of dielectric constant, percentage of radial elongation, tensile properties, pre-strain effects on actuation, surface topography, and measured actuation under high voltage.

#### 4.1.1 Permittivity evaluation

Dielectric constant ( $K$ ) is also known as relative permittivity ( $\epsilon_r$ ) and is equal to the permittivity of the material ( $\epsilon$ ) as a ratio relative to the permittivity of free space ( $\epsilon_0$ ). Permittivity is a material property that influences the Coulomb force between two-point charges in the material and define how easily a material can become polarized when is exposed to an electric field on an insulator. The real part of the complex relative permittivity ( $\epsilon_r'$ ) is a measure of how much energy from an external field is stored in a material;  $\epsilon_r' > 1$  for most solids and liquids. The imaginary part of complex relative permittivity ( $\epsilon_r''$ ) is called the loss factor and is a measure of how dissipative a material is to an external field.  $\epsilon_r''$  is always  $> 0$  and is usually much smaller than  $\epsilon_r'$ . The loss factor includes the effects of both dielectric loss and conductivity (Keysight Technologies, 2016).

$$K = \epsilon_r = \frac{\epsilon}{\epsilon_0} = \epsilon_r' - j\epsilon_r'' \quad (4.1)$$

Based on equations 2.1 and 4.1, a dielectric material with high dielectric constant is needed for the production of EAP actuators to increase the equivalent pressure applied to dielectric material. The dielectric test fixture, Agilent 16451B was utilized to quantify the capacitance of different printed TPU samples and in turn calculate the permittivity of the material. This equipment can measure the capacitance of solid materials up to 30 MHz and utilizes a three-terminal method

(ASTM-D150). This method consists of create a capacitor placing the dielectric material between two electrodes. The permittivity is calculated based on the measured capacitance.

The electrodes were covered with electric insulating guards to guarantee that the measured capacitance between the electrodes was just made out of the electric field flowing through the dielectric elastomer. Capacitance was recorded using an Agilent 4263B LCR Meter at 100 kHz. Electrode type A was chosen and utilized, since this sort of electrode is utilized to test materials without a thin film electrode. The tested sample were printed discs with 54 mm of outer diameter and the thickness was varied from 1 to 5 mm. Five samples per thickness value were produced and tested.

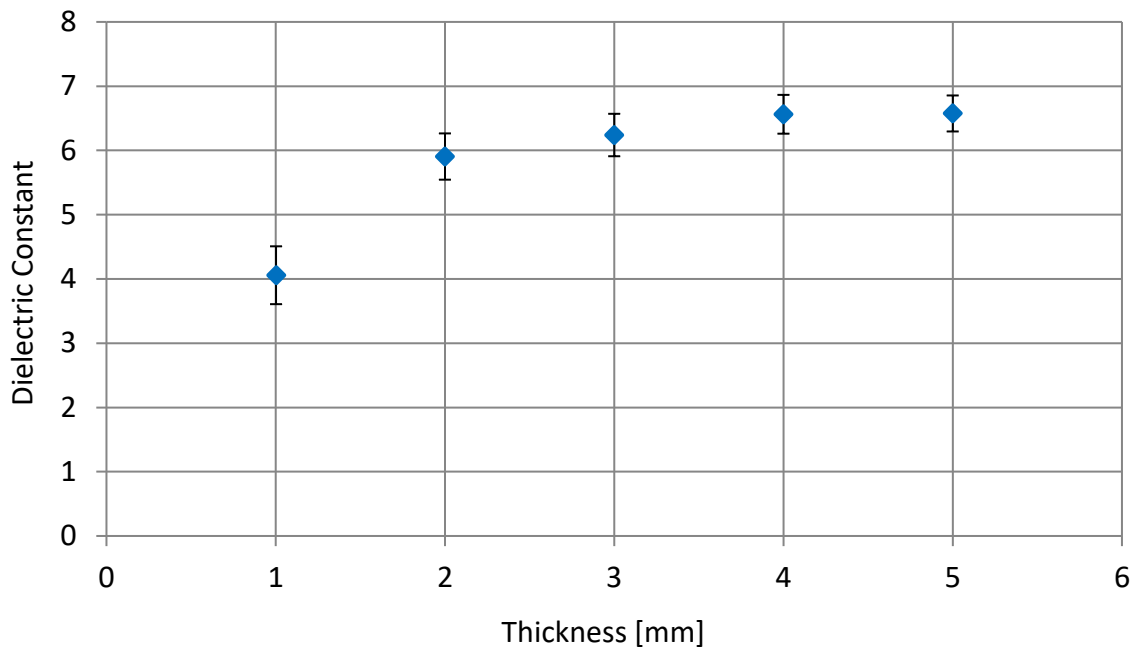


Figure 10. Dielectric constant of printed TPU.

The measured dielectric constant for each batch of samples were averaged. Figure 10 shows that the batch of samples with 1 mm of thickness have a significant deviation from the rest of the batches. This occurs because these samples are very thin and the percentage of overall air in the specimen volume is significant compared to the infill material. In addition, the small distance between the electrodes could affect the measurement and acquire some noise during the test. Based on the previous analysis, results from the batch of samples with 1 mm of thickness were ignored

to determine the value of the dielectric constant. The samples with thickness between 2 and 5 mm showed a stable trend in the dielectric constant trend between 6 and 7. Based on the results, it is possible to conclude that printed TPU have a dielectric constant of  $6.32 \pm 0.30$ .

#### 4.1.2 Applied Pre-strain

The actuation of DEAP structures can be improved if the dielectric material is pre-strained. This induced deformation enhances the expansion of the dielectric membrane to increase the actuation of the structure. The printed samples were pre-strained using an Omnidirectional Iris stretcher machine. This machine deforms the membrane uniformly in the radial direction until failure. In this case failure is characterized by the break of the membrane. The printed specimens had a circular shape with an inner diameter of 100 mm and a thickness of 0.2 mm. An external ring support was added to the membrane design, having a width of 15 mm of width and a thickness of 0.8 mm, to prevent stress concentration and premature breaking at the fastening points. A total of ten samples were produced and tested.

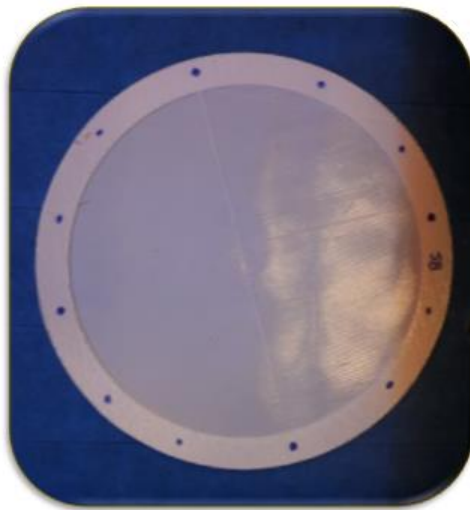


Figure 11. 3D Printed TPU membrane.

The samples were clamped to the machine in 12 different points, one point for each arm of the machine. The samples were stretched uniformly in planar directions. Based on the experimental test, it is possible to conclude that printed TPU membranes are capable of elongate  $560 \pm 10\%$  in the planar direction before failure, which refers to the area strain.

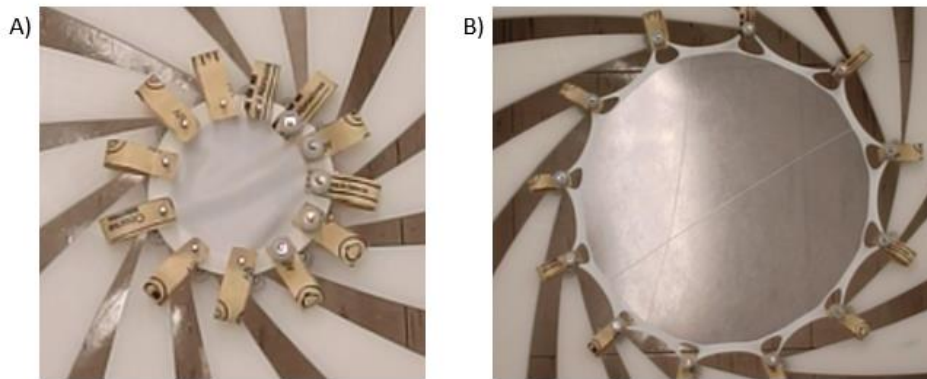


Figure 12. Applied pre-strain test. a). Before stretch b). After stretch (elongation of 560%).

### 4.1.3 Tensile properties

Some of the most important parameters that define the mechanical properties of a 3D printed part are the printing path angle and the quantity of layers. These two settings are defined by the G-code generated in the slicer software. The printing path angle defines the orientation of the infill material, and the quantity of layers affects the structural integrity of the printed part by the adhesion points generated between each layer. Tensile tests were done based on the standard ASTM D638 – 14 “Standard Test Methods for tensile Properties” to characterize the influence of those parameters in the mechanical properties of the material.

The specimens were type IV, based on the ASTM D638 - 14 norm, generally used when direct comparison is required between materials of different rigidity. Three different batches of samples were made varying printing path angle ( $0^\circ$ ,  $45^\circ$ ,  $90^\circ$ ) and the number of layers, from one layer (thickness of  $0.20 \pm 0.02$  mm) to five layers (thickness of  $1.00 \pm 0.02$  mm). Eight specimens were printed for each combination of printing path angle and number of layers.

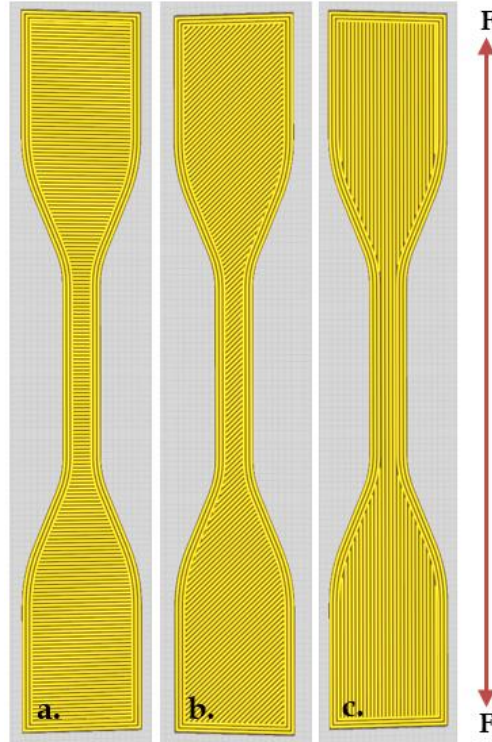


Figure 13. Printing path angles: a) 90°; b) 45°; c) 0°.

A Mechanical Testing System (MTS Criterion - Model C45.605), universal loading machine was utilized to carry out the tensile testing, utilizing a load cell rated for 1 kN loading. The MTS wedge grips were displaced at a rate of 50 mm/min with data collected at 100 Hz.

Table 1. Tensile test data for one-layer samples

| Specimens - One Layer (Thickness: 0.2 mm) |                   |                    |                        |                              |                            |
|---|-------------------|--------------------|------------------------|------------------------------|----------------------------|
| Angle                                     | Number of Samples | Peak Load (SD) [N] | Peak Stress (SD) [MPa] | Strain at Break (SD) [mm/mm] | Young's Modulus (SD) [MPa] |
| 90°                                       | 8                 | 44.38 (2.38)       | 9.48 (0.65)            | 5.11 (0.42)                  | 6.21 (0.61)                |
| 45°                                       | 8                 | 82.47 (2.25)       | 14.94 (0.63)           | 8.39 (0.49)                  | 3.56 (0.58)                |
| 0°  | 8                 | 135.12 (2.66)      | 26.56 (0.55)           | 9.31 (0.45)                  | 3.04 (0.60)                |

Table 2. Tensile test data for two-layer samples

| Specimens - Two Layers (Thickness: 0.4 mm) |                   |                    |                        |                              |                            |
|--|-------------------|--------------------|------------------------|------------------------------|----------------------------|
| Angle                                      | Number of Samples | Peak Load (SD) [N] | Peak Stress (SD) [MPa] | Strain at Break (SD) [mm/mm] | Young's Modulus (SD) [MPa] |
| 90°  | 8                 | 53.28 (2.51)       | 11.22 (0.61)           | 4.91 (0.43)                  | 6.78 (0.63)                |
| 45°  | 8                 | 107.93 (2.35)      | 21.42 (0.57)           | 8.01 (0.47)                  | 3.87 (0.60)                |
| 0°   | 8                 | 143.03 (2.29)      | 28.16 (0.60)           | 8.64 (0.46)                  | 3.29 (0.62)                |

Table 3. Tensile test data for three-layer samples

| Specimens - Three Layers (Thickness: 0.6 mm) |                   |                    |                        |                              |                            |
|--|-------------------|--------------------|------------------------|------------------------------|----------------------------|
| Angle  | Number of Samples | Peak Load (SD) [N] | Peak Stress (SD) [MPa] | Strain at Break (SD) [mm/mm] | Young's Modulus (SD) [MPa] |
| 90°  | 8                 | 69.25 (2.24)       | 13.85 (0.62)           | 4.62 (0.47)                  | 7.22 (0.58)                |
| 45°  | 8                 | 127.64 (2.28)      | 25.94 (0.63)           | 7.38 (0.42)                  | 4.13 (0.60)                |
| 0°   | 8                 | 155.55 (2.41)      | 30.91 (0.67)           | 8.29 (0.40)                  | 3.51 (0.55)                |

Table 4. Tensile test data for four-layer samples

| Specimens - Four Layers (Thickness: 0.8 mm) |                   |                    |                        |                              |                            |
|---|-------------------|--------------------|------------------------|------------------------------|----------------------------|
| Angle                                       | Number of Samples | Peak Load (SD) [N] | Peak Stress (SD) [MPa] | Strain at Break (SD) [mm/mm] | Young's Modulus (SD) [MPa] |
| 90°   | 8                 | 76.94 (2.33)       | 15.14 (0.61)           | 4.38 (0.44)                  | 7.85 (0.59)                |
| 45°   | 8                 | 138.66 (2.53)      | 27.68 (0.55)           | 6.59 (0.40)                  | 4.28 (0.62)                |
| 0°  | 8                 | 170.21 (2.44)      | 33.44 (0.62)           | 7.14 (0.42)                  | 3.64 (0.66)                |

Table 5. Tensile test data for five-layer samples

| Specimens - Five Layers (Thickness: 1 mm) |                   |                    |                        |                              |                            |
|---|-------------------|--------------------|------------------------|------------------------------|----------------------------|
| Angle                                     | Number of Samples | Peak Load (SD) [N] | Peak Stress (SD) [MPa] | Strain at Break (SD) [mm/mm] | Young's Modulus (SD) [MPa] |
| 90°                                       | 8                 | 96.47 (2.40)       | 18.69 (0.67)           | 4.25 (0.41)                  | 8.14 (0.54)                |
| 45°                                       | 8                 | 159.11 (2.11)      | 31.57 (0.56)           | 6.18 (0.46)                  | 4.46 (0.59)                |
| 0°  | 8                 | 178.24 (2.38)      | 35.32 (0.61)           | 6.60 (0.41)                  | 3.72 (0.60)                |

The studied manufacturing parameters affects the mechanical response of the printed samples. An angle of 0° mean that the orientation of the infill material is parallel to the load direction. These samples have more resistivity to tension loads getting the highest load peaks and deformation when contrasted with the samples with perpendicular infill orientation. The specimens with one-layer present the lowest stress ang highest strain, being the samples less resistant. In this case, the quantity of material is proportional to the stiffness and resistance of the printed sample.

Figure 14 shows the average value obtained for the Young's modulus of each batch of samples. These results showed that the batches of samples printed with 0° and 45° path angle have similar behavior increasing the Young's modulus in approximately 1 MPa per mm of thickness. The batch of samples printed with 90° path angle have the highest values of the measured parameters increasing the Young's modulus in approximately 2 MPa per mm of thickness. In this study a perfect polymerization is assumed, which implies that the infill material is completely joined. This assumption affects the results because possibly some of the manufactured samples did not have a perfect polymerization, which may change its tensile properties. However, the manufacturing process was the same for all the samples, using the same parameters.

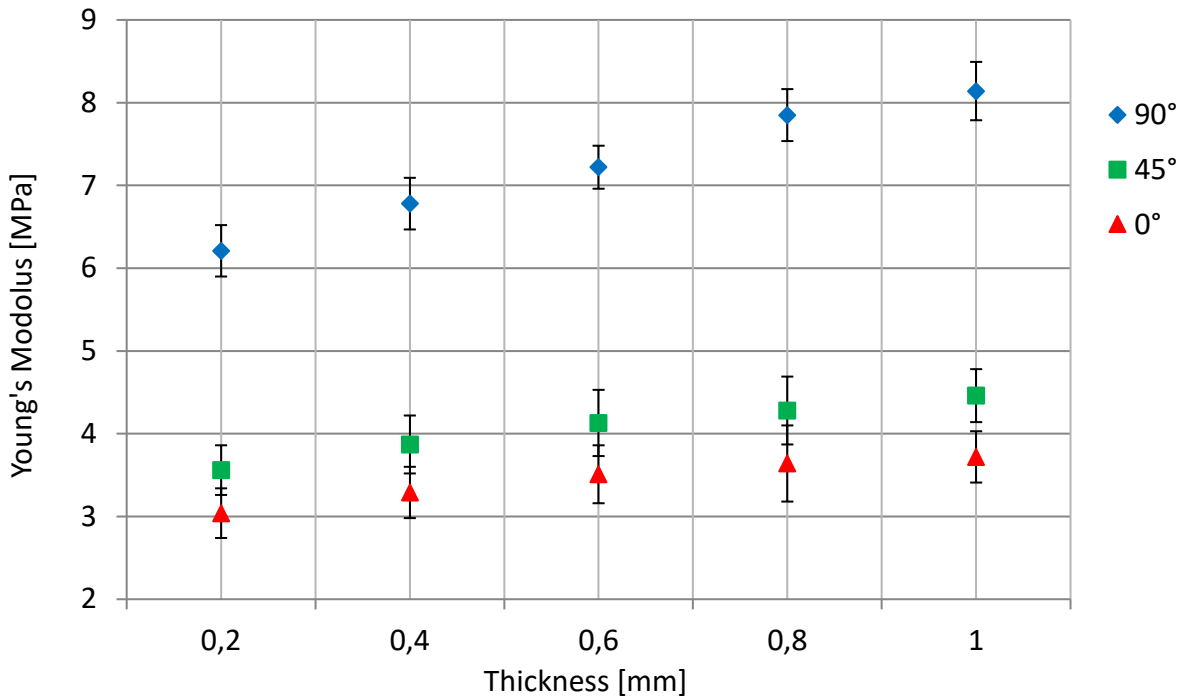


Figure 14. Young's modulus of printed TPU.

#### 4.1.4 Pre-strain treatment

Elastomeric materials are used as dielectric films because this kind of materials have weak intermolecular forces and high viscoelasticity, which makes the material elastic and flexible (Wissler & Mazza, 2008). The elastic recovery of this kind of material is one the most significant attributes, being capable of experience large deformations and return to its original shape without significant structural changes. If an elastomeric material is pre-strained it can achieve a state where large deformation can be produced with small changes of stress.

Some electro active materials require to be pre-strained to increase the actuation of the active structure. The pre-strain treatment aligns the polymer chains of the material in the expanding directions and reduce its thickness. In addition, this process reorients the defects that could cause premature failure of the polymer, improving the dielectric breakdown of the material. However, the pre-strain treatment influences the mechanical properties of the material decreasing the elastic energy density because of creep effect and cyclic stress concentration.

The percentage of applied pre-strain in the dielectric polymer membrane was varied to determine the best condition to produce the largest deformation of the electroactive structure. The

specimens were printed utilizing concentric circular printing path producing one layer with a thickness of 0.2 mm. Three different pre-strain percentages were tested (63%, 360% and 560%), manufacturing five DEAP actuators for each pre-strain percentage. The electroactive structures were tested utilizing a high voltage supply (TREK 610E). The applied voltage was increased between 0 and 10 kV, with increments of 100 V, until failure. The current was limited to a maximum of 2 mA.

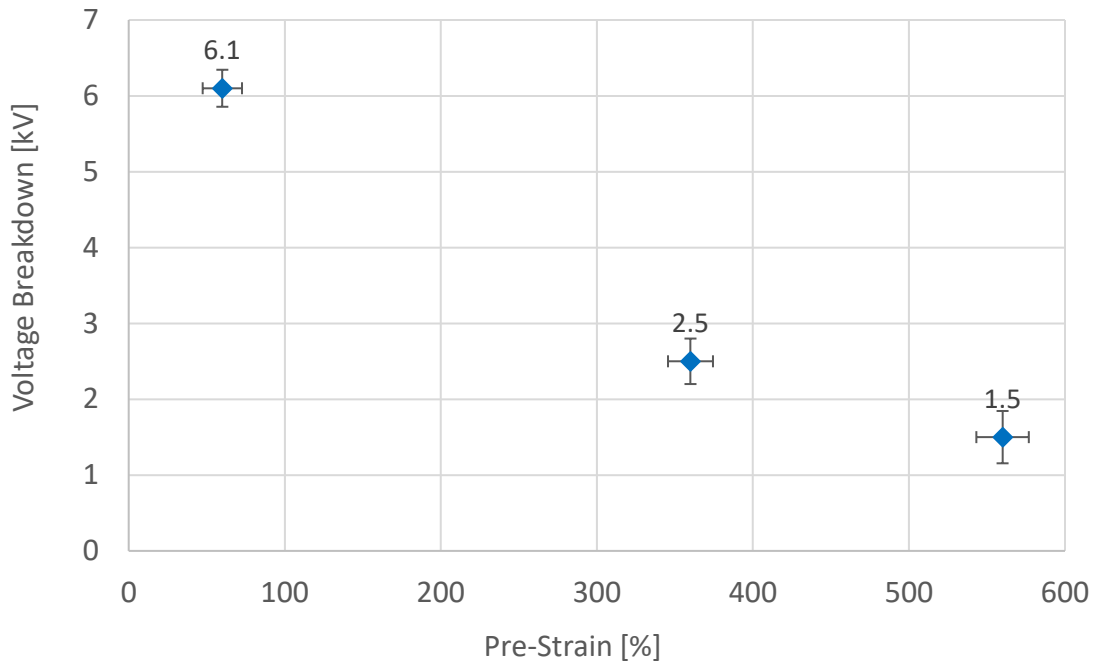


Figure 15. The pre-strain effect on electric field resistance.

Figure 15 shows how the pre-strain influences the voltage breakdown of the dielectric membrane. High pre-strains reduced the resistance of the polymer membrane to electric fields because the thickness of membrane is decreased significantly, to only a few microns. Figure 16 shows the electrically induced deformation of the membrane as a function of its pre-strain.

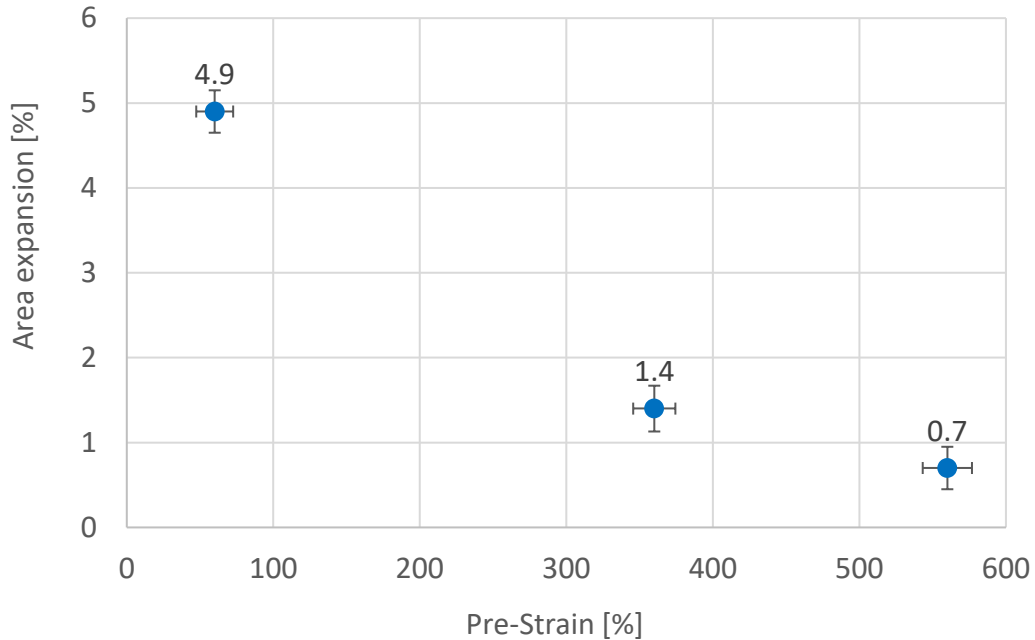


Figure 16. The pre-strain effect on the actuation.

Based on the previous results, it is possible to conclude that 63% of pre-strain applied to the dielectric material enhance its resistance to electric fields, making this value good enough to enhance the actuation of the DEAP actuator. High pre-strain could produce structural defects like fissures, holes, or valleys, creating regions of stress concentration. In addition, some preliminary tests demonstrate that without pre-strain the manufactured DEAP structures were nor capable of producing actuation.

#### 4.1.5 Surface metrology

Low surface quality is one of the main problems and limitation of FDM technique, particularly whenever contrasted with other manufacturing processes. Stress concentration occur when there are irregularities in the geometry or material of a structure, like holes or grooves. Surface quality could affect the performance of flexible structures creating focus points of stress where the structure is more likely to break. A precise characterization of surface topography and roughness is necessary for these kind of electroactive structures to guarantee that the surface integrity of the printed elastomeric membranes is adequate for exposure to electric fields and mechanical loads.

Two different types of printed membranes were characterized. One of them have concentric circles as printing path, while the other have parallel lines as printing path. The printed samples were manufactured using the same CAD model to ensure equal dimensions between them and were printed using the same settings (nozzle diameter: 0.4 mm, temperature: 205 °C, bed temperature: 60 °C, speed: 10 mm/s). The printing process takes 28 minutes for the samples with concentric circles path, and 35 minutes for the samples with parallel line path. The printing time is different between the samples because the printing path that use concentric circles utilize more constant velocity during the entire process with less changes of direction. Five samples were manufactured and characterized for each type of printing path.

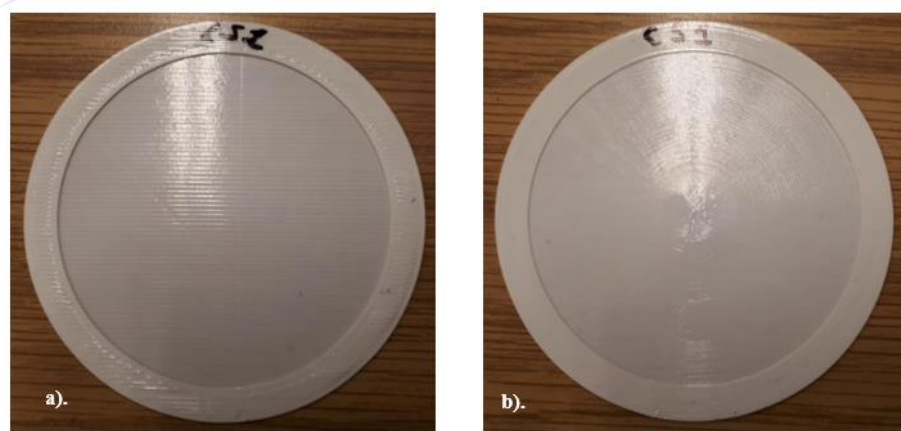


Figure 17. Printed TPU membranes. a). Line path; b). Concentric circles path.

The samples were characterized utilizing an optical microscope “Bruker Contour Elite K 3D”, using an optical magnification of 10X/0.30 and green light interferometry. The scanned area for the samples with parallel line path was 18 mm<sup>2</sup>, while for the samples with concentric circles was 33 mm<sup>2</sup>, for the purpose of visualize the curvature of the path. Figures 18 to 20 show the results for the concentric circles path samples, and Figures 21 to 23 show the results for the line path samples.

### 4.1.5.1 Concentric circles path

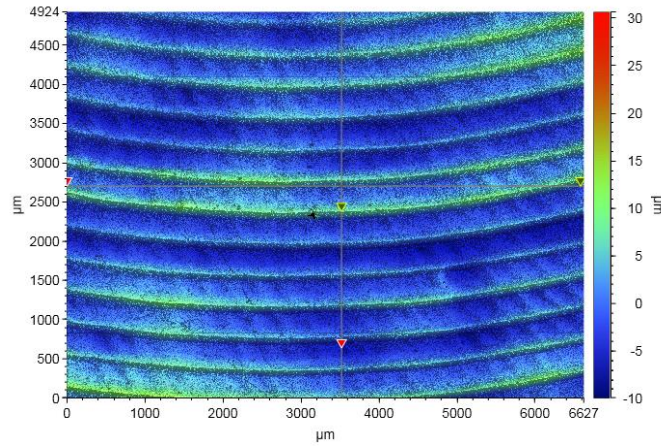


Figure 18. 2D Surface image – Concentric circles path sample.

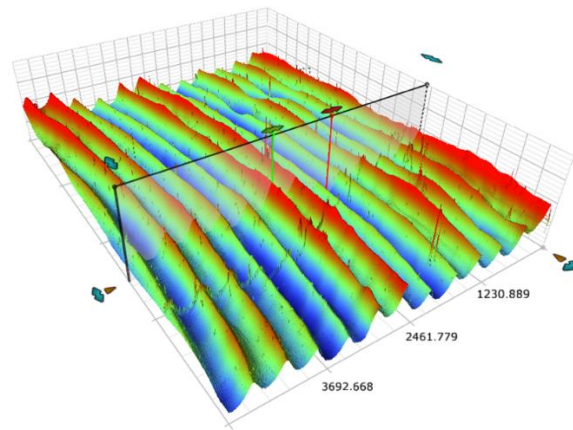


Figure 19. 3D Contour image - Concentric circles path sample.

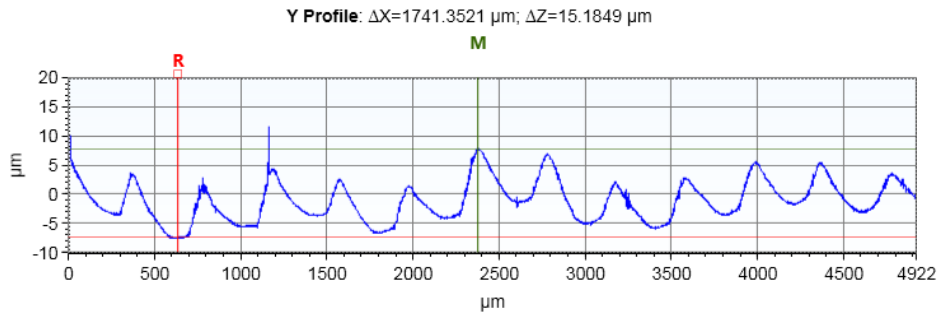


Figure 20. Roughness measurement - Concentric circles path sample.

### 4.1.5.2 Line path

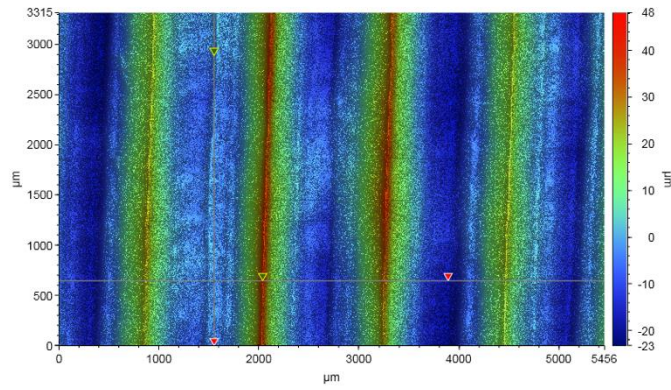


Figure 21. 2D surface image –Line path sample.

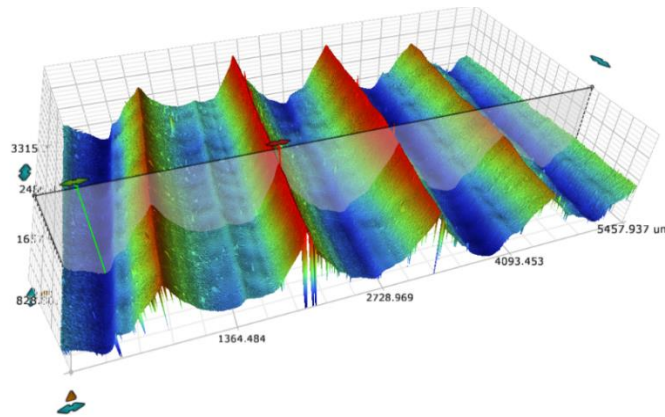


Figure 22. 3D Contour image – Line path sample.

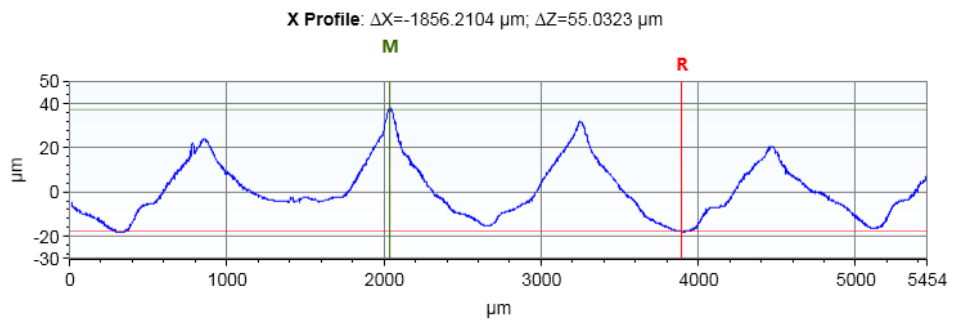


Figure 23. Roughness measurement - line path sample.

Surface metrology results show the surface characteristics of the printed polymer membranes, utilizing different printing paths. The produced membranes have a characteristic roughness that is determined by the printing path. Obtained images showed a consistent surface of the membranes without apertures or fissures that could produce premature failure of the DEAP structures. Figure 20 and 23 depict the roughness of the samples having a wavelike shape composed of approximately equidistant peaks and valleys. Despite that, the height of the peaks and valleys is not constant because the printing bed is not a completely flat surface and may have some angle of inclination. The membranes with line path have an average  $\Delta Z$  (distance between the lowest valley and the highest peak) of 56.41  $\mu\text{m}$ , while the samples with concentric circles path have an average  $\Delta Z$  of 15.63  $\mu\text{m}$ , having a better surface quality.

During the printing process of line path and circles path, the motors that control the X and Y axes are moving all the time. In the line path samples, the infill orientation was not aligned with one of the axes, this makes that the infill material have an angle with respect to the coordinate system of the printer. It is evident how the printing path that utilize lines change the travel direction several times, which produces changes in acceleration and velocity of the printing head. The changes of velocity and acceleration of the printing head increase the profile roughness of the printed samples. When the concentric circles path is utilized the printing head moves with more constant velocity and only has drastic changes in the travel direction when the printing head moves closer to the center of the layer, producing a smooth surface with small profile roughness.

#### **4.1.6 Actuation**

The dielectric membranes were manufactured using the same printing settings and dimensions as in the surface metrology test. Five DEAP structures were manufactured and characterized for each type of printing path. The experimental procedure was the same as in the pre-strain treatment. The expansion of the electrodes was measured and analyzed based on the induced electric field, finding the maximum percentage of area expansion during the actuation test. The samples with printing line path were measured in two different directions: parallel and perpendicular; based on the deformation direction and infill orientation.

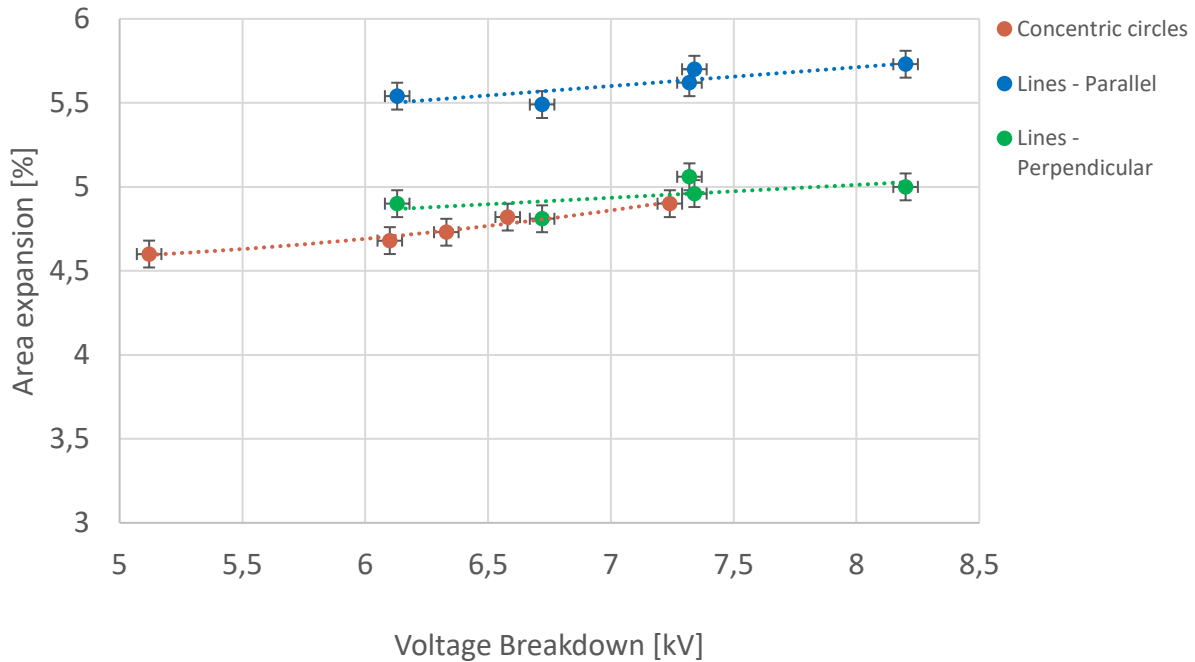


Figure 24. Actuation of DEAP structures.

Figure 24 shows that the printing path influences the actuation of the DEAP structures. The two different types of samples have a relative constant behavior in which the expanded area changed less than 0.5% the samples of each batch. These results demonstrate reproducibility and consistency of the used manufacturing process. The samples with printing line paths have an average expansion area of  $5.71 \pm 0.10$  % in the parallel direction, and  $4.91 \pm 0.10$  % in the perpendicular direction. On the other hand, the samples with concentric circles path have an average expansion area of  $4.73 \pm 0.12$  %. Produced DEAP actuators showed an actuation and electric resistivity higher than other electroactive structures like shape memory alloys and ferroelectric polymers. The manufactured structures presented a voltage breakdown between 5.1 and 8.2 kV, and the actuation performed of all the samples was visible to the human eye. Those results are similar to the resistant of the most used dielectric material “VHB 4910”. Commonly, DEAP structures exhibit a deformation in the micro scale.

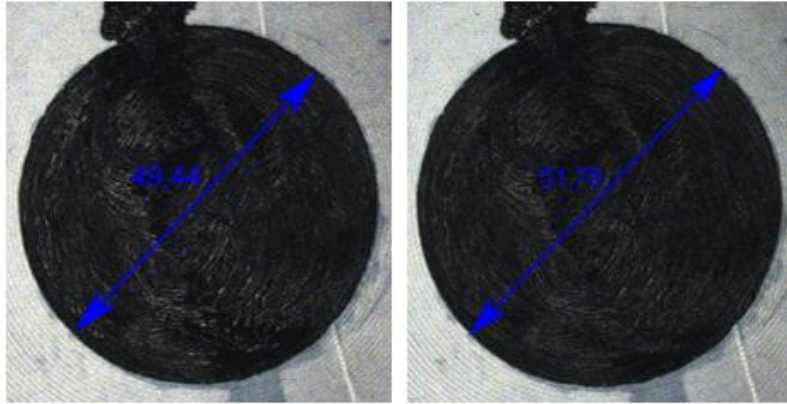


Figure 25. Actuation of DEAP structure at 4.67 kV - Concentric circles path.

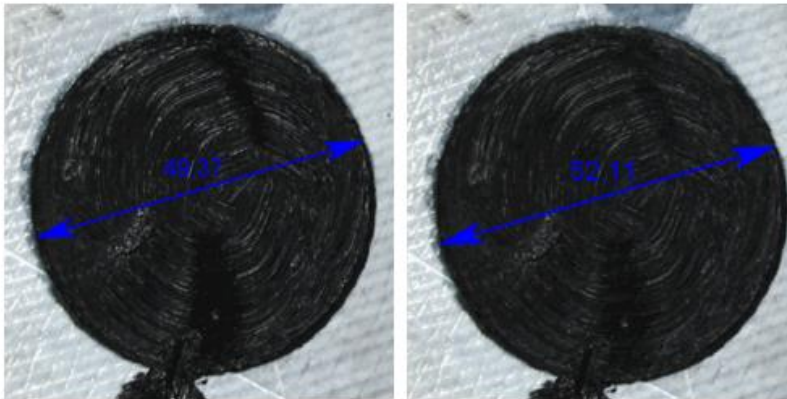


Figure 26. Actuation of DEAP structure at 5.73 kV (Parallel direction) - Line path.

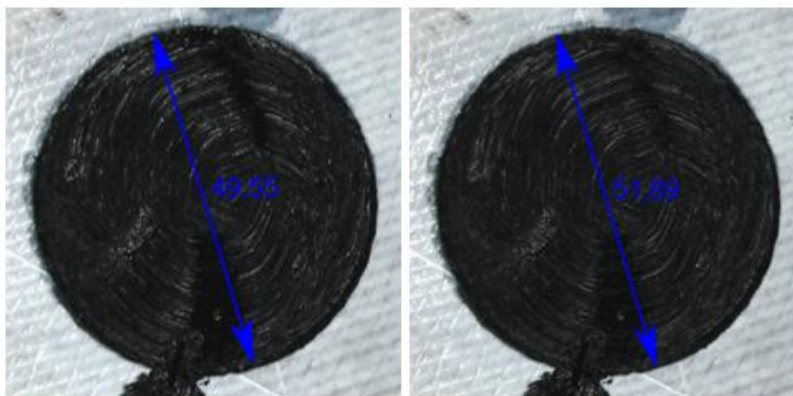


Figure 27. Actuation of DEAP structure at 5.02 kV (Perpendicular direction) - Line path.

## 4.2 Soft actuators

Soft pneumatic actuators were manufactured using the “LulzBot Taz 6” 3D printer. Regular printing heads are not capable of printing flexible materials. For that reason, a specialized printing head for flexible materials was built providing greater control in the process and improving the quality of the printed actuators. All samples were printed using the same 3D printer machine, material, and printing settings (layer height: 0.15 mm, infill density: 100%, printing temperature: 205 °C, build plate temperature: 60 °C, printing speed: 10 mm/s; no support material).

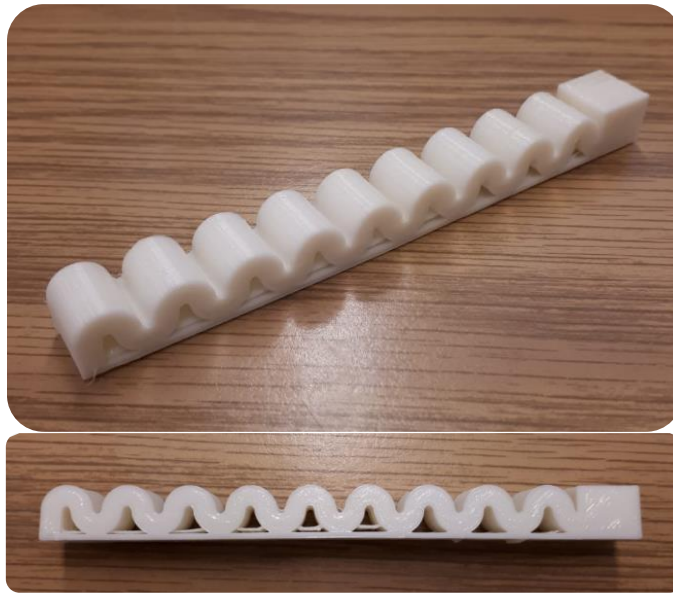


Figure 28. 3D printed bellow pneumatic actuator.

### 4.2.1 Material simulation

Materials that are capable of experiencing large deformation under small loads and then return to their original shape without any significant plastic deformation can be considered to be hyperplastic materials. The stress-strain behavior of a hyperplastic material is nonlinear. A constitutive mathematical model is necessary to represent the real behavior of a hyperplastic material. These hyperplastic models can be used with materials that undergo large deformation, taking into account intrinsic and geometric nonlinearities (Hwang, 2015).

The 3D printing process gives anisotropic properties to the printed actuators due to the different printing orientations of the material during the manufacturing process. Tensile test results demonstrated that printing orientation (related to the printing path) and the number of layers are

critical parameters when printed parts are exposed to external loads (Galley, 2018). Uniaxial tensile results shown in the previous section were used to characterize the material, being able to define the values of the properties that model the corresponding behavior of the material. This stress strain data was fit with known hyperelastic models to predict deformation in a constructed Mooney-Rivlin model.

The two-parameter incompressible Mooney-Rivlin material model describes the local behavior of rubber-like materials. The model assumes that the local strain energy density in an incompressible solid is a simple function of local strain invariants. In a standard tensile test, a rotationally symmetric test specimen is loaded in such a way that it extends in one direction and contracts symmetrically in the other two. For this case of uniaxial extension, the relationship between applied force,  $F$ , and resulting extension,  $\Delta L$ , of a true Mooney-Rivlin material is defined by:

$$\frac{F}{A_0} = 2 \left( C_{10} + C_{01} \frac{L_0}{L_0 + \Delta L} \right) \left( \frac{L_0 + \Delta L}{L_0} - \left( \frac{L_0}{L_0 + \Delta L} \right)^2 \right) \quad (4.2)$$

Where  $A_0$  is the original cross-section area of the test specimen and  $L_0$  is its reference length. The constants  $C_{10}$  and  $C_{01}$  are material parameters which must be determined by fitting equation 4.2 to the experimental data from the tensile test. In this case, the corresponding measured values of engineering stress,  $P_i$ , representing force per unit of reference area:

$$P = \frac{F}{A_0} \quad (4.3)$$

And stretch,  $\lambda_i$ , representing relative elongation:

$$\lambda = \frac{L_0 + \Delta L}{L_0} \quad (4.4)$$

The expected relationship between these variables for a Mooney-Rivlin material is:

$$P(\lambda) = 2 \left( C_{10} + \frac{C_{01}}{\lambda} \right) \left( \lambda - \frac{1}{\lambda^2} \right) \quad (4.5)$$

Given  $N$  pairs of measurements  $(\lambda_i, P_i), i = 1..N$ , the values of  $C_{10}$  and  $C_{01}$  which best fit the measured data are considered to be those which minimize the total squared error:

$$e = \sum_{i=1}^N (P(\lambda_i) - P_i)^2 \quad (4.6)$$

During actuation, the majority of the strain occurred in the longitudinal direction caused by the unfolding of the bellows of the actuator. For that reason, only longitudinal orientation data (printing angle:  $90^\circ$ ) was considered to constitute the model fitting. The average data in the longitudinal orientation was fit using a Mooney Rivlin hyperplastic model. The strain energy equation for this model is presented in equation 4.7,

$$W = C_{10}(I_1 - 1) + C_{01}(I_2 - 1) \quad (4.7)$$

where  $I_1, I_2$  are the first and second deviatoric strain invariants, and  $C_{10}, C_{01}$  are material-specific parameters (Kumar et al., 2016). The least square curve fit was used to determine the parameter for the strain energy function using the simulation software “ANSYS 2019”. Figure 29 shows the curve fitting for the Mooney Rivlin 2 parameter model based on the experimental data. The results showed that the material constants  $C_{10}, C_{01}$  are 0.64 and 0.49 MPa respectively.

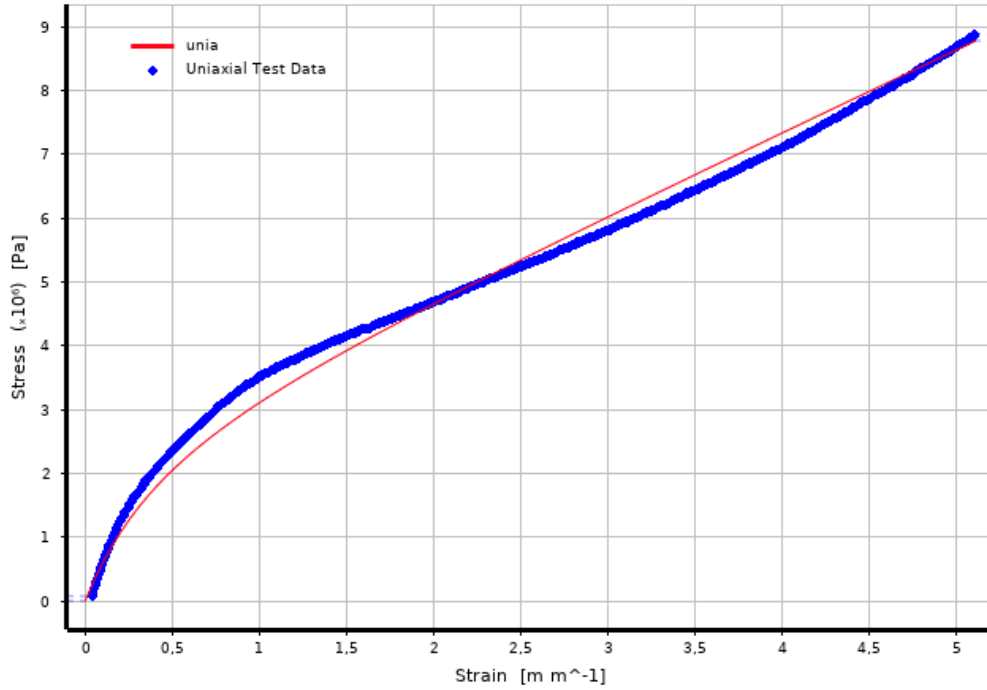


Figure 29. Uniaxial data fitting Mooney Rivlin – 2 parameter hyperplastic model.

#### 4.2.2 Computational simulation

A 3D finite element model was built for the pneumatic bellow actuator previously described. The model was analyzed using COMSOL Multiphysics 5.4 software, to model the behavior of the actuator under different input pressures. In this case, the solid mechanics interface from the structural mechanics module was used for a general structural analysis of a 3D model. The solid mechanics interface is based on solving the equations of motion together with a constitutive model for a solid material. Results such as displacement, stress, and strain are computed.

The physics interface used the global spatial components of the displacement field  $u$  as dependent variables. In a 3D model, the names for the components are  $(u, v, w)$ . The formulation used for structural analysis in COMSOL Multiphysics for both small and finite deformation is a total lagrangian formulation. This means that the computed stress and deformation state is always referred to the material configuration rather than to current position in space. Consider a physical particle, initially located at the coordinate  $X$ . During deformation, this particle follows a path:

$$x = x(X, t) \quad (4.8)$$

Here,  $x$  is the spatial coordinate and  $X$  is the material coordinate. For simplicity, assume that undeformed and deformed positions are measured in the same coordinate system. The displacement  $u$  it is then possible to write

$$x = X + u(X, t) \quad (4.9)$$

The gradient of the displacement, which occurs frequently in the following theory, is always computed with respect to material coordinates. In a 3D case will be:

$$\nabla u = \begin{bmatrix} \frac{\partial u}{\partial X} & \frac{\partial u}{\partial Y} & \frac{\partial u}{\partial Z} \\ \frac{\partial v}{\partial X} & \frac{\partial v}{\partial Y} & \frac{\partial v}{\partial Z} \\ \frac{\partial w}{\partial X} & \frac{\partial w}{\partial Y} & \frac{\partial w}{\partial Z} \end{bmatrix} \quad (4.10)$$

The deformation gradient tensor  $F$  shows how an infinitesimal line element,  $dX$ . Is mapped to the corresponding deformed line element  $dx$  by:

$$dx = \frac{dx}{dX} dX = F dX \quad (4.11)$$

The deformation gradient  $D$  contains the complete information about the local straining and rotation of the material. In terms of the displacement gradient,  $F$  can be written as:

$$F = \frac{\partial x}{\partial X} = \nabla u + I \quad (4.12)$$

The deformation of the material will in general cause changes in the material density. The ratio between current and initial volume (or mass density) is given by:

$$\frac{dV}{dV_0} = \det(F) = J \quad (4.13)$$

The determinant of the deformation gradient tensor is always positive, since negative mass density is unphysical. The previous relation implies that for  $J < 1$  there is a compression, and for  $J > 1$  there is expansion, like in this study case.

The right Cauchy-Green deformation tensor give us the square of local change in distances due to deformation. It is a symmetric and positive definite tensor, which accounts for the strain but not for the rotation. The right Cauchy-Green deformation tensor  $C$  is defined by:

$$C = F^T F \quad (4.14)$$

The Green-Lagrange strain tensor is a symmetric tensor used to evaluate how much a given displacement differs locally from a rigid body displacement, is a measure of how much  $C$  differs from  $I$ . This strain tensor can be defined by:

$$\varepsilon = \frac{1}{2}(C - I) = \frac{1}{2}(F^T F - I) \quad (4.15)$$

Three different stress measures are used in COMSOL Multiphysics:

- Cauchy stress  $\sigma$  defined as force/deformed area in fixed spatial directions not following the body. This is a symmetric tensor.
- First Piola-Kirchhoff stress  $P$ . The forces in the spatial directions are related to the area in the original (material) frame. This is an unsymmetric two-point tensor.
- Second Piola-Kirchhoff stress  $S$ . Both force and area are represented in the material configuration. For small strains the values are the same as Cauchy stress tensor but the directions are rotating with the body. This is a symmetric tensor.

The stresses related to each other are defined be:

$$S = F^{-1}P \quad (4.16)$$

$$\sigma = J^{-1}PF^T = J^{-1}FSF^T \quad (4.17)$$

Using the first Piola-Kirchhoff stress tensor, the equation of motion for the stationary study can be written in the following form:

$$0 = \nabla \cdot (FS)^T + F_V \quad (4.18)$$

Where  $F_V$  is the volume force vector that has components in the actual configuration but given with respect to the undeformed volume. The von Mises equivalent stress is computed from the Cauchy stress, which is based on force per current area.

The material used in the simulation was TPU, defining the material as hyperelastic and modeled by the two-parameter incompressible Mooney Rivlin material model. All components of the actuator were modeled using solid tetrahedral elements. The mesh of the entire structure has 51,379 elements with an average element quality of 0.64, discretizing the structure properly for computational analysis.

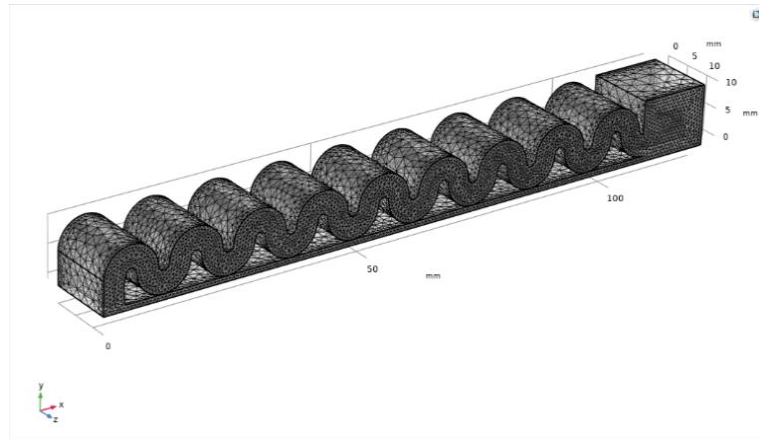


Figure 30. Computational mesh of the bellow actuator.

The pressure was modeled using a load ramping function, solving a sequence of intermediate problems with gradually increasing load values and using the solutions from each previous step as the initial condition for the next step. Based on the design above, the pressure was defined from 0 to 25 psi with increments of 1 psi. Fixed boundary conditions were applied to the proximal end of the actuator where the input for compressed air is located. Air pressure was directly applied to all the surfaces of the internal channel.

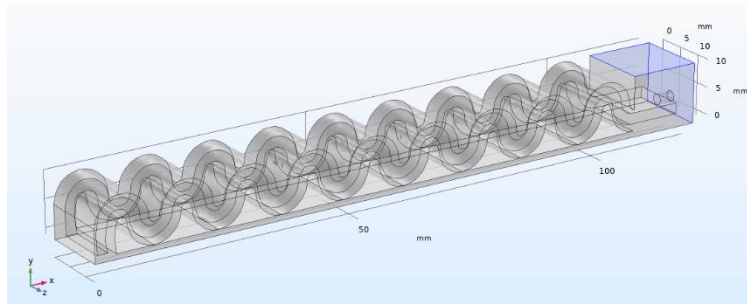


Figure 31. Fixed boundary constraints on the bellow actuator (purple surfaces).

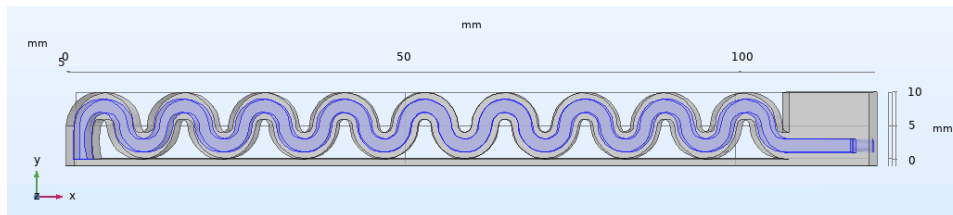


Figure 32. Boundary load on the bellow actuator (purple surfaces).

The model reached convergence after 114 iterations with an error of  $9 \times 10^{-6}$ . The bending behavior of the actuator when it is pressurized to the maximum pressure is illustrated in Figure 33.

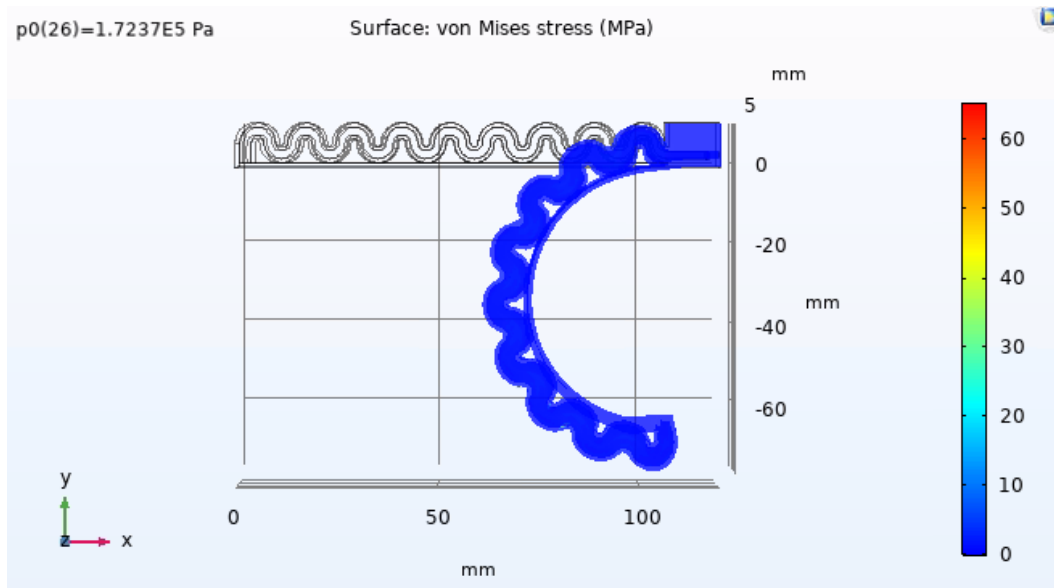


Figure 33. Finite element analysis - bending behavior under a pressure of 25 psi. Von Mises Stress [MPa]

The FEA models show that when air pressure is applied, the wall of the actuator constrains the expansion on the bottom side, and the unconstrained surface on the top of the actuator experiences greater strain from the unfolding effect. The overall effect is therefore a bending of the actuator, where the end of the actuator presents the greater displacement. Based on the results of Figure 29, it is possible to determine that most of the structure is under a low stress condition (<5 MPa) that is, under the yield strength of the material. Therefore, the structure can return to its initial position without any permanent deformation. In addition, the top surface of the actuator presents higher stresses (>5 MPa) as a result of the preferential expansion on these regions. Some areas of increased stress can be identified at the inflection points of the structure on the bottom part of the internal channel.

Figure 34 illustrates the total deformation of the actuator when it is pressurized up to 25 psi. These results are correlated with the bending motion produced by the real actuator, where the furthest area from the fixed boundaries presents the highest displacement (>130 mm). From this region the actuator presents a negative gradient of displacement until it reaches the fixed points.

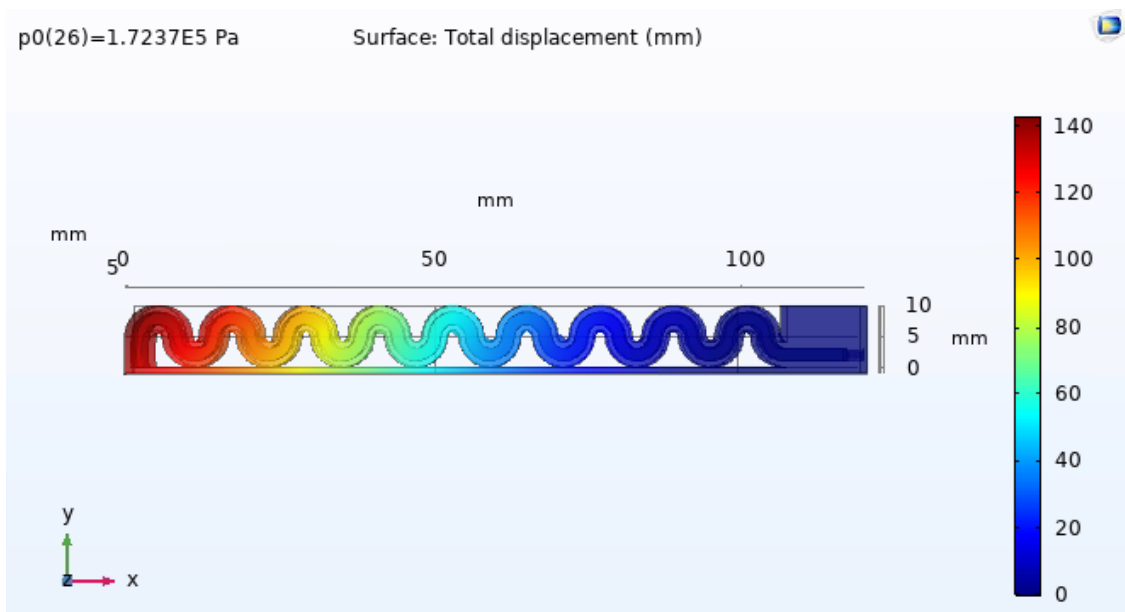


Figure 34. Finite element analysis – Total displacement [mm] under a pressure of 25 psi.

### 4.2.3 Experimental test

The experimental setup was composed of the following elements: compressed air line, manual pressure regulator valve, and pressure transmitter (Wika A-10). All the components were connected in series. The actuator was connected to the pressure transmitter closing the air flow system. The line of compressed air had a pressure of 60 psi that was reduced and controlled by the manual pressure regulator valve. The pressure transmitter measures the real pressure delivered to the actuator. This sensor has a range of 0 to 25 psi and a resolution of 0.01 psi. A National Instruments USB data acquisition system (NI DAQ 6212) was used to measure the current signal provided by the sensor. Finally, the LabVIEW 2019 software was used to control the data acquisition device and managed recording of the data for post processing analysis. The software also monitored the signal in real time to adjust and verify the conditions of the experiment.

The experiment was conducted by pressurizing the internal channel of the structure from 0 to 25 psi in increments of 5 psi. The pressure regulator valve was controlled manually. The actuator was fixed by the air inlet duct using a 3D printed structure. During the entire experimental procedure, the system was completely sealed and, rupture or failure of the actuator was not observed. The entire test was recorded using a camera (Logitec HD Pro Webcam C920) with a resolution of 720p (1280 x 720) and 30 frames per second. The video was analyzed using an open source software, “Tracker 5.1.3”.

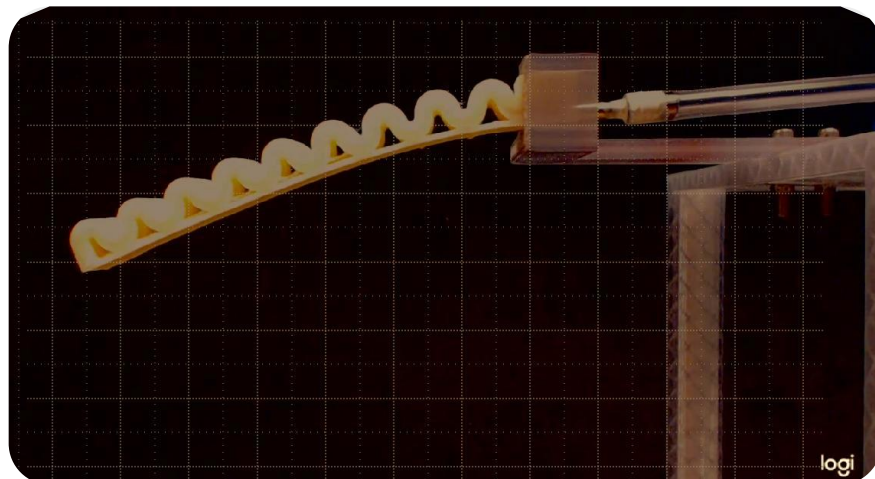


Figure 35. Experimental test setup for the pneumatic bellow actuator.

Computational and experimental results were analyzed using Tracker 5.1.3 software, finding two different parameters: angle of deformation and distance from the origin of a coordinate system to the end of the actuator (located in the wall at the bottom part of the structure). The angle of deformation was measured from the horizontal axis to the end of the actuator. The analysis was made for six different pressures: 0, 5, 10, 15, 20 and 25 psi. Figures 36 to 41 show the data analysis for the experimental and computational results.

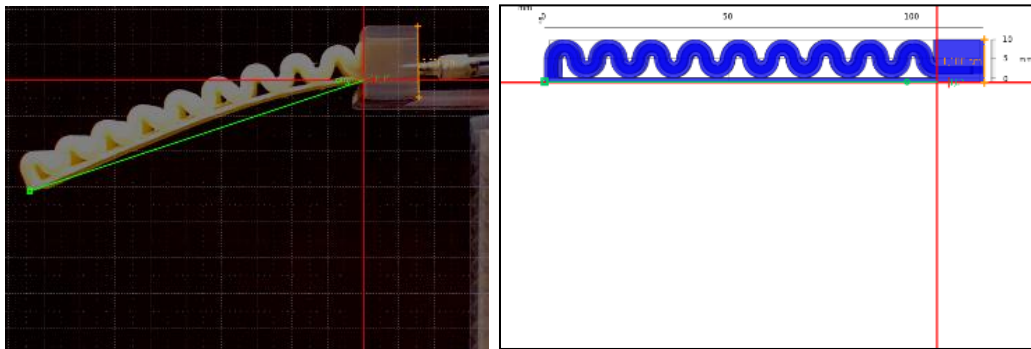


Figure 36. Displacement analysis (0 psi).

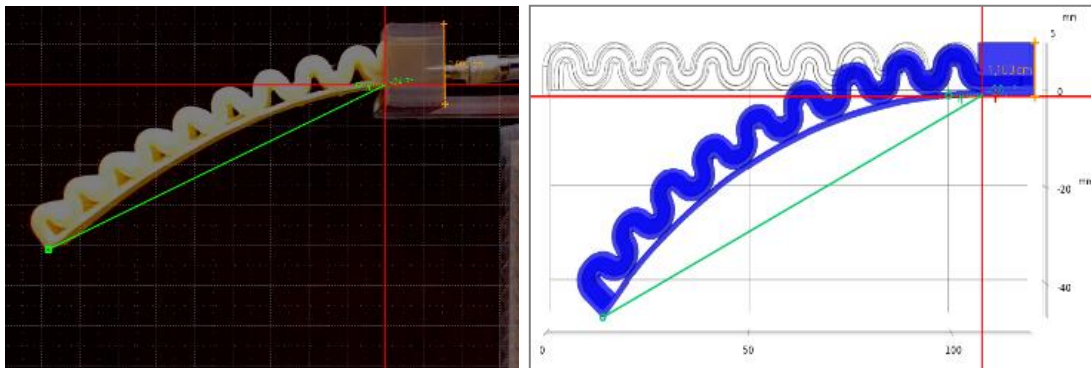


Figure 37. Displacement analysis (5 psi).

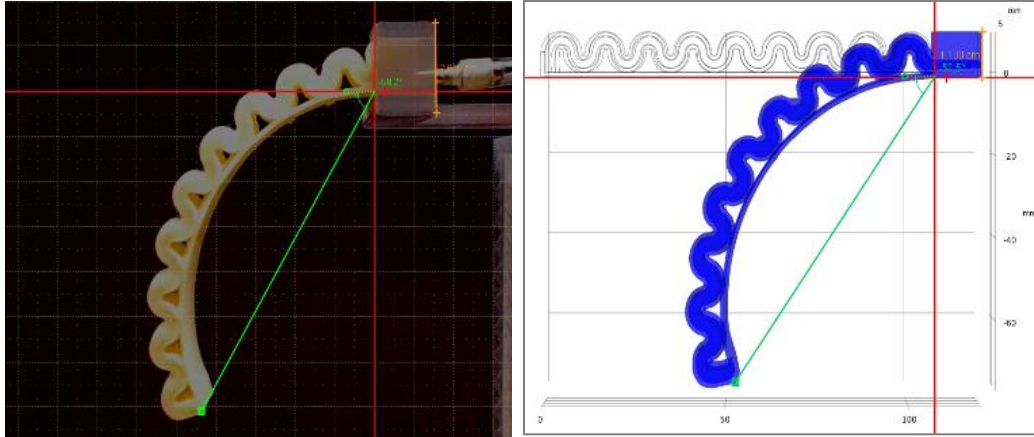


Figure 38. Displacement analysis (10 psi).

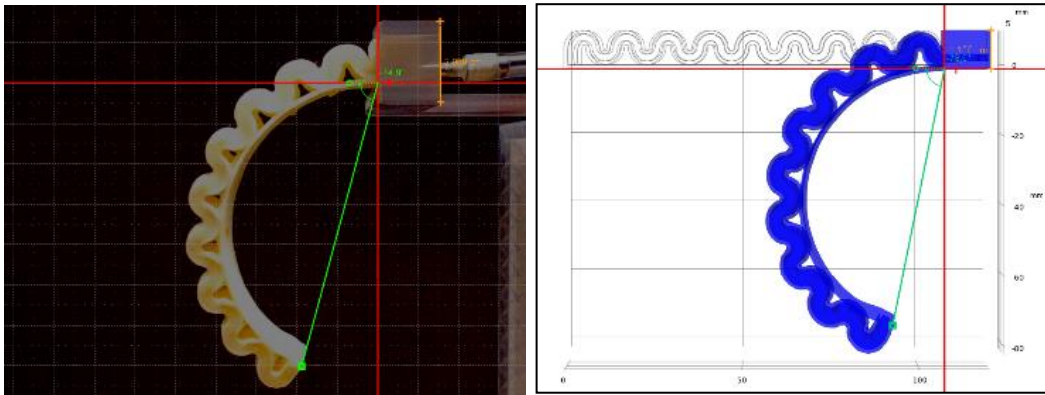


Figure 39. Displacement analysis (15 psi).

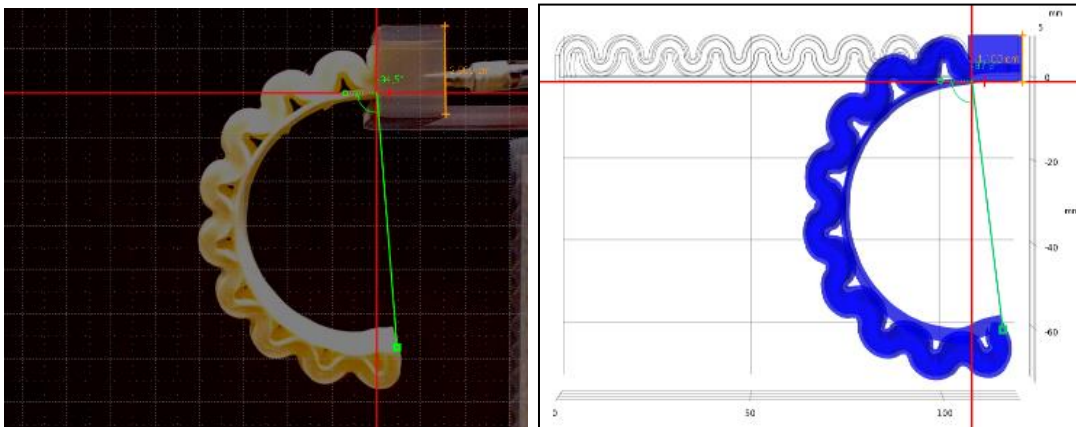


Figure 40. Displacement analysis (20 psi).

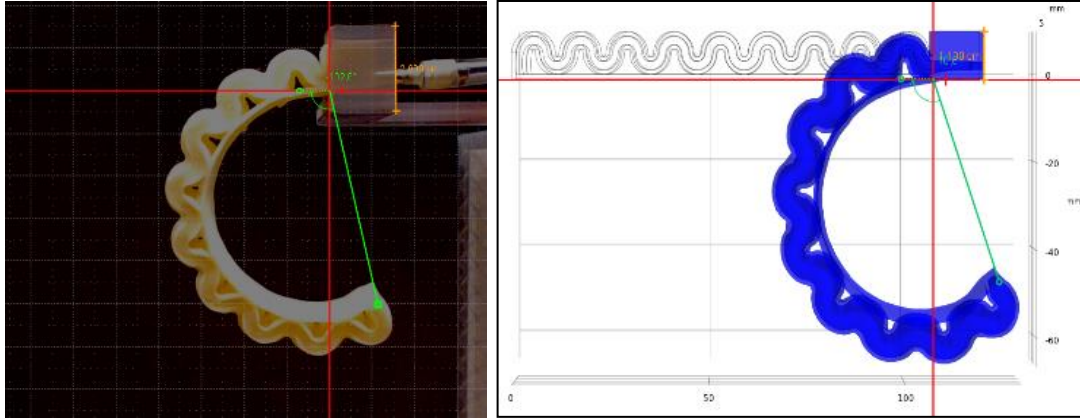


Figure 41. Displacement analysis (25 psi).

The experimental test was performed to five samples of printed soft actuators. Table 6 show the displacement results for computational and experimental results based on the two parameters analyzed.

Table 6. Key data of soft actuators displacement results. (\* absolute values) (The computational simulation values have an error of  $\pm 0.05^\circ$  and  $\pm 0.005$  cm for the angle and length respectively)

| Pressure [psi] | Computational simulation |             | Experimental test    |                     | Error*    |             |
|----------------|--------------------------|-------------|----------------------|---------------------|-----------|-------------|
|                | Angle [°]                | Length [cm] | Angle [°]            | Length [cm]         | Angle [°] | Length [cm] |
| 0              | 0                        | 10.67       | -18.1 ( $\pm 0.4$ )  | 9.90 ( $\pm 0.12$ ) | 18.1      | 0.77        |
| 5              | -26.1                    | 10.29       | -24.7 ( $\pm 0.6$ )  | 9.74 ( $\pm 0.08$ ) | 1.4       | 0.55        |
| 10             | -58.5                    | 9.11        | -55.2 ( $\pm 0.4$ )  | 8.32 ( $\pm 0.10$ ) | 3.3       | 0.79        |
| 15             | -78.6                    | 7.41        | -74.9 ( $\pm 0.3$ )  | 7.25 ( $\pm 0.12$ ) | 3.7       | 0.16        |
| 20             | -97.8                    | 5.91        | -94.5 ( $\pm 0.4$ )  | 5.76 ( $\pm 0.14$ ) | 3.3       | 0.15        |
| 25             | -110.0                   | 5.10        | -102.8 ( $\pm 0.5$ ) | 4.88 ( $\pm 0.16$ ) | 7.2       | 0.22        |

Based on the results presented in Table 6, it is possible to affirm that the computational model describes the real behavior of the manufactured actuator, validating the characterization of the material and the simulation parameters. The results showed good reproducibility based on the low values of the standard deviations. The highest error between the computational simulation and the experimental test was at 0 psi. Under this condition, the computational model had an initial position that was horizontal, because the gravity effects were neglected. The initial position for the experimental test has an initial displacement of the actuator from the origin that is caused by the weight of the structure. However, that initial displacement could be nullified by applying a negative pressure. For pressure conditions from 5 to 20 psi, the error for the angle of deformation

is less than 6%. Under 25 psi the error for the angle of deformation reached a value of 6.5%. For pressure conditions from 0 to 25 psi, the error for the length is less than 5%. After 10 or more repetitions the actuator could experience some hysteresis, characteristic of some elastomeric materials

The computational model shows similar results to those obtained experimentally being able to predict the response of the manufactured soft actuator. However, there are differences between both results due to the manufacturing process of the actuator. The computational model assumes a completely solid actuator, but in reality the actuator could have small gaps between the printed layers.

#### **4.2.4 Applications**

Two different soft gripper actuators were designed using the same concept, shape, and configuration of the previous soft actuator. These designs prove the functionality of the single bellow design and were characterized experimentally and computationally. Both actuators have only one input port for the compressed air that is connected to the entire internal channel. The thickness of each of the three regions that compose the soft actuator are the same as in the single bellow design. The actuator was printed using the same 3D printer, material and setting specified in the single bellow design. All the computational models were made using COMSOL Multiphysics 5.4 software, for the finite element analysis.

##### **4.2.4.1 Open dual bellow actuator**

This soft gripper actuator is composed of two bellow actuators connected in the middle, with an internal channel with an inlet for air supply on the top of the structure.

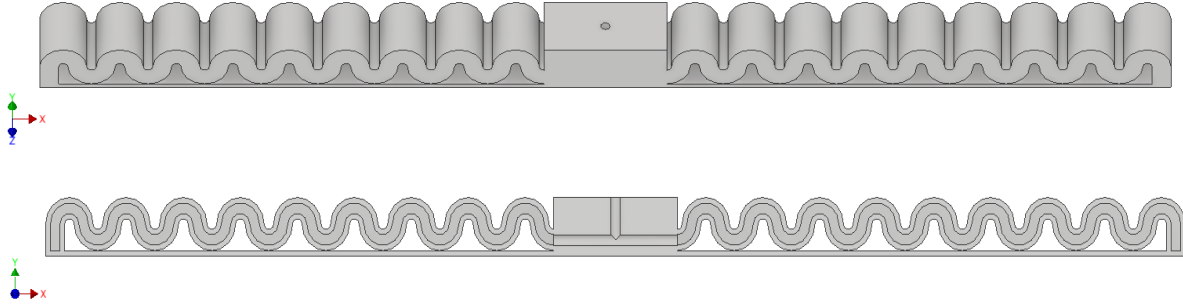


Figure 42. Open dual bellow pneumatic actuator CAD model.

The printing process took 8 hours and 41 minutes to be completed. The printing time is considerably high because this type of material needs to be printed using a very low speed (10 mm/s). The printed actuator has a weight of 25.52 grams and a total length of 240 mm in the x-direction.



Figure 43. 3D printed open dual bellow pneumatic actuator.

It is expected that the actuator produces a bending motion in both of its sides, forming a semicircle when it is pressurized. This motion can work as a gripper, where both of its ends are opened or closed, holding various items. The computational simulation shows the expected motion of the actuator, achieving a closed semi-circular structure under 24 psi. The mesh of the entire structure has 97,833 elements with an average element quality of 0.64, discretizing the structure properly for computational analysis. The model reached convergence after 128 iterations with an error of  $1 \times 10^{-5}$  demonstrating accurate results.

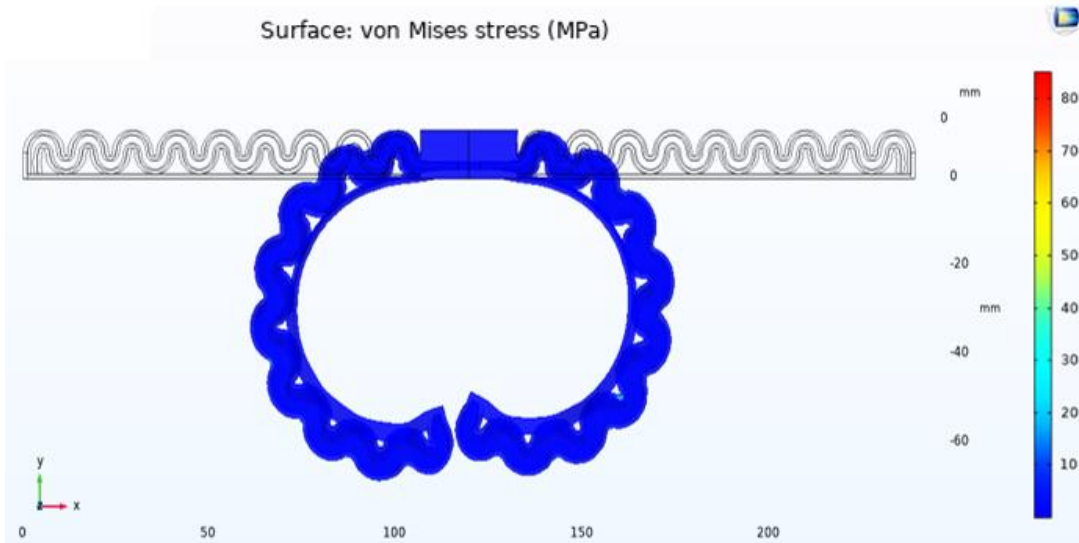


Figure 44. FEA - Bending-close behavior under a pressure of 24 psi. Von Mises Stress [MPa]

The experimental test shows that the 3D printed actuator achieves a closed circular shape under 24 psi. An experimental test was performed to prove the grip functionality of the actuator.

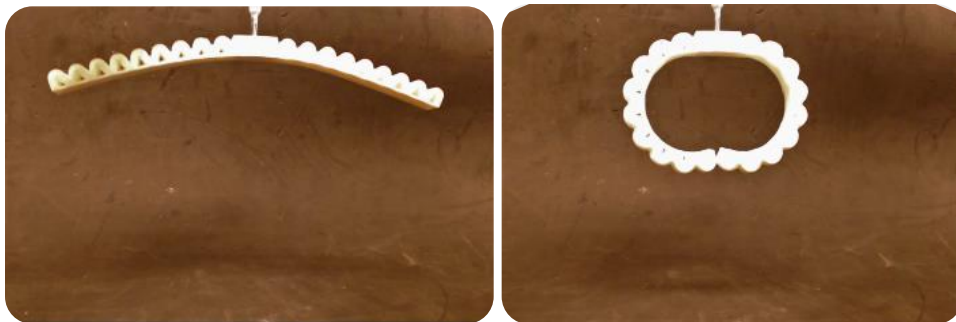


Figure 45. Bending-close behavior under a pressure of 24 psi.

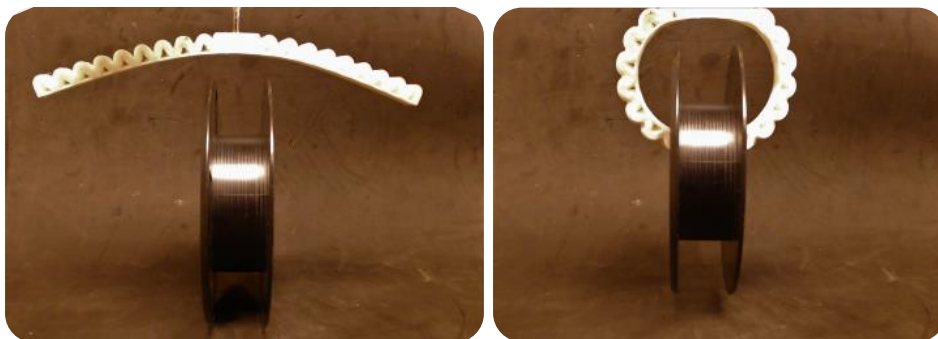


Figure 46. Grip functionality under a pressure of 24 psi.

This type of soft pneumatic actuator was able to lift an empty spool of filament with a weight of 114 g. The actuator presented good grip and mobility to transport and lift the object, under low pressures.

#### 4.2.4.2 Closed dual bellow actuator

This soft gripper actuator is composed of two bellow actuators in a closed loop configuration. The actuators are placed in front of each other being symmetric and connected at both of the extremes having just one closed internal channel. The actuator has one input port for compressed air located in the rigid side of the actuator.

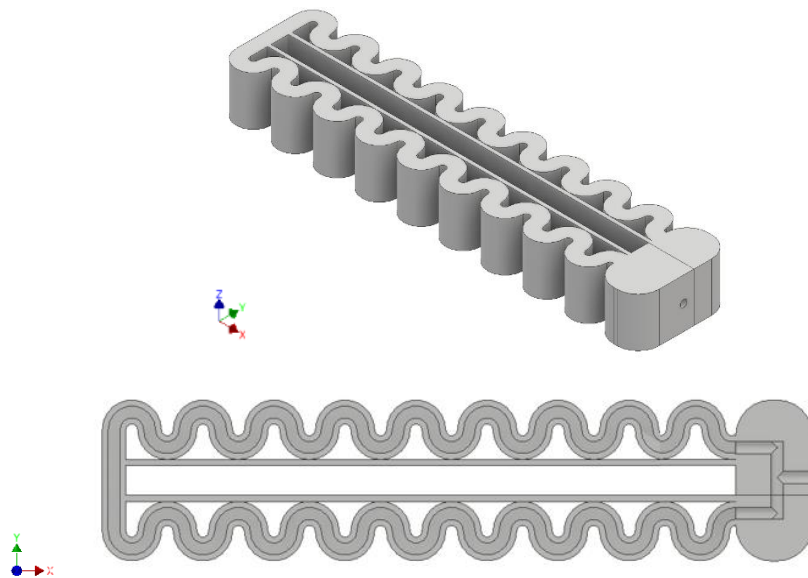


Figure 47. Close dual bellow pneumatic actuator CAD model.

The printing process took 9 hours to be completed. The printed actuator has a weight of 22.77 grams, and a total length of 120 mm in the x-direction.

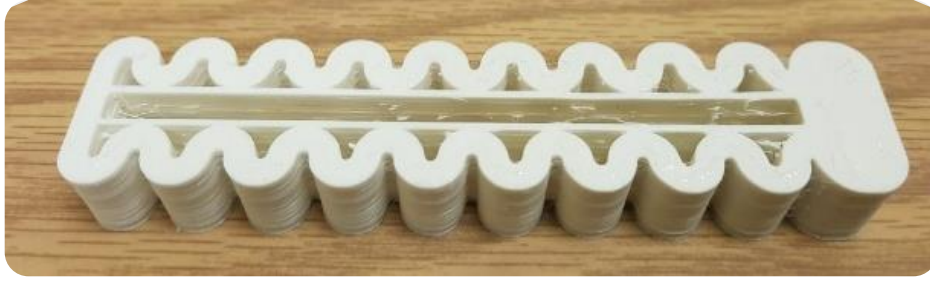


Figure 48. 3D printed close dual bellow pneumatic actuator.

It is expected that the actuator produces a bending motion on both sides, with opposite direction between the upper and lower part of the actuator, forming an oval shape when pressurized. This motion could work as a grip, where the sides of the structure could be opened and closed for better holding. The computational simulation shows the expected motion of the actuator, achieving a maximum oval structure under 25 psi before failure. The mesh of the entire structure has 76,515 elements with an average element quality of 0.64, discretizing the structure properly for computational analysis. The model reached convergence after 109 iterations with an error of  $1 \times 10^{-5}$  demonstrating accurate results.

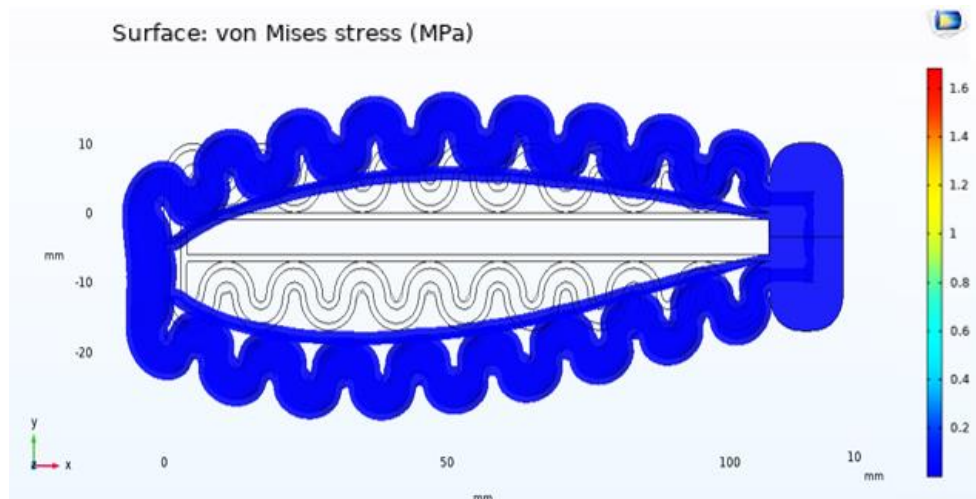


Figure 49. FEA - Bending-open behavior under a pressure of 25 psi. Von Mises Stress [MPa]

The experimental test demonstrated the grip functionality of the actuator lifting a rigid cylinder. The actuator was pressurized under 25 psi, reaching the maximum internal diameter of the structure. Then, a rigid cylinder was placed inside the actuator. Once the piece is located into

the hole of the structure the compressed air was released, producing a closing movement in the structure, holding the piece with good stability and sufficient friction to lift the piece.



Figure 50. Bending-open behavior under a pressure of 25 psi.



Figure 51. Grip functionality under a pressure of 25 psi.

This type of soft pneumatic actuator was capable of lifting a 3D printed cylinder with an external diameter of 30 mm and 52g of total weight. The actuator presented a maximum diameter of 32 mm under 25 psi.

### 4.3 Flexible sensors

A 3D finite element model was built for the sensors previously described. The model was built and analyzed using COMSOL Multiphysics 5.4 software. The model predicts the response and behavior of the sensors under different pressures. The pressure was modeled using a load ramping function, solving a sequence of intermediate problems with gradually increasing load

values and using the solutions from each previous step as the initial condition for the next step. The pressure was defined from 0 to 30 kPa with increments of 500 Pa.

### 4.3.1 Capacitance sensor

This computational study used the solid mechanics interface from the structural mechanics module to model the linear elastic (ETPU - conductive) and hyperplastic materials (TPU – nonconductive). In this case, the flexible conductive material is modeled as a linear elastic material, where Hooke's law related the stress tensor to the elastic strain tensor described by:

$$\sigma = \sigma_{ex} + C : \varepsilon_{el} = \sigma_{ex} + C : (\varepsilon - \varepsilon_{inel}) \quad (4.19)$$

Where  $C$  is the 4<sup>th</sup> order elasticity tensor defined by the material properties. In this study, the linear elastic material is defined by its Young's modulus, Poisson's ratio, and density (described in chapter 3). The elastic strain  $\varepsilon_{el}$  is the difference between the total strain  $\varepsilon$  and all inelastic strains  $\varepsilon_{inel}$ . There may also be an extra stress contribution  $\sigma_{ex}$  with contribution from initial stresses and viscoelastic stresses. For this material, the elastic strain density is defined by:

$$W_s = \frac{1}{2} \varepsilon_{el} : (C : \varepsilon_{el} + 2\sigma_0) = \frac{1}{2} \varepsilon_{el} : (\sigma + \sigma_0) \quad (4.20)$$

On the other hand, the electrostatics interface from the AC/DC module is utilized to model the capacitance formed by the electrodes and the dielectric material. The electric scalar potential,  $V$ , satisfies Poisson's equation:

$$-\nabla \cdot (\varepsilon_0 \varepsilon_r \nabla V) = \rho \quad (4.21)$$

Where  $\varepsilon_0$  is the permittivity of the free space,  $\varepsilon_r$  is the relative permittivity, and  $\rho$  is the space charge density. The electric field and the displacement are obtained from the gradient of  $V$ :

$$E = -\nabla V \quad (4.22)$$

$$D = \varepsilon_0 \varepsilon_r E \quad (4.23)$$

Both modules are coupled by the electromechanical forces module. This coupling module model the electromechanical interaction between deformable solids and electric fields, particularly in case when the deformations of the structure can significantly affect the electric field distribution.

For finite deformations, the expression for the electromagnetic stress and material polarization can be derived using the following thermodynamic potential called electric enthalpy:

$$H_{eme} = W_s(C) - \frac{1}{2} \varepsilon_0 \varepsilon_r J C^{-1} : (E \otimes E) \quad (4.24)$$

And the right Cauchy-Green deformation tensor is:

$$C = F^T F \quad (4.25)$$

With  $F = \nabla u + I$ , and  $J = \det(F)$ . The mechanical energy function  $W_s(C)$  depends on the solid model used. The second Piola-Kirchhoff stress tensor is given by:

$$S = 2 \frac{\partial H_{eme}}{\partial C} \quad (4.26)$$

And the electric displacement can be calculated as:

$$D_m = \frac{\partial H_{eme}}{\partial E} \quad (4.27)$$

The dielectric material used in this type of sensor was air, having a relative permittivity of 1. Air was selected because it facilitates the reduction of the distance between the electrodes, without the need of applying a higher stress to deform that extra material between them. Fixed boundary conditions were applied on the perimeter of the membrane and the pressure was applied to the surface of the membrane where the electrodes were located.

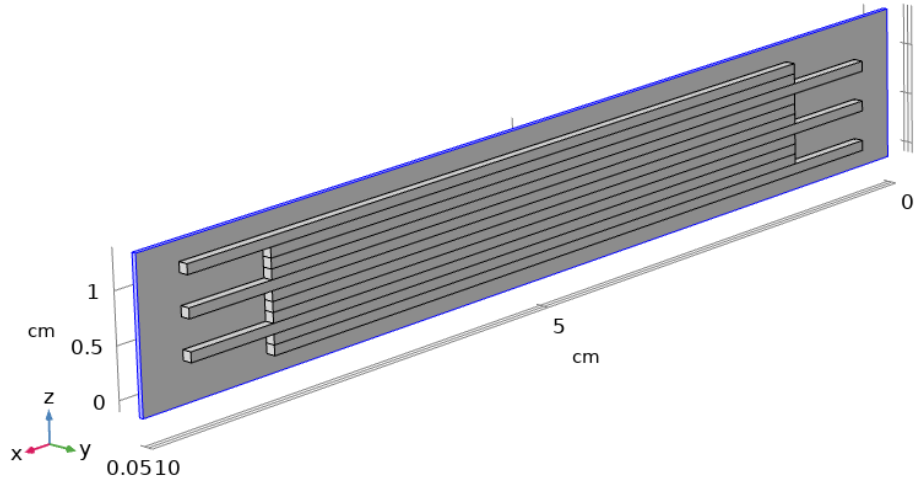


Figure 52. Fixed boundary conditions on the capacitance sensor.

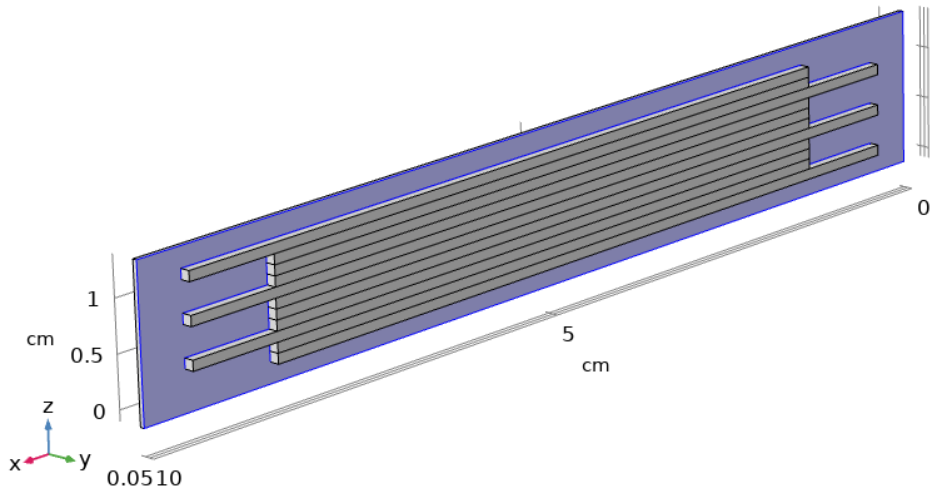


Figure 53. Boundary load on the capacitance sensor.

One of the electrodes of the capacitor was used as a terminal, applying a voltage of 1 V; and the other one was used as ground. Charge conservation was applied to the air elements located between each line of the electrodes. The structure of this sensor was discretized in a mesh having 51,727 elements with an average element quality of 0.67, discretizing the structure properly for computational analysis.

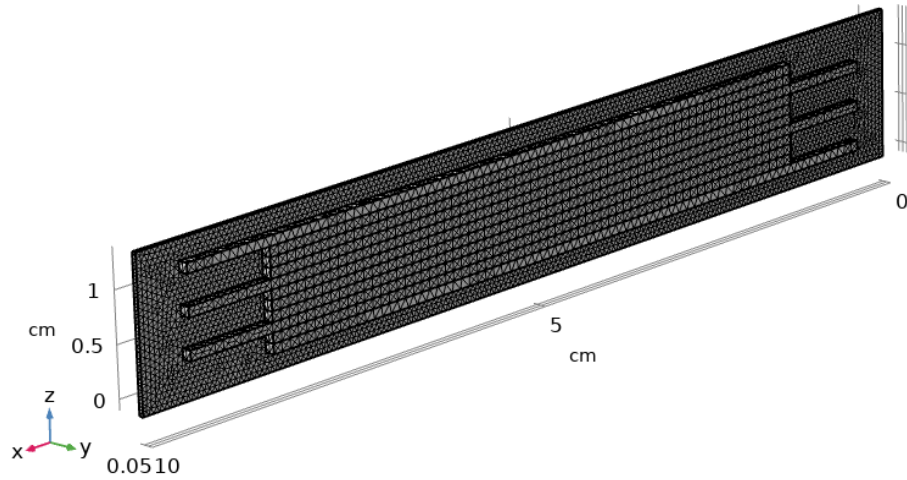


Figure 54. Computational mesh of the capacitance sensor.

The model reached convergence after 200 iterations with an error of  $8.4 \times 10^{-6}$  demonstrating accurate results. The displacement of the sensor when it is pressurized to the maximum pressure is illustrated in Figure 55.

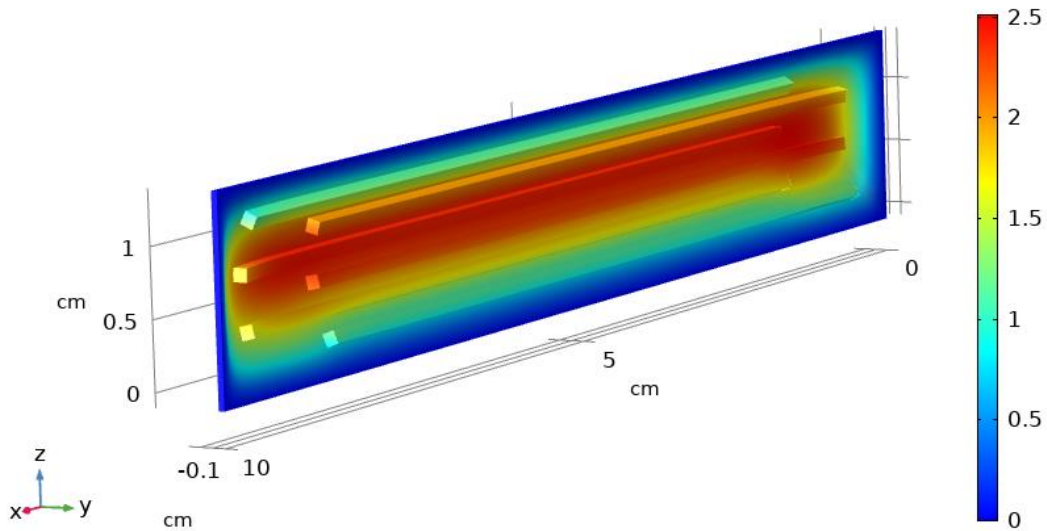


Figure 55. Total displacement under 30 kPa – capacitance sensor.

Figure 55 shows how the membrane is deformed and expanded in the same directions where the pressure is applied. As we expected the center of the membrane presents the highest displacement in the structure, with a maximum value of 2.5 mm.

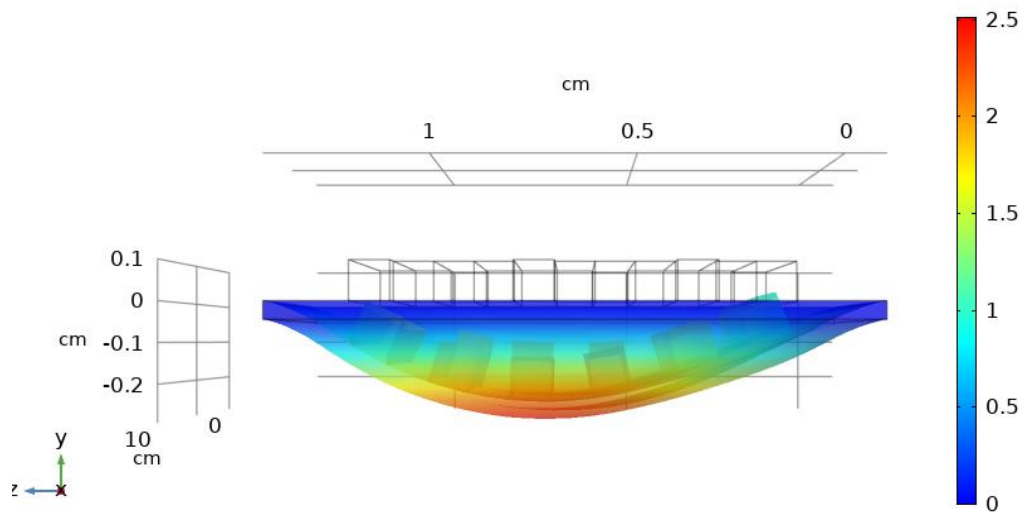


Figure 56. Total displacement under 30 kPa in the Y, Z plane – capacitance sensor.

Figure 56 presents the total displacement of the structure under the maximum pressure in the Y, Z plane. This view allows to observe how the deformation produced in the membrane causes a displacement of the electrodes reducing the distance between them. In addition, it is possible to observe that at the maximum pressure, the membrane presents a semi-elliptical shape. Based on Figure 29 it is possible to determine that most of the structure is under a low stress condition ( $<2$  MPa) that is, under the yield strength of the material. Therefore, the structure can return to its initial position without any permanent deformation. Figure 57 shows the Von Mises stress of the structure under 30 kPa. The areas with higher stress are located in the regions near to the fixed boundaries.

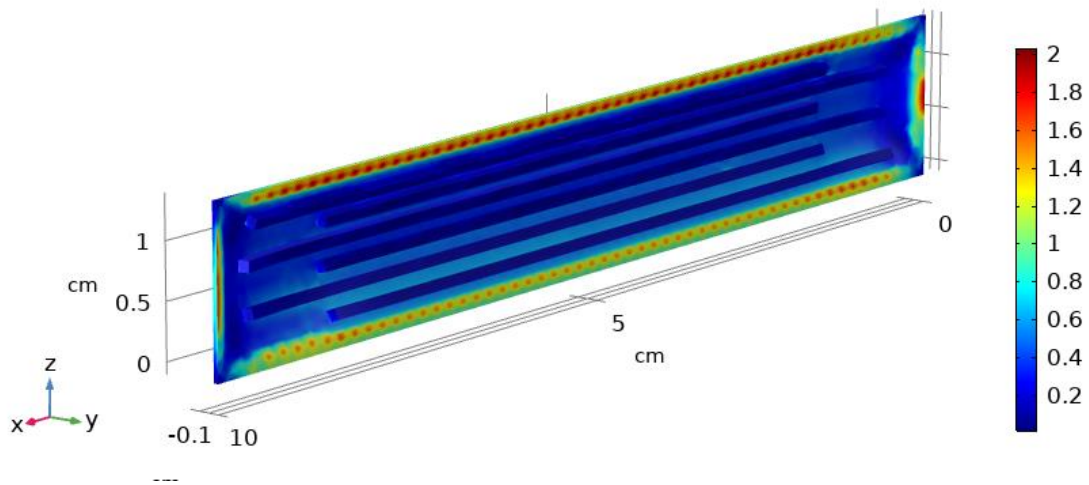


Figure 57. Von Mises Stress [MPa] – Capacitance sensor.

The capacitance results demonstrate the functionality of the sensor showing how the capacitance of the sensor increases in relationship with the applied pressure. Figure 58 shows the characteristic behavior of the capacitance of the sensor, where at beginning the value is almost double the capacitance value with a pressurization of approximately 5 kPa. After that region, the slope of the capacitance is reduced, and a stabilization trend can be observed. That is caused because the hyperplastic material that composes the membrane reaches an elastic region where the strain of the material is reduced. In addition, the geometry of the sensor and the applied boundary conditions create limitations in the deformation of the sensor. The sensor was able to increase its initial capacitance value (3.1 pF) almost three times when was exposed to 30 kPa. The capacitance of the sensor behaves as expected, similar to a capacitor in a charging condition.

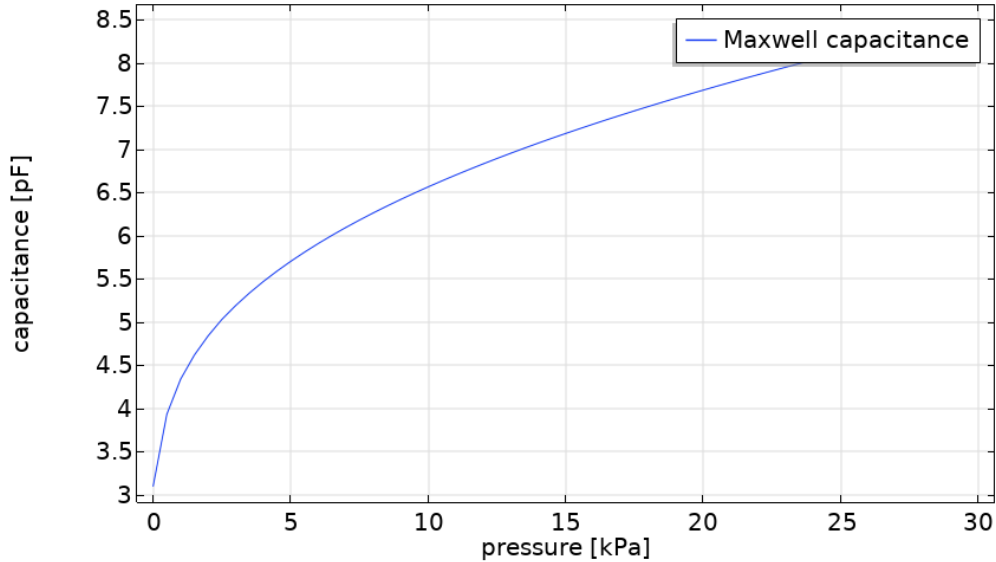


Figure 58. Capacitance [pF] vs Pressure [kPa] – Capacitance sensor.

### 4.3.2 Resistance sensor

This computational study used the solid mechanics interface from the structural mechanics module to model the lineal elastic (ETPU - conductive) and hyperplastic materials (TPU – nonconductive). The models were explained in the previous section of this chapter. In this case, the flexible conductive material experiences a resistance change due to the change of geometry resulting from applied mechanical stresses. The resistance of the conductive material is calculated using the resistance derived from Ohm’s law, explained in chapter 3.

As in the capacitance sensor, fixed boundary conditions were applied on the perimeter of the membrane. However, the pressure was applied on the opposite surface of the membrane, making that the resistor located in the other surface present the highest elongation.

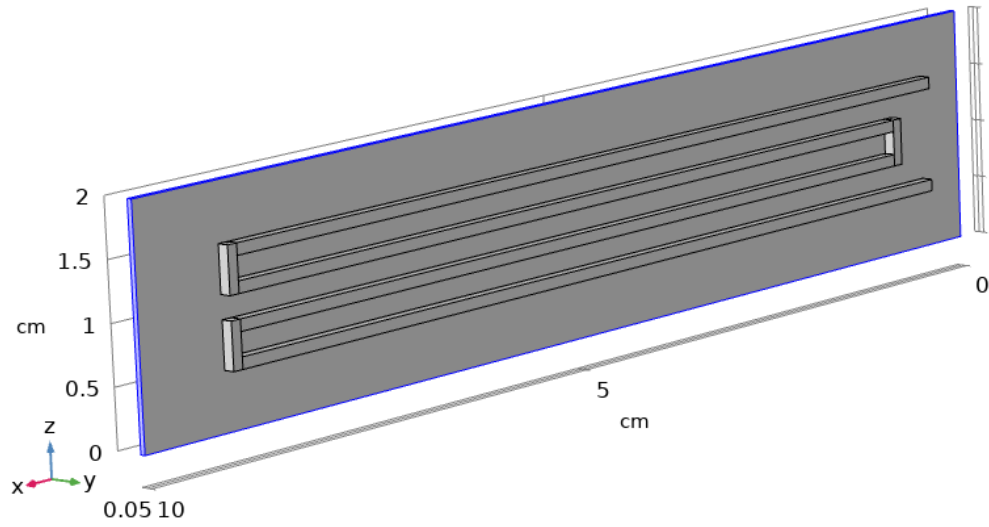


Figure 59. Fixed boundary conditions on the resistance sensor.

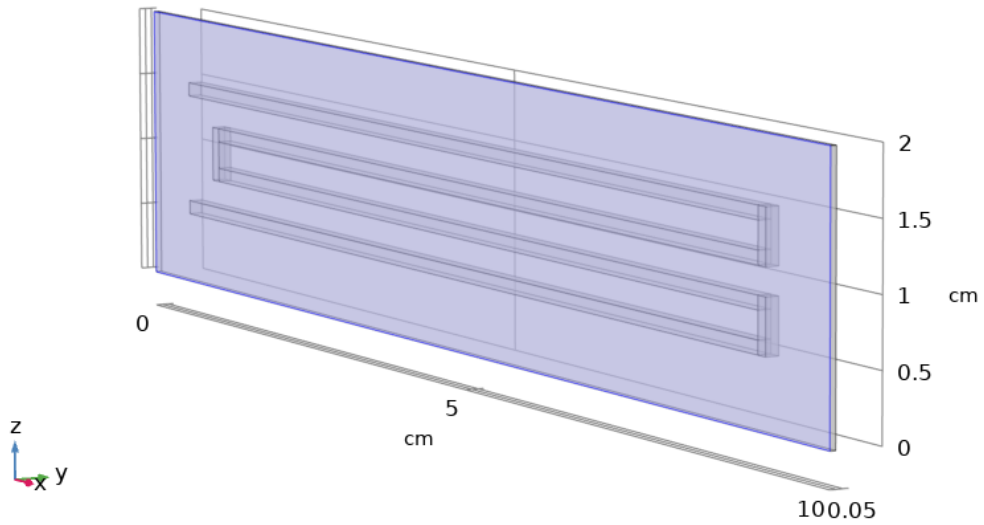


Figure 60. Boundary load on the resistance sensor.

One of the ends of the resistor was used as a terminal applying a current of 1 A on the cross-sectional area; and the other one was used as ground. The structure of this sensor was discretized in a mesh having 46,784 elements with an average element quality of 0.66, discretizing the structure properly for computational analysis.

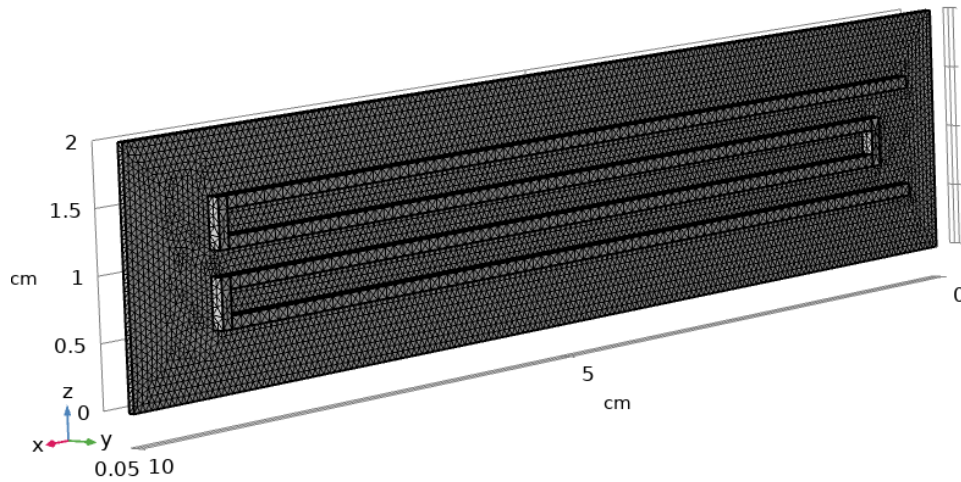


Figure 61. Computational mesh of the resistance sensor.

The model reached convergence after 150 iterations with an error of  $3.3 \times 10^{-6}$  demonstrating accurate results. The displacement of the sensor when it is pressurized to the maximum analyzed pressure is illustrated in Figure 62.

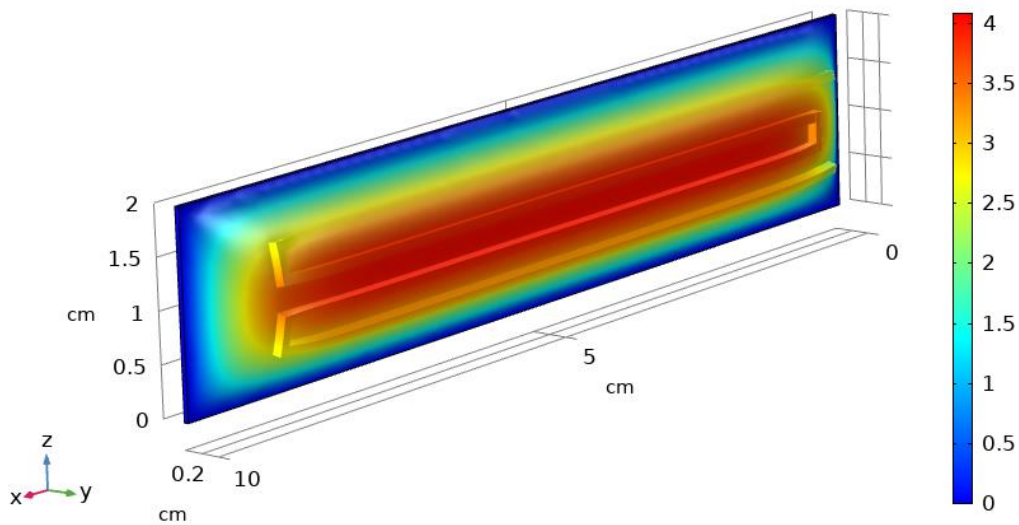


Figure 62. Total displacement under 30 kPa – Resistance sensor.

Figure 62 shows how the membrane is deformed and expanded in the same directions where the pressure is applied. As expected, the center of the membrane presents the highest displacement in the structure, with a maximum value of 4 mm. In addition, it is possible to observe

that the entire conductive element presents a displacement with a value between 2.8 and 4 mm. The conductive element was deformed causing an elongation in its structure.

Based on Figure 29, it is possible to determine that most of the structure is under a low stress condition ( $<3$  MPa) that is, under the yield point of the material. Therefore, the structure can return to its initial position without any permanent deformation. Figure 63 shows the Von Mises stress of the structure under 30 kPa. The areas with higher stress are located in the regions near to the fixed boundaries.

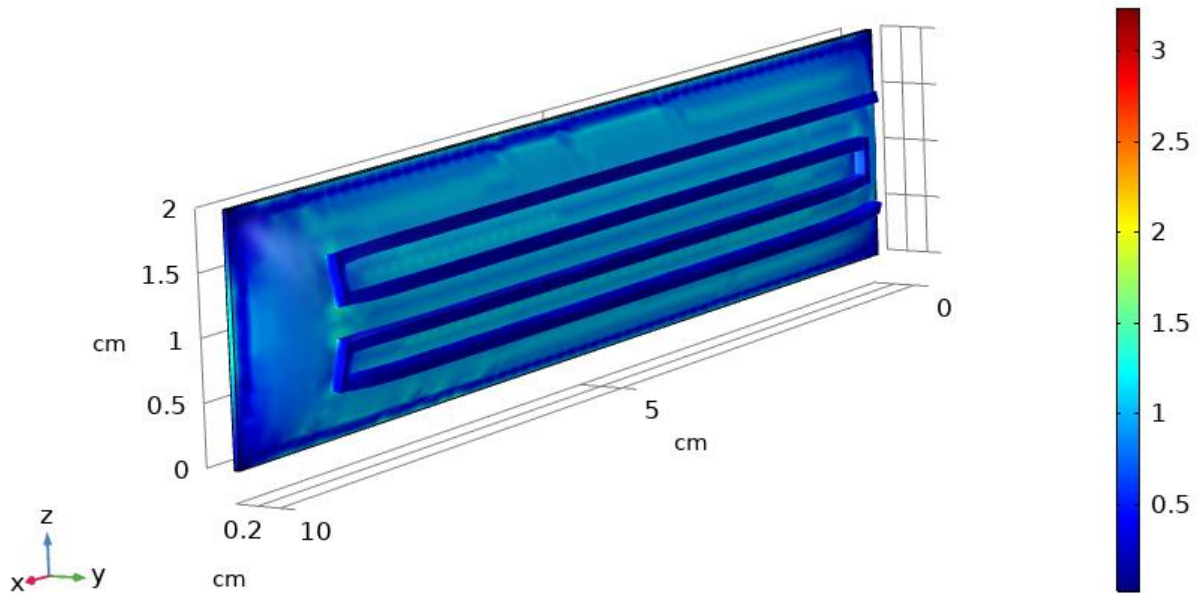


Figure 63. Von Mises Stress [MPa] – Resistance sensor.

The resistance results demonstrate the functionality of the sensor showing how the resistance of the sensor increases in relationship with the applied pressure. Figure 64 shows the characteristic behavior of the resistance of the sensor, where between 0 and 5 kPa is capable of increasing its resistance  $300 \Omega$ . In this region, the sensor is deformed more rapidly due to the properties of the hyperplastic material causing higher rate elongations in the resistor element, and therefore greater increases in its resistance. After that region, the resistance has a linear behavior. The sensor was capable of increasing its resistance approximately  $1200 \Omega$  when it was exposed to 30 kPa of applied pressure.

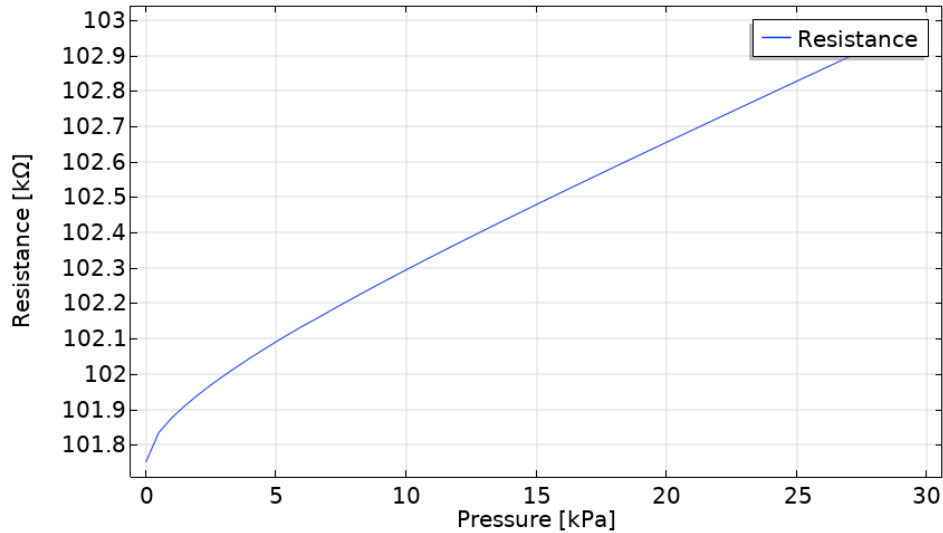


Figure 64. Capacitance [pF] vs Pressure [kPa] – Resistance sensor.

### 4.3.3 3D printed sensors

The designed sensors were 3D printed using the same materials that were selected for the computational simulations. Both sensors were manufactured using the “LulzbotTaz 6” 3D printer. A special printing head for flexible materials was used enhancing the quality and control in the printing process. The sensors were printed using the following printing settings:

- Layer height: 0.15 mm
- Infill density: 100%
- TPU Printing temperature: 205°C
- ETPU Printing temperature: 220°C
- Build plate temperature: 60°C
- Printing speed: 10 mm/s

Figures 65 and 66 show the preliminary results of the 3D printed capacitance and resistance sensors, respectively. The printed sensors have the same dimensions as the ones described before in the design section. There is only one main change in the design of the printed sensors. First, in the capacitance sensor a connection between the conductive lines of each electrode was added to connect the entire electrode and begin able to measure the capacitance changes easily. Second, in

the resistance sensor two prime towers were added at the ends of the conductive element to facilitate the measure of resistance of the structure.



Figure 65. 3D printed capacitance sensor.

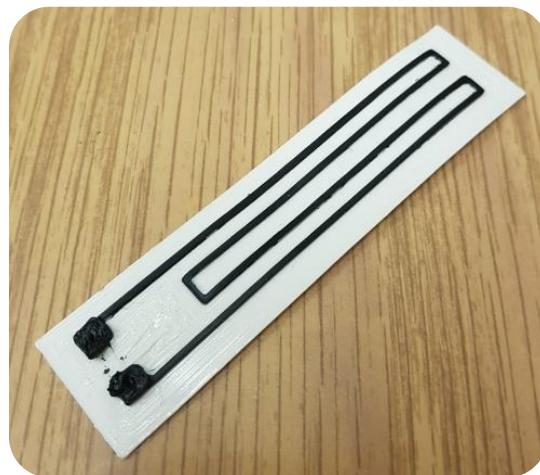


Figure 66. 3D printed resistance sensor.

## CHAPTER 5. CONCLUSIONS

### 5.1 Electroactive polymer structures

The proposed design of a 3D printed DEAP structure was successfully produced and characterized. The manufacturing process to produce the dielectric membranes was based on FDM technique. The electromechanical properties of these 3D printed membranes were characterized. TPU demonstrated to be an appropriate dielectric material for electroactive structures, having a high dielectric constant compared with other polymers. Printed TPU have a dielectric constant of 6.3, this is more than the double of the value for polymers like: Silicone Nusil, Silicone Dow Corning HS3, Silicone Dow Corning Sylgard 186, Polybutadiene Aldrich PBD, and Isoprene Natural Rubber Latex. Similarly, TPU material showed excellent elongation properties.

Standardized tensile tests were performed to analyze and characterize the response of the dielectric material under external loads, and the effect of the 3D printing manufacturing process. The effect of the thickness and printing angle of the elastomeric material were studied, concluding that the numbers of layers and the orientation in which it is printed affects the resistance of the material to electric fields and mechanical loads. However, this characteristic of 3D printing process can be used to control the preferential directions of actuation.

Surface topography of produced dielectric membranes was also studied, finding that printed samples have a specific roughness which depends on the used printing path. The surface of the printed samples has a wavelike shape compound of approximately equidistant peaks and valleys. Concentric circle pathways produced smoother surfaces with a tight profile roughness compared to line based pathways, by approximately 30 microns.

The actuation results evidences replicability of the DEAP structures by the proposed manufacturing process, obtaining consistent and relatively constant behavior of the produced actuators. 3D printing of flexible dielectric materials utilizing FDM as manufacturing process was successfully demonstrated and validates the possibility of manufacture new designs of electroactive structures that involves multilateral printing in one continuous process.

## 5.2 Soft actuators

A functional 3D printed pneumatic bellow actuator was manufactured using fused deposition modeling, without the need of support material. The 3D printed samples were totally sealed without the use of any sealing material or post processes. In addition, two different gripper designs were manufactured and tested, demonstrating the functionality of these types of structures to lift objects. Those designs can be used in many applications, being capable to produce force and torque outputs proportional with the internal pressure of the structure.

The proposed 3D finite element model is able to predict the response of the designed actuator with an error of less than seven percent. Computational and experimental results match making it possible to extend the methodology used in this work to analyze and produce more complex structures such as a complete robotic hand. Multi-material printed parts need to be explored in these types of applications, where a rigid material can control and optimize the performance of the actuators, and conductive material can produce direct sensing of the deformation of the structure.

## 5.3 Flexible sensors

This work demonstrates two different designs of flexible sensors that can be manufactured using additive manufacturing by fused deposition modeling. Computational simulation results prove the conceptual idea of structures that can change their capacitance and resistance based on the deformation produced by external forces. The capacitance sensor was able to increase its capacitance from 3 to 8.5 pF when it was exposed to a pressure of 30 kPa. The resistance sensor was able to increase its resistance from 101.8 to 103 k $\Omega$  when it was exposed to a pressure of 30 kPa. The designed sensors have great potential to be used embedded into 3D printed structures, being able to measure deformation or fatigue of rigid bodies.

The sensors were 3D printed successfully, showing good bonding between the two selected materials. Printed parts exhibit great quality and consistency. Preliminary tensile tests showed good structural integrity of the sensors. Experimental tests need to be performed to characterize the response and sensitivity of each sensor. In addition, multiple sensors need to be printed in order to test the replicability of these type of devices, using 3D printing as the manufacturing process.

## 5.4 Future work

This study needs to be complemented with a series of experimental and computational tests, where different designs of the studied structures are analyzed. In addition, is necessary to develop optimization processes in which the characteristics of the printed elastomeric material are improved. For example, analyze if some specific printing path could improve the maximum elongation and roughness of the manufactured elastomeric material. Mechanical properties of 3D printed flexible materials could be analyzed studying the behavior of printed samples where the infill material is oriented using more than one printing angle. The elastic hysteresis of the hyperplastic material needs to be tested and analyzed to determine its characteristic behavior under extension and contraction. The manufactured structures require fatigue testing to determine the resistance of the structure under cyclic loading, these results will determine if the designed structures are useful for some specific application. All of these experimental results should be compared with other manufacturing process. I propose to manufacture all the studied structures using casting and compare the results from this conventional manufacturing process with the innovative 3D printing process.

The final step of the project would be the design and manufacture of complex structures that combine sensors and actuators in a single structure, that can be 3D printed in one continuous process. The designed structure needs to solve some specific problem (from industry or human necessity) to reinforce the innovation of the entire project and serve as the first approach to functional 3D printed structures.

## REFERENCES

- Aaron Rosenthal, M., & Pei, Q. (2008). MULTIPLE-DEGREES-OF-FREEDOM ROLL ACTUATORS. In *Dielectric Elastomers as Electromechanical Transducers* (pp. 91–102). Elsevier. <https://doi.org/10.1016/B978-0-08-047488-5.00009-5>
- Amjadi, M., Yoon, Y. J., & Park, I. (2015). Ultra-stretchable and skin-mountable strain sensors using carbon nanotubes–Ecoflex nanocomposites. *Nanotechnology*, 26(37), 375501. <https://doi.org/10.1088/0957-4484/26/37/375501>
- Al-Rubaiai, M., Tsuruta, R., Gandhi, U., Wang, C., & Tan, X. (2019). A 3D-printed stretchable strain sensor for wind sensing. *Smart Materials and Structures*, 28(8), 084001. <https://doi.org/10.1088/1361-665X/ab1fa9>
- Araromi, O. A., Conn, A. T., Ling, C. S., Rossiter, J. M., Vaidyanathan, R., & Burgess, S. C. (2011). Spray deposited multilayered dielectric elastomer actuators. *Sensors and Actuators A: Physical*, 167(2), 459–467. <https://doi.org/10.1016/j.sna.2011.03.004>
- Bar-Cohen, Y., Cardoso, V. F., Ribeiro, C., & Lanceros-Méndez, S. (2017). Electroactive Polymers as Actuators. In *Advanced Piezoelectric Materials* (pp. 319–352). <https://doi.org/10.1016/B978-0-08-102135-4.00008-4>
- Belforte, G., Eula, G., Ivanov, A., & Sirolli, S. (2014). Soft Pneumatic Actuators for Rehabilitation. *Actuators*, 3(2), 84–106. <https://doi.org/10.3390/act3020084>
- Biddiss, E.; Chau, T. Dielectric Elastomers as Actuators for Upper Limb Prosthetics: Challenges and Opportunities. *Med. Eng. Phys.* 2008, 30 (4), 403–418.
- Carpi, F., & De Rossi, D. (2008). CONTRACTILE MONOLITHIC LINEAR ACTUATORS. In *Dielectric Elastomers as Electromechanical Transducers* (pp. 123–131). Elsevier. <https://doi.org/10.1016/B978-0-08-047488-5.00012-5>
- C. Boller (2001), *Composites for Sensors and Actuators*, Encyclopedia of Materials: Science and Technology. Springer International Publishing. <https://doi.org/10.1016/B0-08-043152-6/00256-4>.
- Cardoso, V. F.; Ribeiro, C.; Lanceros-Mendez, S. *Metamorphic Biomaterials*. In *Bioinspired Materials for Medical Applications*; Elsevier, 2017; pp 69–99.

- Choong, C.L.; Shim, M.B.; Lee, B.S.; Jeon, S.; Ko, D.S.; Kang, T.H.; Bae, J.; Lee, S.H.; Byun, K.E.; Im, J.; et al. Highly stretchable resistive pressure sensors using a conductive elastomeric composite on a micropyramid array. *Adv. Mater.* 2014, 26, 3451–3458.
- Davis, D.L.; Carlson, J.A. Fluidic Actuator. US Patent No. 6868773B2, 2005.
- Davis, S. (2018). Pneumatic Actuators. *Actuators*, 7(3), 62. <https://doi.org/10.3390/act7030062>
- Diabase Engineering (2018) X60 Ultra Flexible Filament. <https://flexionextruder.com/shop/x60-ultra-flexible-filament-white/> (accessed 15 Jan 2019).
- Drotman, D., Ishida, M., Jadhav, S., & Tolley, M. T. (2019). Application-Driven Design of Soft, 3-D Printed, Pneumatic Actuators With Bellows. *IEEE/ASME Transactions on Mechatronics*, 24(1), 78–87. <https://doi.org/10.1109/TMECH.2018.2879299>
- D09 Committee. Test Methods for AC Loss Characteristics and Permittivity (Dielectric Constant) of Solid Electrical Insulation; ASTM International. <https://doi.org/10.1520/D0150-18>.
- D20 Committee. Test Method for Tensile Properties of Plastics; ASTM International. <https://doi.org/10.1520/D0638-14>.
- Galley, A. (n.d.). Pneumatic Hyperelastic Robotic End-Effector for Grasping Soft Curved Organic Objects. 143.
- Ge J et al (2016) A stretchable electronic fabric artificial skin with pressure-, lateral strain-, and flexion-sensitive properties. *Adv Mater* 28:722–728
- Ge, L., Dong, L., Wang, D., Ge, Q., & Gu, G. (2018). A digital light processing 3-D printer for fast and high-precision fabrication of soft pneumatic actuators. *Sensors and Actuators A: Physical*, 273, 285–292. <https://doi.org/10.1016/j.sna.2018.02.041>
- Gonzalez (2018) D., “3-D Printing of Dielectric Electroactive Polymer actuators and Characterization of dielectric Flexible Materials” ASME 2018 Conference on Smart Materials, Adaptive Structures and Intelligent Systems SMASIS. American Society of Mechanical Engineers, SMASIS2018-8011
- Guo, S.-Z., Qiu, K., Meng, F., Park, S. H., & McAlpine, M. C. (2017). 3D Printed Stretchable Tactile Sensors. *Advanced Materials*, 29(27), 1701218. <https://doi.org/10.1002/adma.201701218>

- Ha, S. M., Yuan, W., Pei, Q., Pelrine, R., & Stanford, S. (2006). Interpenetrating Polymer Networks for High-Performance Electroelastomer Artificial Muscles. *Advanced Materials*, 18(7), 887–891. <https://doi.org/10.1002/adma.200502437>
- Ha, S. M.; Yuan, W.; Pei, Q.; Pelrine, R.; Stanford, S. Interpenetrating Networks of Elastomers Exhibiting 300% Electrically-Induced Area Strain. *Smart Mater. Struct.* 2007, 16 (2), S280–S287. <https://doi.org/10.1088/0964-1726/16/2/S12>.
- Hamzah, Hairul & Keattch, Oliver & Covill, Derek & Patel, Bhavik. (2018). The effects of printing orientation on the electrochemical behaviour of 3D printed acrylonitrile butadiene styrene (ABS)/carbon black electrodes. *Scientific Reports*. 8. 10.1038/s41598-018-27188-5
- Han, T., Kundu, S., Nag, A., & Xu, Y. (2019). 3D Printed Sensors for Biomedical Applications: A Review. *Sensors*, 19(7), 1706. <https://doi.org/10.3390/s19071706>
- Hashemi, S., Bentivegna, D., & Durfee, W. (2020). Bone-Inspired Bending Soft Robot. *Soft Robotics*, soro.2019.0183. <https://doi.org/10.1089/soro.2019.0183>
- Hollerbach, J., Hunter, I. W., Ballantyne, J., Khatib, O., Craig, J. and Lozano, P. (1992). *A Comparative Analysis of Actuator Technologies for Robotics*. MIT Press, Cambridge, MA, pp. 299–342.
- Hou, C.; Wang, H.; Zhang, Q.; Li, Y.; Zhu, M. Highly conductive, flexible, and compressible all-graphene passive electronic skin for sensing human touch. *Adv. Mater.* 2014, 26, 5018–5024.
- Hu, W., Li, W., & Alici, G. (2018). 3D Printed Helical Soft Pneumatic Actuators. 2018 IEEE/ASME International Conference on Advanced Intelligent Mechatronics (AIM), 950–955. <https://doi.org/10.1109/AIM.2018.8452456>
- Hunter, I. W., & Lafontaine, S. (1992). A comparison of muscle with artificial actuators. *Technical Digest IEEE Solid-State Sensor and Actuator Workshop*, 178–185. <https://doi.org/10.1109/SOLSEN.1992.228297>
- Hwang, Y., Paydar, O. H., & Candler, R. N. (2015). Pneumatic microfinger with balloon fins for linear motion using 3D printed molds. *Sensors and Actuators A: Physical*, 234, 65–71. <https://doi.org/10.1016/j.sna.2015.08.008>
- Jeong YR, Park H, Jin SW, Hong SY, Lee SS, Ha JS (2015) Highly stretchable and sensitive strain sensors using fragmentized graphene foam. *Adv Func Mater* 25:4228–4236

- Jing Z, Guang-Yu Z, Dong-Xia S (2013) Review of graphene-based strain sensors. *Chin Phys B* 22:057701
- Kanoun O et al (2014) Flexible carbon nanotube films for high performance strain sensors. *Sensors* 14:10042–10071
- Keong, B. A. W., & Hua, R. Y. C. (2018). A Novel Fold-Based Design Approach toward Printable Soft Robotics Using Flexible 3-D Printing Materials. *Advanced Materials Technologies*, 3(2), 1700172. <https://doi.org/10.1002/admt.201700172>
- Keysight Technologies (2016) Solution for measuring permittivity and permeability with LCR meters and impedance analyzers. <http://literature.cdn.keysight.com/litweb/pdf/5980-2862EN.pdf> (accessed 15 Jan 2019).
- King, A. M., Loiselle, D. S., & Kohl, P. (2004). Force generation for locomotion of vertebrates: Skeletal muscle overview. *IEEE Journal of Oceanic Engineering*, 29(3), 684–691. <https://doi.org/10.1109/JOE.2004.833205>
- Kim, D.H.; Lu, N.S.; Ma, R.; Kim, Y.S.; Kim, R.H.; Wang, S.D.; Wu, J.; Won, S.M.; Tao, H.; Islam, A.; et al. Epidermal electronics. *Science* 2011, 333, 838–843.
- Krause, J., & Bhounsule, P. (2018). A 3-D Printed Linear Pneumatic Actuator for Position, Force and Impedance Control. *Actuators*, 7(2), 24. <https://doi.org/10.3390/act7020024>
- Kornbluh, R. Fundamental Configurations for Dielectric Elastomer Actuators. In *Dielectric Elastomers as Electromechanical Transducers*; Elsevier, 2008; pp 79–90. <https://doi.org/10.1016/B978-0-08-047488-5.00008-3>.
- Kovacs, G., Düring, L., Michel, S., & Terrasi, G. (2009). Stacked dielectric elastomer actuator for tensile force transmission. *Sensors and Actuators A: Physical*, 155(2), 299–307. <https://doi.org/10.1016/j.sna.2009.08.027>
- Kukolj, M. Axially Contractible Actuator. U.S. Patent No. 4733603, 1988.
- Kumar, N., & Rao, V. V. (2016). Hyperelastic Mooney-Rivlin Model: Determination and Physical Interpretation of Material Constants. 6(1), 4.
- Kwok, S. W., Goh, K. H. H., Tan, Z. D., Tan, S. T. M., Tjiu, W. W., Soh, J. Y., Ng, Z. J. G., Chan, Y. Z., Hui, H. K., & Goh, K. E. J. (2017). Electrically conductive filament for 3D-printed circuits and sensors. *Applied Materials Today*, 9, 167-175. <https://doi.org/10.1016/j.apmt.2017.07.001>

- Laschi, C., Rossiter, J., Iida, F., Cianchetti, M., & Margheri, L. (Eds.). (2017). *Soft Robotics: Trends, Applications and Challenges: Proceedings of the Soft Robotics Week, April 25-30, 2016, Livorno, Italy (Vol. 17)*. Springer International Publishing.  
<https://doi.org/10.1007/978-3-319-46460-2>
- Leigh, S. J., Bradley, R. J., Purssell, C. P., Billson, D. R., & Hutchins, D. A. (2012). A Simple, Low-Cost Conductive Composite Material for 3D Printing of Electronic Sensors. *PLoS ONE*, 7(11), e49365. <https://doi.org/10.1371/journal.pone.0049365>
- Lendlein, A., Feng, Y., Grijpma, D. W., & Zhao, Y. (2018). Smart Materials. *ChemPhysChem*, 19(16), 1938–1940. <https://doi.org/10.1002/cphc.201800578>
- Li, K., Wei, H., Liu, W., Meng, H., Zhang, P., & Yan, C. (2018). 3D printed stretchable capacitive sensors for highly sensitive tactile and electrochemical sensing. *Nanotechnology*, 29(18), 185501. <https://doi.org/10.1088/1361-6528/aaafa5>
- Liu, C., Huang, N., Xu, F., Tong, J., Chen, Z., Gui, X., Fu, Y., & Lao, C. (2018). 3D Printing Technologies for Flexible Tactile Sensors toward Wearable Electronics and Electronic Skin. *Polymers*, 10(6). <https://doi.org/10.3390/polym10060629>
- Liu, X., Zhao, Y., Geng, D., Chen, S., Tan, X., & Cao, C. (2020). Soft Humanoid Hands with Large Grasping Force Enabled by Flexible Hybrid Pneumatic Actuators. *Soft Robotics*, soro.2020.0001. <https://doi.org/10.1089/soro.2020.0001>
- Lou, Z.; Chen, S.; Wang, L.; Jiang, K.; Shen, G. An ultra-sensitive and rapid response speed graphene pressure sensors for electronic skin and health monitoring. *Nano Energy* 2016, 23, 7–14.
- Madden, J. D. W. (2008). DIELECTRIC ELASTOMERS AS HIGH-PERFORMANCE ELECTROACTIVE POLYMERS. In *Dielectric Elastomers as Electromechanical Transducers* (pp. 13–21). Elsevier. <https://doi.org/10.1016/B978-0-08-047488-5.00002-2>
- Material info: PI-ETPU 95-250 Carbon Black. (n.d.). Rubber 3D Printing. Retrieved April 20, 2020, from <https://rubber3dprinting.com/pi-etpu-95-250-carbon-black/>
- Mangla, O., Srivastava, A., Malhotra, Y., & Ostrikov, K. (2014). Lanthanum oxide nanostructured films synthesized using hot dense and extremely non-equilibrium plasma for nanoelectronic device applications. *Journal of Materials Science*, 49(4), 1594–1605. <https://doi.org/10.1007/s10853-013-7842-3>

- MacCurdy, R., Katzschnann, R., Youbin Kim, & Rus, D. (2016). Printable hydraulics: A method for fabricating robots by 3-D co-printing solids and liquids. *2016 IEEE International Conference on Robotics and Automation (ICRA)*, 3878–3885. <https://doi.org/10.1109/ICRA.2016.7487576>
- Miriyev, A., Stack, K., & Lipson, H. (2017). Soft material for soft actuators. *Nature Communications*, 8(1). <https://doi.org/10.1038/s41467-017-00685-3>
- Mohd Ghazali, F. A., Mah, C. K., AbuZaiter, A., Chee, P. S., & Mohamed Ali, M. S. (2017). Soft dielectric elastomer actuator for micropump application. *Sensors and Actuators A: Physical*, 263, 276–284. <https://doi.org/10.1016/j.sna.2017.06.018>
- Mok Ha, S., Yuan, W., Pei, Q., Pelrine, R., & Stanford, S. (2008). INTERPENETRATING POLYMER NETWORKS AS HIGH PERFORMANCE DIELECTRIC ELASTOMERS. In *Dielectric Elastomers as Electromechanical Transducers* (pp. 43–50). Elsevier. <https://doi.org/10.1016/B978-0-08-047488-5.00005-8>
- Morin, A.H. Elastic Diaphragm. U.S. Patent No. 2642091, 1953.
- Nag, A., Mukhopadhyay, S. C., & Kosel, J. (2019). *Printed Flexible Sensors: Fabrication, Characterization and Implementation* (Vol. 33). Springer International Publishing. <https://doi.org/10.1007/978-3-030-13765-6>
- Newell, B., Garcia, J., & Krutz, G. (2018). Dielectric Electroactive Polymers with Chemical Pre-Strain: An Experimentally Validated Model. In *Actuators* (Vol. 7, No. 3, p. 50). Multidisciplinary Digital Publishing Institute.
- Paoletti, I., & Ceccon, L. (2018). The Evolution of 3D Printing in AEC: From Experimental to Consolidated Techniques. In D. Cvetković (Ed.), *3D Printing*. InTech. <https://doi.org/10.5772/intechopen.79668>
- Payen, D. J., & Bathe, K.-J. (2011). Improved stresses for the 4-node tetrahedral element. *Computers & Structures*, 89(13–14), 1265–1273. <https://doi.org/10.1016/j.compstruc.2011.02.009>
- Prahlad, H.; Kornbluh, R.; Pelrine, R.; Stanford, S.; Eckerle, J.; Oh, S. *Polymer Power: Dielectric Elastomers and Their Applications in Distributed Actuation and Power Generation*; Proceedings of ISSS: Bangalore, India, 2005; Vol. 13, p 8.
- Pelrine, R. (2000). High-Speed Electrically Actuated Elastomers with Strain Greater Than 100%. *Science*, 287(5454), 836–839. <https://doi.org/10.1126/science.287.5454.836>

- Pelrine, R., Kornbluh, R., Joseph, J., Heydt, R., Pei, Q., & Chiba, S. (2000). High-field deformation of elastomeric dielectrics for actuators. *Materials Science and Engineering: C*, 11(2), 89–100. [https://doi.org/10.1016/S0928-4931\(00\)00128-4](https://doi.org/10.1016/S0928-4931(00)00128-4)
- Pelrine, R. High-Speed Electrically Actuated Elastomers with Strain Greater Than 100%. *Science* 2000, 287 (5454), 836–839. <https://doi.org/10.1126/science.287.5454.836>.
- Pelrine, R., Sommer-Larsen, P., Kornbluh, R. D., Heydt, R., Kofod, G., Pei, Q., & Gravesen, P. (2001). Applications of dielectric elastomer actuators (Y. Bar-Cohen, Ed.; p. 335). <https://doi.org/10.1117/12.432665>
- Polyurethanes, P. C. Innovative material properties. <https://www.tpu.covestro.com/en/Technologies/Properties/Electrical-Properties> (accessed 15 Jan 2019).
- Romo-Estrada (2018) J., “Mechanical Iris Stretcher for Electroactive Polymers.” ASME 2018 Conference on Smart Materials, Adaptive Structures and Intelligent Systems SMASIS. American Society of Mechanical Engineers, SMASIS2018-7964
- Rim, Y.S.; Bae, S.H.; Chen, H.J.; De Marco, N.; Yang, Y. Recent progress in materials and devices toward printable and flexible Sensors. *Adv. Mater.* 2016, 28, 4415–4440.
- Schlaak, H. F.; Lotz, P.; Matysek, M. Multistack Contractile Actuators. In *Dielectric Elastomers as Electromechanical Transducers*; Elsevier, 2008; pp 109–122. <https://doi.org/10.1016/B978-0-08-047488-5.00011-3>.
- Shepherd, R. F., Ilievski, F., Choi, W., Morin, S. A., Stokes, A. A., Mazzeo, A. D., Whitesides, G. M. (2011). Multigait soft robot. *Proceedings of the National Academy of Sciences*, 108(51), 20400–20403. <https://doi.org/10.1073/pnas.1116564108>
- Shi, G.; Zhao, Z.H.; Pai, J.H.; Lee, I.; Zhang, L.Q.; Stevenson, C.; Ishara, K.; Zhang, R.J.; Zhu, H.W.; Ma, J. Highly sensitive, wearable, durable strain sensors and stretchable conductors using graphene/silicon rubber composites. *Adv. Funct. Mater.* 2016, 26, 7614–7625.
- Shih, B., Mayeda, J., Huo, Z., Christianson, C., & Tolley, M. T. (2018). 3D printed resistive soft sensors. 2018 IEEE International Conference on Soft Robotics (RoboSoft), 152-157. <https://doi.org/10.1109/ROBOSOFT.2018.8404912>
- Software Tracker - Video analysis and modeling tool V.5.0.6. Douglas Brown.

- Sommer-Larsen, P., Hooker, J. C., Kofod, G., West, K., Benslimane, M., & Gravesen, P. (2001). Response of dielectric elastomer actuators (Y. Bar-Cohen, Ed.; p. 157). <https://doi.org/10.1117/12.432641> <https://physlets.org/tracker/> (accessed 15 Jan 2019)
- Soreni-Harari, M., St. Pierre, R., McCue, C., Moreno, K., & Bergbreiter, S. (2020). Multimaterial 3D Printing for Microrobotic Mechanisms. *Soft Robotics*, 7(1), 59–67. <https://doi.org/10.1089/soro.2018.0147>
- Tolley, M. T., Shepherd, R. F., Mosadegh, B., Galloway, K. C., Wehner, M., Karpelson, M., Wood, R. J., & Whitesides, G. M. (2014). A Resilient, Untethered Soft Robot. *Soft Robotics*, 1(3), 213-223. <https://doi.org/10.1089/soro.2014.0008>
- Verl, A., Albu-Schäffer, A., Brock, O., & Ratz, A. (Eds.). (2015). *Soft Robotics*. Springer Berlin Heidelberg. <https://doi.org/10.1007/978-3-662-44506-8>
- Yang, Y., Chen, Y., Li, Y., Chen, M. Z. Q., & Wei, Y. (2017). Bioinspired Robotic Fingers Based on Pneumatic Actuator and 3-D Printing of Smart Material. *Soft Robotics*, 4(2), 147–162. <https://doi.org/10.1089/soro.2016.0034>
- Yang, H., Leow, W. R., & Chen, X. (2018). 3D Printing of Flexible Electronic Devices. *Small Methods*, 2(1), 1700259. <https://doi.org/10.1002/smt.201700259>
- Yang, D., Verma, M. S., So, J.-H., Mosadegh, B., Keplinger, C., Lee, B., Khashai, F., Lossner, E., Suo, Z., & Whitesides, G. M. (2016). Buckling Pneumatic Linear Actuators Inspired by Muscle. *Advanced Materials Technologies*, 1(3), 1600055. <https://doi.org/10.1002/admt.201600055>
- Zhu, R., Wallrabe, U., Woias, P., Wapler, M., & Mescheder, U. (2019). Semi-rigid ring-shaped electrode dielectric electroactive polymer membrane as buckling actuator. *Journal of Micromechanics and Microengineering*, 29(5), 055001. <https://doi.org/10.1088/1361-6439/ab078d>
- Wang, X.W.; Liu, Z.; Zhang, T. Flexible sensing electronics for wearable/attachable health monitoring. *Small* 2017, 13, 1602790
- Whitesides, G. M. (2018). *Soft Robotics*. *Angewandte Chemie International Edition*, 57(16), 4258–4273. <https://doi.org/10.1002/anie.201800907>